INFORMATION TO USERS

The most advanced technology has been used to photograph and reproduce this manuscript from the microfilm master. UMI films the text directly from the original or copy submitted. Thus, some thesis and dissertation copies are in typewriter face, while others may be from any type of computer printer.

The quality of this reproduction is dependent upon the quality of the copy submitted. Broken or indistinct print, colored or poor quality illustrations and photographs, print bleedthrough, substandard margins, and improper alignment can adversely affect reproduction.

In the unlikely event that the author did not send UMI a complete manuscript and there are missing pages, these will be noted. Also, if unauthorized copyright material had to be removed, a note will indicate the deletion.

Oversize materials (e.g., maps, drawings, charts) are reproduced by sectioning the original, beginning at the upper left-hand corner and continuing from left to right in equal sections with small overlaps. Each original is also photographed in one exposure and is included in reduced form at the back of the book. These are also available as one exposure on a standard 35mm slide or as a 17" x 23" black and white photographic print for an additional charge.

Photographs included in the original manuscript have been reproduced xerographically in this copy. Higher quality 6" x 9" black and white photographic prints are available for any photographs or illustrations appearing in this copy for an additional charge. Contact UMI directly to order.

Order Number 9012919

A numerical study of the seasonal variability of the Somali Current

Jensen, Tommy Gert, Ph.D.

The Florida State University, 1989

THE FLORIDA STATE UNIVERSITY

COLLEGE OF ARTS AND SCIENCES

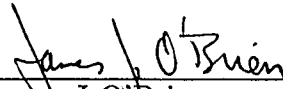A NUMERICAL STUDY OF THE SEASONAL VARIABILITY

OF THE SOMALI CURRENT

By

TOMMY G JENSEN

A Dissertation submitted to the
Program in Geophysical Fluid Dynamics
in partial fulfillment of the
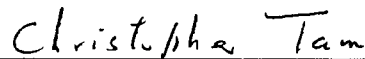requirements for the degree of
Doctor of Philosophy

Degree Awarded:

Fall Semester, 1989

The members of the Committee approve the dissertation of
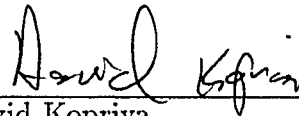Tommy G Jensen defended on October 5, 1989.

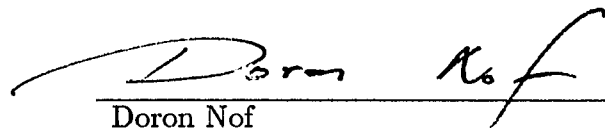James J O'Brien
Professor Directing Dissertation

Christopher Tam
Outside Committee Member

Benoit Cushman-Roisin
Committee Member

David Kopriva
Committee Member

Doron Nof
Committee Member

Abstract

A new numerical ocean model with multiple isopycnal layers has been used to model the Indian Ocean. Normal vertical modes are used for initialization and in a new open boundary formulation. A 21 year integration with the Hellerman–Rosenstein wind stress is made with a 3.5 layer and a 1.5 layer version of the model.

The solution with three active layers reproduces the observed general circulation and variability of the Indian Ocean, for instance the semi-annual equatorial undercurrent and Yanai wave field in the west. The seasonal changes in the Somali Current system is studied in more detail. It is found that barotropic instability is likely to cause the generation of the Great Whirl in early June. We find a very good agreement between the observed undercurrents and the simulations in the model. Equatorial onshore flow below the thermocline in June is associated with the disappearence of the undercurrent below the Somali current. The return of this undercurrent in the fall is caused by instability of the Great Whirl. Experiments where the duration of the summer monsoon is extended show that the initial decrease in the magnitude of the Great Whirl is due to eastward and downward energy transfer rather that due to relaxation of the wind. The solutions of the model indicate that baroclinic instability plays an important role in the decay of the Great Whirl.

The solution with a single active layer is essentially the same for the upper layer until in the late summer monsoon, when the flow becomes unstable. Different

decay patterns of the whirl and associated eddies leads to different flows during the winter monsoon.

Acknowledgement

I would also like to thank Mimi Burbank of SCRI for her expert assistance using $T_{\!E}\!X$ for the layout of the dissertation. Finally, I wish to express heartfelt thanks to Louise who's understanding, patience, encouragement and sense of humor was always there when needed.

TABLE OF CONTENTS

LIST OF FIGURES

From *Düing, Molinari and Swallow* (1980).   53

Figure 28 : Ten year average November 16. Velocity and depth to the bottom

of layer 1 (a), layer 2 (b), layer 3, (c) and surface elevation (d) in the

3.5 layer model. Panels (e) and (f) show the surface elevation and

upper layer thickness with velocity vectors in the 1.5 layer model.   54

Figure 29 : Observed alongshore currents at 5° N based on all available

complete monthly values from 1975 to 1979. (*a*): Vertical profiles,

(*b*) : Time series at two levels. From *Quadfasel and Schott*, (1983).   57

Figure 30 : Deep eddy observed in February to March 1965 along 9° N.

Geostrophic currents are based on hydrography with reference level obtained

from neutrally − buoyant floats. From *Bruce and Volkmann*, (1969).   58

Figure 31 : Velocities at 700 m. Solid arrows represent data observed between

May 16 and 22, 1979. Dashed arrows indicate data from May 26 to 31, 1979.

Temperature was measured along ship track (light line).

From *Leetmaa et al.*, (1980).   61

Figure 32 : Linear vertical mode solution. Section perpendicular to the coast

at 5° N (left panel) and section of alongshore flow 44 km from the coast.

The magnitude of the alongshore wind stress is shown above (right panel).

Contour interval is 10 cm/s. Shaded areas indicate southward flow.

surface elevation (cm) (d). Panel (e) : Available potential energy, (kJ/m^2).   84

1. INTRODUCTION

1.1. Motivation and objectives

There has been a long tradition at Florida State University of using isopy-cnic layered models with a limited vertical resolution to study ocean dynamics. Mc-Nider and O'Brien (1973) used a four-layer model to study coastal upwelling, while Hurlburt and Thompson (1980) investigated the circulation in the Gulf of Mexico using three different models: a two-layer, a reduced-gravity, and a barotropic model. Studies using reduced-gravity models with one moving layer have been succesful in simulating equatorial flow, for instance El Ninõ in the Pacific (Busalacchi and O'Brien, 1980). The work by Hurlburt and Lin, (1981), who demonstrated that a reduced-gravity model contained the essential physics for generation of a Somali Current, motivated later work with realistic geometries for the Indian Ocean as mentioned below, e.g., Luther and O'Brien (1985). These studies suggests that further progress can be made by including additional physics. For instance, Zebiak and Cane (1987) added a mixed layer of constant depth with thermodynamics on top of the upper layer and coupled the ocean to an atmospheric layer to study the El Ninõ-Southern Oscillation phenomenon. In a similar study (Schopf and Suarez, 1988) a two–layer reduced-gravity model allowed temperature variations in both active layers.

Layers permit accurate representation of low vertical modes compared to fixed levels. Therefore for fixed resources one can have finer horizontal resolution. Bleck and Boudra (1981, 1986) compared results from quasi-isopycnic layered mod-

1

els with other numerical formulations, for instance quasi-geostrophic layered models and isobaric models as Bryan's (1969) model. They found that the latter two suppressed barotropic and baroclinic instability. Two and three layer versions of their quasi-isopycnic model were also used to study the effect of model parameters on the circulation of the South Atlantic-Indian Ocean (Boudra and Ruijter, 1986).

The principal advantage of using density as the vertical coordinate as in the models above, compared to depth, is that no artificial cross isopycnal mixing occurs. Another consequence of using the layer thicknesses as variables is that better vertical resolution automatically is obtained in areas with strong stratification (Bleck and Boudra, 1986). The low vertical resolution effectively filters out higher vertical modes, which, due to their smaller length scales, are not adequately resolved by the horizontal discretization in the numerical model and consequently produce unwanted noise. Finally, these models with coarse vertical resolution and without prognostic thermohaline equations require relatively small computational resources compared to oceanic general circulation models with full physics. This makes it possible to perform numerical experiments where the effect of changing various parameterizations, boundary conditions, geometries and wind stress fields can be investigated. The multi-layer formulation to be used in this study is described in section 2.

The purpose of this study is to build a new multi-layer ocean model, which can simulate the seasonal changes of surface and subsurface currents in the Northwest Indian ocean, in particular the Somali Current system. As forcing, a seasonal climatological wind stress is used to obtain a quasi-periodic ocean circulation. The model results will be analyzed and compared with observations. The effect of additional layers will also be studied by comparing the currents in the upper layer of the

new model with calculations from a reduced-gravity model with the same geometry and forcing.

1.2. The Somali Current System

The circulation of the northwestern part of the Indian Ocean is highly influenced by the monsoon winds. The Somali Current, which has a volume transport comparable to that of the Gulf Stream (Lighthill, 1969), changes direction with the Monsoon winds: Northeastward currents during the summer (Southwest Monsoon) and southwestward currents during the winter (Northeast Monsoon). Swallow and Bruce (1966) reported a transport of 60 Sv in the upper 200 m during the summer monsoon, and surface velocities up to 3.7 m/s have been measured (Düing et al., 1980). Measurements made in 1964 during the International Indian Ocean Expedition (IIOE) and during the seventies showed that the flow pattern of the Somali Current is far more complicated than the continuous northward or southward flow as seen in climatological atlases, e.g. Schott (1983). In particular, during the summer it is now anticipated that a two-gyre system exists. Knox and Anderson (1985) defines the Somali Current System as "the currents along the African coast plus their associated eddies, offshore meanders and recirculations."

1.3. Observations

The observed seasonal changes have been reviewed by Schott (1983), Knox and Anderson (1985) and can be summarized as follows: In late winter the Somali current has a deep southward flow from the island of Socotra to about 2°–3° S. Here the flow joins the East African Coast current coming from the south into the eastward Equatorial Counter Current. In the early spring, usually in March, a northward surface current is established north of 5°N due to local wind stress curl. Below, between 150 m – 600 m, a southward undercurrent is found (Quadfasel

4

and Schott, 1983). Between the equator and 5°N the surface flow is southward. South of the equator a northward current increases in strength at this time, crosses the equator and flows offshore. During April and May this current migrates to the north. Southwesterly winds start in early May, and strong upwelling is found north of 3°–5° N, which is the latitude where offshore flow is found. A southward return flow develops offshore, and a gyre, the so called Southern Gyre, is formed. As the coast-parallel wind strengthens and strong anticyclonic wind stress curl occurs offshore, a northern gyre, often called the Great Whirl, a name introduced by Findlay (1866), who first reported it, is formed between 5° and 10° N. Wedges of cold water are found along the coast north of each gyre. As the Great Whirl deepens, the southward undercurrents disappear. This two gyre system is stable until August or September, when the Southern Gyre propagates northward and merges with the Great Whirl, as observed by Bruce (1973). The salinity of the Southern Gyre is lower than in the surrounding water mass before the coalescense, suggesting mass transport from the south. After this event the Somali Current becomes stationary, flowing from 4° S to 10° N, with northward transport above 150 m and southward transport reappears below (Quadfasel and Schott, 1983). To the north-east of the Great Whirl a third warm core eddy, the Socotra eddy is found in the late summer. Its relative high salinity indicates that the water in this eddy is advected from a higher latitude. This situation lasts until after the onset of the northeast monsoon in November, when a shift to southward currents takes places, first along the coast and later offshore. During the winter monsoon the flow is a deep southward continuous flow from Socotra to 5°S.

The seasonal cycle as described above is considered the most common situation and was the situation during the FGGE year 1979. Swallow and Fieux, (1982) reviewed historical data for May and June, from 1900 to 1973. They found

that the two gyre situation was the most common. The southern gyre was missing in three years, and could be found during May or June in 30 of the years. Out of 69 years, evidence of the Great Whirl was found in 55.

1.4. Modelling

It was suggested by Lighthill (1969) that the onset of the Somali Current in the spring was a result of remote forcing due to winds over the Arabian Sea turning eastwards. The linear theory predicted a response time of one month for the coastal current to be set up associated with the reflection of westward travelling baroclinic equatorial Rossby waves. The theory also predicted the existence of a deep undercurrent, and an offshore countercurrent, where the magnitude of the undercurrent depends on the relative strength of the first baroclinic and barotropic modes. His most important result was the short time scale required to create a western boundary current near the equator compared to the long time needed at mid-latitudes.

However, Leetmaa (1972, 1973) observed that in 1970 and 1971, a northerly flow forced by local winds started in the south, off the coast of Kenya, some time before the onset of the westerlies in the interior. This raised a controversary whether the Somali Current was a result of local or remote forcing.

Lin and Hurlburt (1981) used a simple reduced-gravity model in a rectangular domain to model the response to local meridional wind forcing. They found a response time of one week, and that a sequence of cyclonic and anticyclonic eddies formed north of the equator and moved poleward. Their simple model produced the most important features: Coastal upwelling was seen to the northwest of the latitude where the currents of a large warm eddy turned offshore, and found and wedges of a thin upper layer 500 km offshore just north of that separation point. The more detailed solution, *i.e.*, the magnitude of the transport, eddy activity and

intensity of the upwelling depended on whether open or closed boundary conditions were used and of the width of the wind stress field.

The first numerical simulation of the Indian Ocean circulation is due to Cox (1970). The model had realistic coastlines, with the horizontal resolution of $1°$ and 7 layers in the vertical. The observed large scale structure of the Indian Ocean was reproduced, including the annual reversal of the Somali Current with coastal upwelling during the summer, but eddies like the Great Whirl and the southern gyre were missing due to the coarse horizontal resolution in the model. During the summer the model boundary current did not extend as far north as observed, and the velocities in the boundary current were a factor of two or more too small. It was suggested that the Somali Current is barotropic up to $3°N$, where coastal upwelling drive a baroclinic transport. Using Ekman theory, Cox (1970) found vertical velocities up to 5 m/day due to local winds. Since these winds are important for the upwelling, it was concluded that local forcing was important in the north, while the southern part is a remotely forced western boundary current in a classical sense, *i.e.*, a return flow in response to a Sverdrup interior.

In a later study, Cox (1976) examined the two theories of remote versus local forcing using the numerical model of Cox (1970), but applied it to a large rectangular ocean, symmetric around the equator. It was found that the local forcing was dominant initially and caused the current to extent further north than by the remote forcing, which became important after a couple of weeks. A linear analytical theory by Anderson and Rowlands (1976) corroborates these results, showing that the amplitude of the boundary current increases linearly in time in the cause of local wind forcing, but quadratic in time for remote forcing.

Using monthly means of climatological wind stress to force a reduced-gravity model, Luther and O'Brien (1985) and Luther et al., (1985) succesfully

reproduced most of the observed features of the seasonal cycle as described above. Their simulation was the first eddy resolving, fully nonlinear model with realistic geometry of the northwestern Indian Ocean. During and after the collapse of the two gyre system some differences between model and observations are seen, and of course their model does not contain information of the vertical structure of the currents.

The scenario described in the section above, is subject to some interannual variability. Simmons et al., (1988) found that the number of eddies around Socotra in the fall depended on the wind forcing, which was based on ship observations from different years. In a recent study, Luther and O'Brien (1989), also using winds from ship observations applied to the model mentioned above, found that out of 23 years of model simulations, the southern gyre was missing in two. The coalescense of the southern gyre and the Great Whirl was seen in all but 7 years. On the other hand, the Great Whirl and the Socotra eddy occurred every summer.

Modelling the undercurrents has been less succesful. Hurlburt and Thompson (1976) found a cyclonic inflow and an undercurrent associated with the generation of the Great Whirl in a two-layer model. The upper layer response was in good agreement with the observed whirl and its northward migration, but the flow in the deep layer was not. Using a linear vertical mode model McCreary and Kundu (1985) found that an undercurrent developed south of an area with wind stress curl. For winds without curl, no undercurrent was seen. In a later study, McCreary and Kundu (1988) used a two-layer reduced-gravity model and found that no undercurrent was produced even in the presence of wind stress curl. Schott (1987) compared observations with the output from Philanders's 27-level model of the Indian Ocean. The results are not published, but the model is described in Philander and Pacanowski (1984, 1986). The model was driven by winds from

Hellerman and Rosenstein (1983) and initiated with climatological temperature and salinity data given by Levitus (1982). A good qualitative agreement between observations and model was found for the Somali Current. The model reproduced the undercurrent during the North East Monsoon, but lacked a deep response found in observations. The latter might be due to the rather short spin up time of 3 years from initialization of the model. Other recent modelling efforts are summarized by Luther (1987).

1.5. Model Experiments

Schott (1987) lists several topics not yet fully investigated due to lack of observations and model results:

Most emphasis has been given to the summer monsoon, and little is known about the structure of the currents during the winter monsoon. The extent of the undercurrents is not yet known. Other questions to be addressed are whether barotropic-baroclinic instability is important for the collapse of the Great Whirl, and whether local wind changes may be responsible responsible. The cause of this break down is not yet understood. These problems will be addressed here, in particular the two latter topics.

Two different configurations of a new numerical model will be used in this study. A version with one active layer over a non-moving lower layer will produce results which has the same physics as in the models by Luther and O'Brien (1985), Luther et al. (1985), but is driven by a different wind stress. Here a pseudo wind stress based on the Hellerman and Rosenstein (1983) wind stress analysis is used as wind forcing. The investigations mentioned above used another climatological wind stress, e.g., the NOAA Global Marine Sums data set. The second model version will have three moving layers over an infinitely deep lower layer. The geometry, wind forcing, and physical parameters, with the exception of vertical density profile, is

not changed from the computations with a single layer, in order that the effect of additional vertical resolution can be studied.

The models are spun up for 21 years, and an analysis of their seasonal cycle is presented and compared with observations. First the features of the general circulation of the Indian Ocean are described using 10 year averages of the model results from year 11 to 20. Next we focus on the seasonal variability of these averages for the Somali Current system including the undercurrents. Finally the evolution during the summer monsoon in year 21 is described and analysed in detail in order to determine the dynamics involved in the decay of the Great Whirl.

2. MODEL FORMULATION

2.1. *Physics of the model*

We apply the equations of motion and conservation of mass for the ocean in spherical coordinates (see Semtner, 1986). Let the longitude and latitude be given by ϕ and θ and the velocity components towards the east and north be u and v, respectively. As radial coordinate we use $z = r - a$, where r is the radial distance from the center of a spherical earth with radius a. We choose $z = 0$ to be the surface of the ocean at rest. Define vertically integrated volume transport components U_j and V_j by

$$U_j = \int_{z_j}^{z_{j+1}} u \, dz \qquad (2-1)$$

between two surfaces $z_j(\phi, \theta, t)$ and $z_{j+1}(\phi, \theta, t)$, with an equivalent expression for V_j. The thickness of the j-th layer defined by this integration, is $H_j = (z_{j+1} - z_j)$.

Consider an ocean consisting of several layers of uniform density as shown in Fig. 1. The layers are labelled with increasing numbers downward. Let us assume that all layers have a positive thickness everywhere for all time. This implies that layers are not allowed to surface or merge, and that the bottom topography, given by $z = D(\phi, \theta)$, is always in the lowest layer. A numerical technique, the Flux Corrected Transport (FCT) scheme (see Zalesak, 1979), makes it possible to relax these restrictions and has recently been applied to layered ocean models to allow fronts at the surface, e.g., Bleck and Boudra (1986), Huang (1987). The method requires that the flux in the continuity equation is calculated as a combination

10
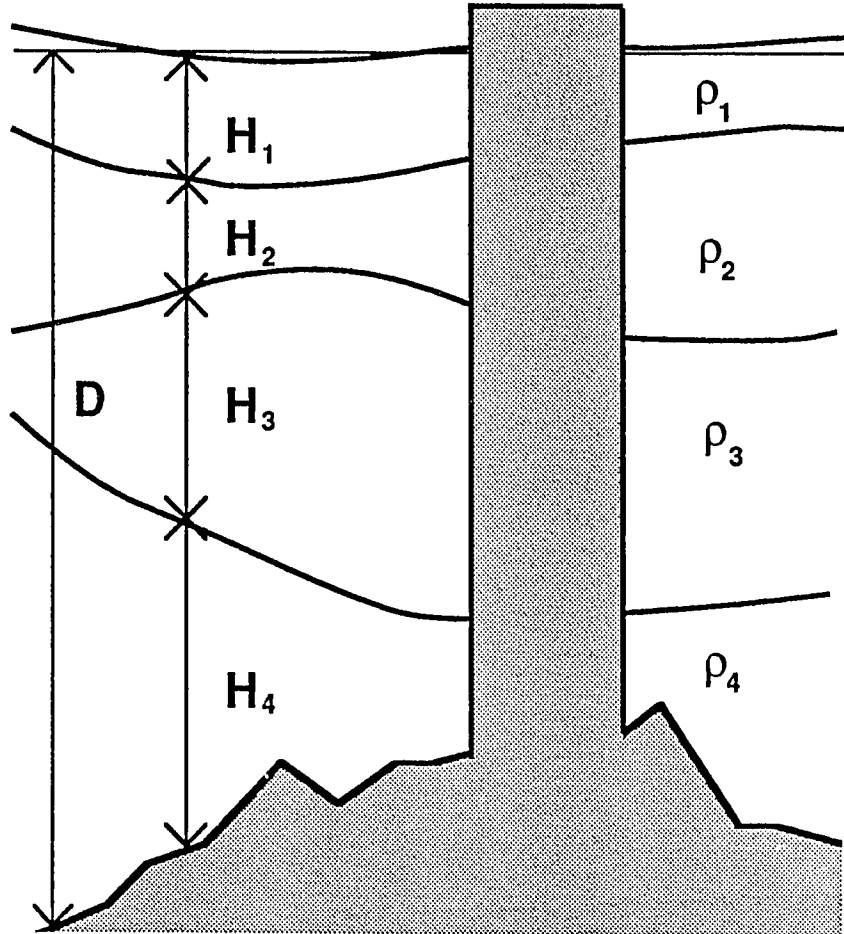
Figure 1. Vertical structure of a four layer isopycnal model. Bottom topography does not intersect isopycnals.

from a diffusive scheme and a non-diffusive scheme with the constraint that the layer thickness always is greater than zero. One problem with the method is that it does not allow quadratic-conservative flux form of the non-linear terms, which requires division by the layer thickness. Consequently it will not be applied in the present study. The derivation of the equations below is given in Appendix A. If the density and thickness of the j-th layer is given by ρ_j and H_j, the transport equation for U becomes

$$\frac{\partial U_j}{\partial t} + \frac{1}{a\cos\theta}\frac{\partial}{\partial \phi}\left(\frac{U_j^2}{H_j}\right) + \frac{1}{a}\frac{\partial}{\partial \theta}\left(\frac{U_j V_j}{H_j}\right) - \frac{2U_j V_j}{aH_j\cot\theta} - fV_j =$$

$$\frac{-H_j}{\rho_j a\cos\theta}\left[\frac{\partial p_a}{\partial \phi} + \rho_j g\frac{\partial \eta}{\partial \phi} - g\sum_{i=1}^{j-1}(\rho_j - \rho_i)\frac{\partial H_i}{\partial \phi}\right] + \mathcal{F}^\phi + \left(\frac{\tau_j^{\phi,t}}{\rho_j} - \frac{\tau_j^{\phi,b}}{\rho_j}\right) \qquad (2-2)$$

where the horizontal friction for the U equation is given by

$$\mathcal{F}^\phi = A\left[H_j\nabla^2\left(\frac{U_j}{H_j}\right) - \frac{1}{a^2\cos^2\theta}\left[U_j(1 - 2\cos^2\theta) + 2\sin\theta\, H_j\frac{\partial}{\partial \phi}\left(\frac{V_j}{H_j}\right)\right]\right] \qquad (2-3)$$

and similarly for V, we have

$$\frac{\partial V_j}{\partial t} + \frac{1}{a\cos\theta}\frac{\partial}{\partial \phi}\left(\frac{U_j V_j}{H_j}\right) + \frac{1}{a}\frac{\partial}{\partial \theta}\left(\frac{V_j^2}{H_j}\right) + \frac{(U_j^2 - V_j^2)}{aH_j\cot\theta} + fU_j =$$

$$\frac{-H_j}{\rho_j a}\left[\frac{\partial p_a}{\partial \theta} + \rho_j g\frac{\partial \eta}{\partial \theta} - g\sum_{i=1}^{j-1}(\rho_j - \rho_i)\frac{\partial H_i}{\partial \theta}\right] + \mathcal{F}^\theta + \left(\frac{\tau_j^{\theta,t}}{\rho_j} - \frac{\tau_j^{\theta,b}}{\rho_j}\right) \qquad (2-4)$$

with the horizontal friction term

$$\mathcal{F}^\theta = A\left[H_j\nabla^2\left(\frac{V_j}{H_j}\right) - \frac{1}{a^2\cos^2\theta}\left[V_j(1 - 2\cos^2\theta) + 2\sin\theta\, H_j\frac{\partial}{\partial \phi}\left(\frac{U_j}{H_j}\right)\right]\right] \qquad (2-5)$$

In the equations above g is the acceleration of gravity, τ the tangential stress due to vertical friction, where the superscripts denote the ϕ or θ component and top or bottom of layer. With N layers the surface displacement η is given by

$$\eta = D + \sum_{i=1}^{N} H_i \qquad (2-6)$$

In the equation above the parameterization of the horizontal eddy viscosity is based on the velocity field and not the vertically integrated transport as most often seen in layered models. The formulation has been chosen so a thin layer with large velocities will experience more friction than a thick layer with equivalent transport. It is also seen, that if the layer thickness gradient is constant, the geostrophic current will experience a spin down due to friction. In the case where the horizontal friction is proportional to the Laplacian of the transport, a steady geostrophic solution is possible. The magnitude of the horizontal friction coefficient, A, used in the calculations was 750 m^2/s, the same value used by Woodberry et al. (1989).

The only vertical stress to be applied in the model in this study is the wind stress, which acts as a body force on the upper layer.

The continuity equation becomes

$$\frac{\partial H_j}{\partial t} + \frac{1}{a\cos\theta}\left[\frac{\partial U_j}{\partial \phi} + \frac{\partial}{\partial \theta}(V_j\cos\theta)\right] = w_e \qquad (2-7)$$

where w_e is a source term due to entrainment. This term is positive for the upper layer in case its thickness becomes less that a preset minimum depth H_{min}, and of the same magnitude but negative for the second layer. For deeper layers the term is always set to zero. This entrainment is included only to prevent the interface between the first two layers to surface. The parameterization of McCreary and Kundu, (1988) is used. However, the effect on the upper layer density, momentum and kinetic energy balance by this entrainment has been neglected here. For the momentum equations the term ignored is $w_e\vec{v}_2$, which is the transfer of momentum from the second to the top layer. The entrainment velocity is given by

$$w_e = \begin{cases} \frac{(H_1-H_{min})^2}{\tau_e H_{min}} & H_1 \leq H_{min} \\ 0 & H_1 > H_{min} \end{cases} \qquad (2-8)$$

The simplification made by only considering the effect of w_e in the continuity equation corresponds to entrainment where the engulfed water into the upper

layer has zero velocity and is heated instantaneously to the density ρ_1. It should be emphasized that this adjustment is rarely active in the results presented in this work. We chose 60 m for H_{min} and a time constant τ_e of 1.2 hours.

We can ignore forcing due to the gradient in atmospheric pressure, p_a, compared to the wind stress for large scale and mesoscale motion, e.g. Gates (1966); thus the barotropic pressure gradient is contained in the term where the surface deviation η appears. Because of the large phase speeds of barotropic gravity waves most numerical models have a special treatment of this mode. For instance, most authors filter out these waves by applying the rigid lid approximation, for example as in Bryan's (1969) world ocean model, or using a semi-implicit numerical scheme (O'Brien and Hurlburt, 1972, Hurlburt, 1974, Hurlburt and Thompson, 1976). Here we shall apply another method to remove the barotropic modes, including the planetary waves, by assuming that the pressure gradient vanishes in the lowest layer, which implies that the velocity also is zero in the deep ocean. From (2-2) and (2-4) we obtain by taking the limit $H_N \rightarrow \infty$, that the gradient of the surface elevation is given by

$$\nabla \eta = \sum_{i=1}^{N-1} \left(\frac{\rho_N - \rho_i}{\rho_N} \right) \nabla H_i \qquad (2-9)$$

The effect of bottom topography can to some extent be included when $(2-9)$ is applied by generalizing the method of Cushman-Roisin and O'Brien (1983). They demonstrated that the effect of variable bottom topography in a two-layer model can be simulated by locally changing the phase speed in a reduced-gravity model. Here we will use $(2-9)$ with $N = 4$ and $N = 2$, which gives us a 3.5 layer model and a 1.5 layer model, respectively. Explicit integration of the set of equations $(2-2)$ to $(2-8)$ with a finite depth, providing that the isopycnals does not intersect the bottom topography (e.g., Fig. 1), is in principle done in the same way, but limitations due to the very short time step in the integration makes this impractical. The computer

15

time needed increases by a factor of 40 compared to the reduced-gravity case with the same number of layers.

2.2. Model geometry

The model covers the northwestern part of the Indian Ocean from 25.1°S to 26.1°N and 34.8°E to 119.6°E. The coastlines are identical to those used by Woodberry, et al., (1989). As seen from (Fig. 2) the eastern and southern boundaries are open, while the no-slip condition is applied along land boundaries. The 200 m isobath was used to define the coastlines. This implies that groups of coral reef islands, such as the Laccadives and Maldives southwest of India, and the Seychelles Bank, Saya de Malha Bank with the Agalegas Islands and Nazarath Bank with the Cargados-Carajos Islands, which are found northeast and west of Madagascar, appears as large islands.

It might have been preferable to extend the model further south to include more of the southern gyre, and model the flow around the southern tip of Madagascar, but the present geometry was chosen since prepared wind fields and digitized coastlines were available.

2.3. Numerical formulation

The model equations are discretized in space on the Arakawa C-grid (Mesinger and Arakawa, 1976, Arakawa and Lamb, 1977). The numerical scheme, which is mass and energy conserving, is nearly identical to the C scheme tested by Grammeltvedt (1969) and first proposed by Lilly (1965). With a distance between two similar points, for instance two H-points, of 0.2° in both horizontal directions, the model domain contains 425 × 256 grid points per layer for each variable.

With the barotropic mode excluded using (2-9) we can solve the finite difference equivalents of eqns. (2-2) to (2-8) using an explicit time integration scheme
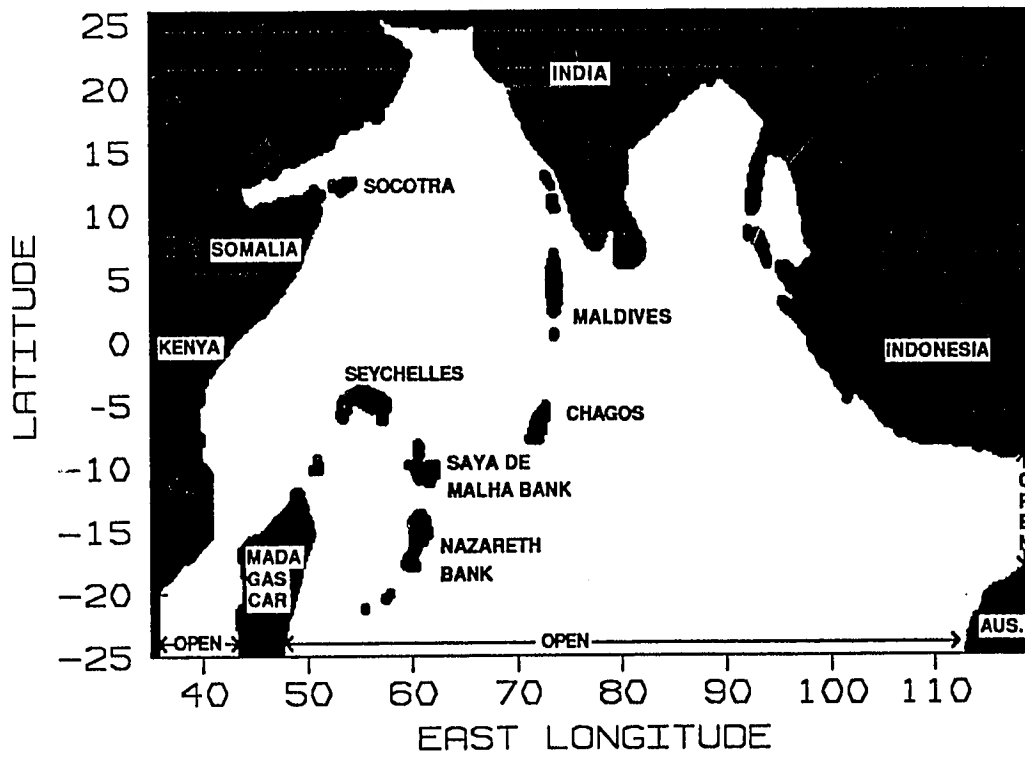
Figure 2. Model geometry. The 200 m isobath is used as coastlines. There are open boundaries to the south and in the east.

without a severe restriction in time step. With the grid above the leap-frog time integration scheme is stable with a time step of about 20 minutes, depending on the current speed and the phase speed of the first vertical mode in the model. For the Laplacian friction term a Dufort-Frankel implicit scheme is applied for stability (e.g., O'Brien, 1986). An Euler forward scheme is applied to every 99 steps to filter out the computational mode inherent in the leap-frog scheme.

The model is coded in Fortran 200, fully vectorized, to run on the Cyber 205 and ETA10 vector computers. Less than 5% of the CPU time is spent for scalar computations. Half precision (32 bits) variables have been used in the calculations, to make the code nearly twice as fast compared to when full precision (64 bits) variables are declared. The largest terms, *i.e.*, Coriolis terms, pressure gradient terms and wind stress are computed separately to avoid unnessessary round off errors. Their sum is added to the sum of the remaining terms in the momentum equation. For the same reason, only the layer thickness deviations, $(H_j - H_{0j})$, was stored and used as dependent variable. The model requires about 25 minutes of CPU time per active layer per model year on a one processor ETA10-G or 1 hour on the Cyber 205. The memory requirement for the ocean model is designed to fit within a 4 megaword central memory to avoid paging. The 3.5 layer model requires 2.4 megawords of storage.

2.4. Boundary and initial conditions

At the coast it is assumed that both components of the transport vanishes, *i.e.*, the no slip condition. The boundary layer is not resolved, but as shown by Cox (1979), this condition is provides a vorticity flux from the boundary into the interior, which gives a more realistic solution. While these boundary conditions are simple, the correct conditions to be used at open boundaries in multi-layer models are less obvious. An easy approach is to apply a Sommerfeld radiation condition to each

layer separately. However, different vertical modes have different phase speeds, and a more accurate method is to separate the solution along the open boundary into these modes. Using linear theory for an ocean with flat bottom, Lighthill (1969) showed that the vertical modes of the velocity are eigenvectors to the matrix

$$a_{jk} = \frac{\rho_{min(j,k)}}{\rho_j} H_k \qquad (2-10)$$

and the eigenvalues correspond to the equivalent depths for each mode. By inverting the matrix which has the eigenvectors of a_{jk} as columns, we can find the amplitude for each vertical mode from the solution of the layered model. The radiation condition is applied to each mode separately and the resulting current components along the open boundary can then be computed as the sum of these vertical modes.

Several numerical approximations to the Sommerfeld radiation condition have been proposed. The scheme implemented in this model was given by Camerlengo and O'Brien (1980), who improved and simplified the original scheme by Orlanski (1976). Both these conditions and the more simple extrapolation condition were tested on a model problem to select the most suitable open boundary condition, and the best results were obtained using the Camerlengo and O'Brien scheme on each vertical mode. Details are given in Appendix B. A review of radiation boundary conditions can be found in Hedley and Yau (1988), while Røed and Cooper (1986, 1987) considered a wider range of open boundary conditions. In the three references above it was demonstrated that the schemes based on the radiation condition may be inadequate in some cases.

The vertical modes for the Indian Ocean given by Gent, et al., (1983) have been used to select the initial layer thicknesses. For the first three vertical baroclinic modes they reported equivalent depths of 79.9 cm, 30.5 cm and 12.6 cm, respectively. By selecting ρ_j for four layers as 1.0239, 1.0262, 1.0273 and 1.0279 g/cm^3 and layer thicknesses H_j, 200 m, 250 m and 400 m for the three upper layers,

we obtain equivalent depths of 102 cm, 22.5 cm and 10.2 cm. This corresponds to Kelvin wave speeds of 316 cm/s, 149 cm/s and 100 cm/s for the three baroclinic modes, compared to 280 cm/s, 173 cm/s and 111 cm/s found by Gent, et al., (1983). Realistic initial phase velocities for the internal gravity waves were chosen to ensure good phase correlation with observed currents. For comparison, the Kelvin wave phase speeds of the first three vertical modes in the model by Cox (1976) were 291 cm/s, 179 cm/s and 117 cm/s. In the 2.5 layer model of McCreary and Kundu (1988) the initial values were 321 cm/s and 123 cm/s. For the 1.5 layer model $\rho_1 = 1.025$ g/cm^3 and $\rho_2 = 1.028$ g/cm^3 was selected, which corresponds to a value of reduced gravity of 0.03 m/s^2 also used by Woodberry, et al., (1989). This results in a Kelvin wave speed of 245 cm/s. Kindle and Thompson (1989) used the same density difference, but used an initial upper layer thickness of 250 m in their 1.5 layer model, resulting in a phase speed of 274 cm/s.

However, when the models are fully non-linear as those presented here, the actual phase speed will vary with space and time depending of the solution.

2.5. Wind forcing

The model is forced by a climatological monthly mean wind stress based on the data set prepared by Hellerman and Rosenstein (1983). A pseudo-stress is formed by dividing these data by the product of an average drag coefficient and an air density (Woodberry, et al., 1989). This allows the drag coefficient and air density to be model parameters independent of the wind analysis. A constant drag coefficient of 1.5 10^{-3} and an air density of 1.2 kg/m^3 has been applied here. Figs. 3 to 6 show the wind stress and its curl for February, May, August and November.

South of 10°S the winds a directed towards WNW with strongest winds in September and October. North of the equator the monsoon winds blow towards SW from November to March with maximum wind stress in January. The sum-
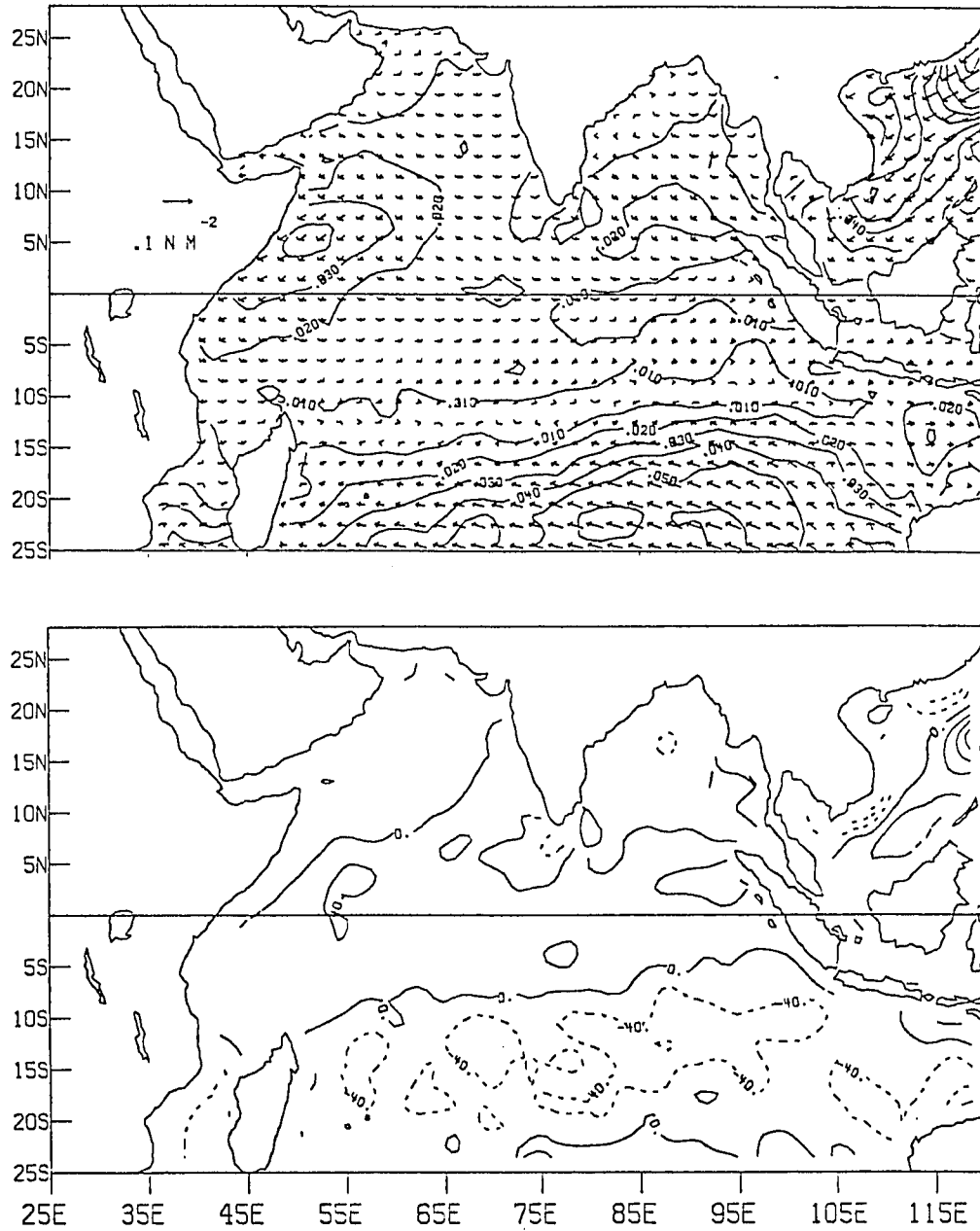
Figure 3. Wind stress and its curl over the Indian Ocean for February. The contour interval is 0.01 N/m² and 4.0·10⁻⁸ N/m³.
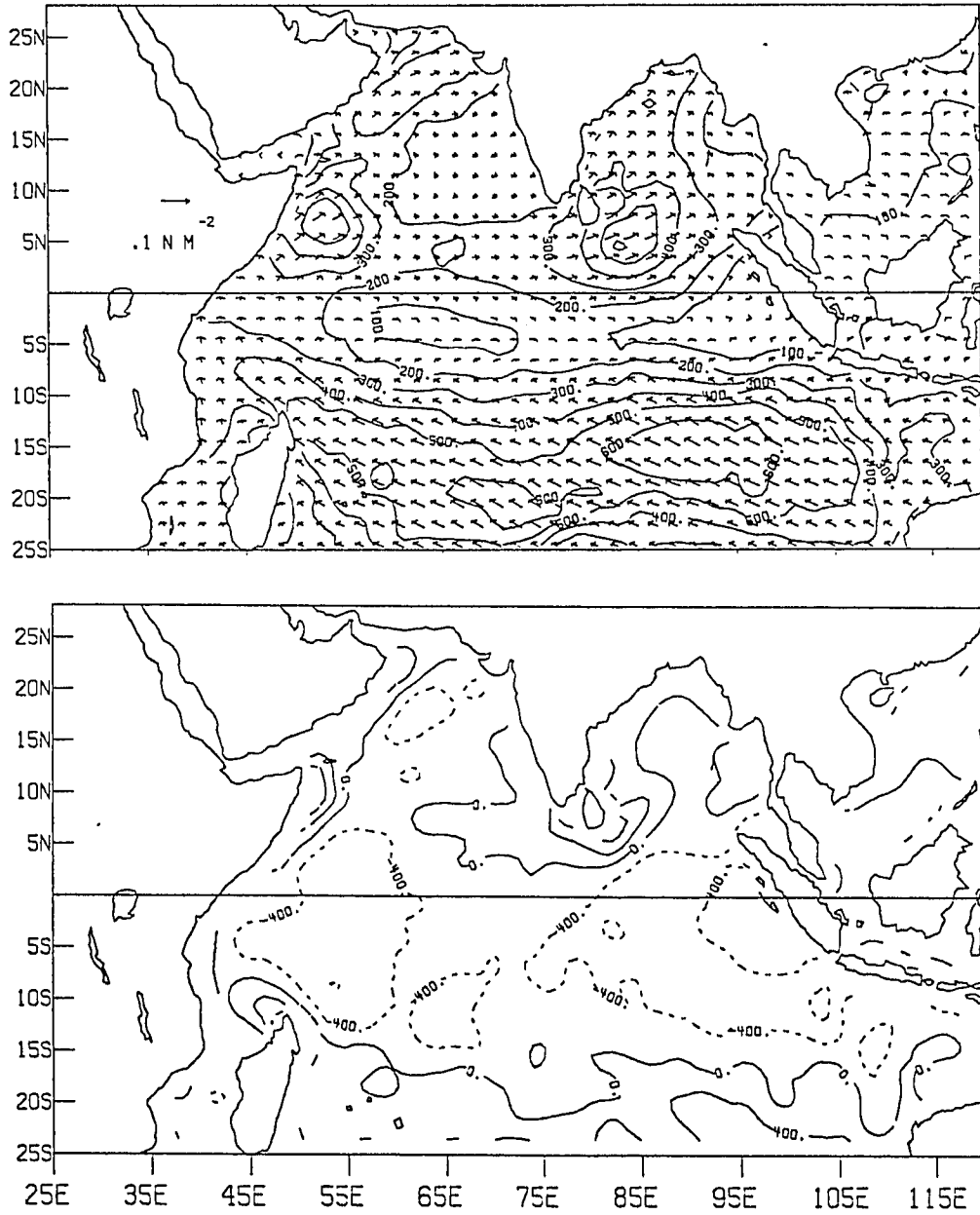
Figure 4. Wind stress and its curl over the Indian Ocean for May. The contour interval is 0.01 N/m^2 and $4.0 \cdot 10^{-8}$ N/m^3.
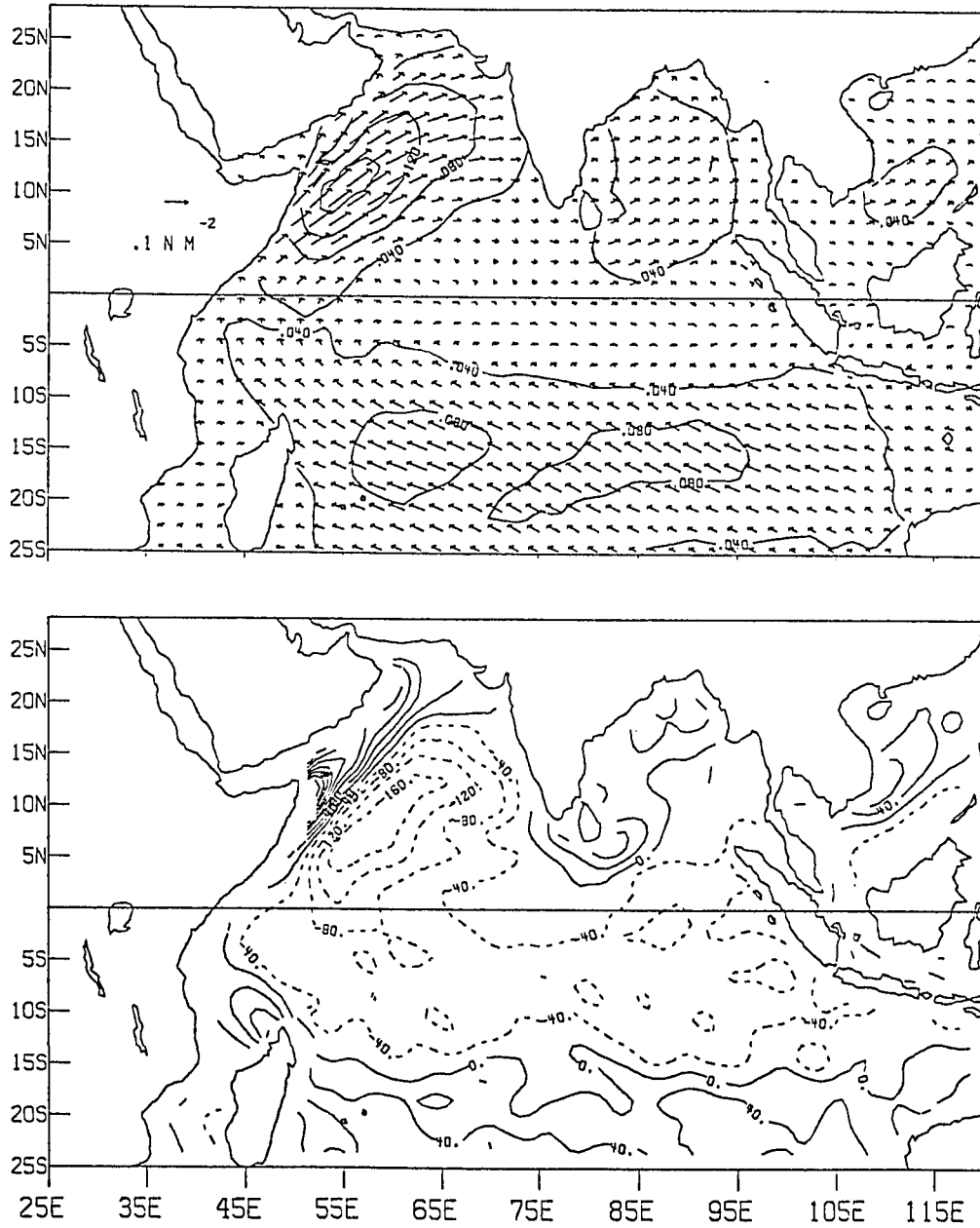
Figure 5. Wind stress and its curl over the Indian Ocean for August. The contour interval is 0.01 N/m^2 and $4.0 \cdot 10^{-8}$ N/m^3.
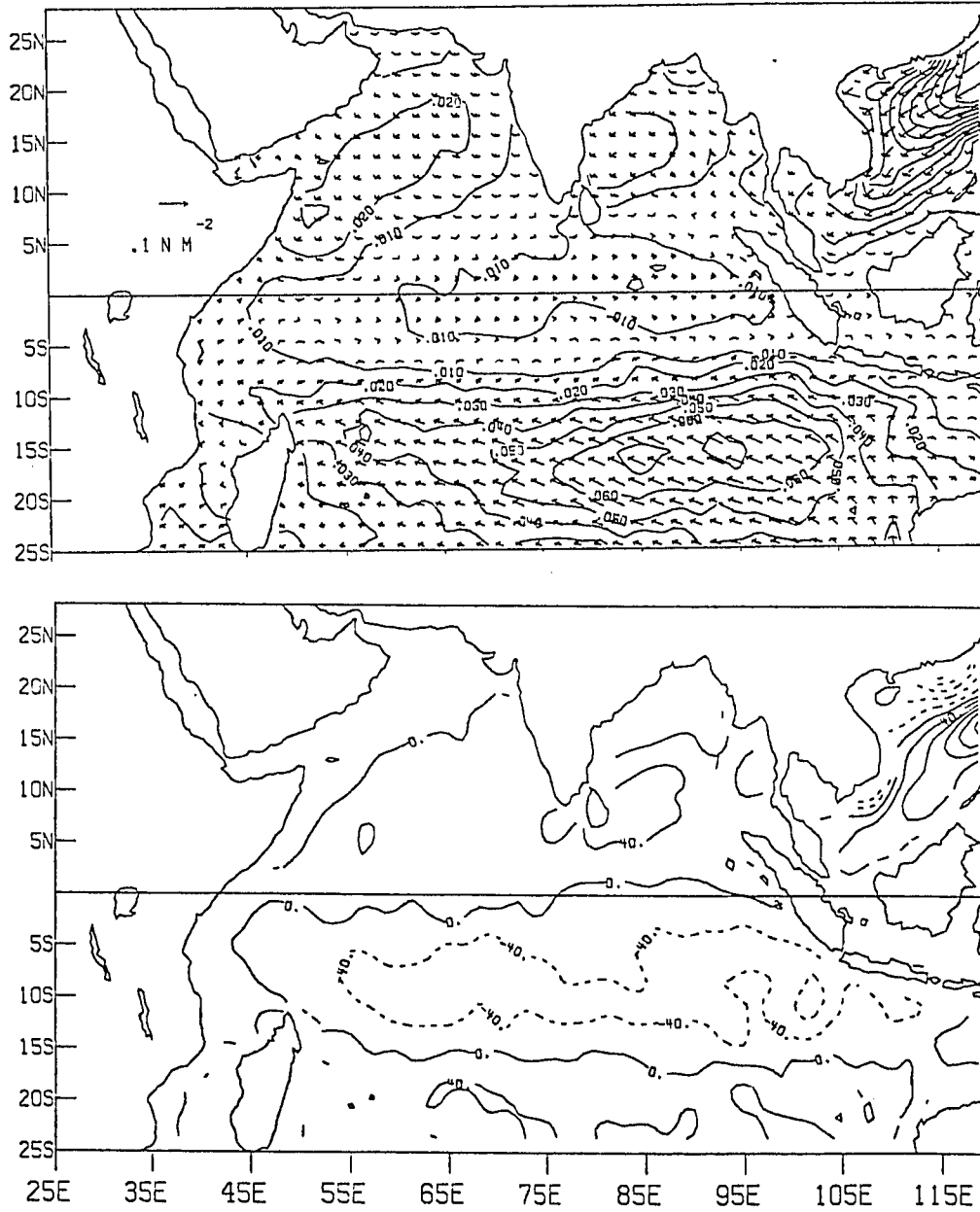
Figure 6. Wind stress and its curl over the Indian Ocean for November. The contour interval is 0.01 N/m^2 and $4.0 \cdot 10^{-8}$ N/m^3.

24

mer monsoon is much more intense, with northeastward winds from May through September. A bicubic spline was used to interpolate the pseudo-stress to the model grid from the $2° \times 2°$ grid of the original data set. Linear interpolation was applied to compute the wind stress at a given time step from the monthly average values. To avoid excessive generation of internal waves when the model is started from rest, the wind stress field is multiplied by the function

$$(1 - \exp(-t/\tau_0)) \qquad\qquad (2-11)$$

where $\tau_0 = 20$ days, during the first year of the spin up. This wind forcing was chosen to make comparison easier with the results of Woodberry et al. (1989), who used the same wind forcing to drive their model. Further details are given in their work.

With the wind forcing used here, rapid wind changes are not resolved. Using scatterometer data with 6 days resolution compared to COADS data with 30 days resolution, Perigaud and Delecluse (1988) found that the response of a 1.5 non-linear reduced-gravity model was insensitive to the high frequency part of the forcing.

The model is spun up from rest by applying the annual wind stress cycle repeatedly, until a quasi-periodic solution is obtained. From experience with 1.5 layer reduced-gravity models (Luther and O'Brien, 1985, Luther et al., 1985 and Woodberry, et al. 1989) a spin-up time of less than 20 years can be expected with three baroclinic modes. In the two first of these studies a spin up time of three years was reported to be adequate for the Somali Current. This was due to the limited area of the model. In the last work, the spin up of the southern part of the Indian Ocean required approximately 7 years of integration to obtain a periodic solution. Here, since higher vertical modes propagate slower, the spin up time can be expected to be longer.

3. RESULTS

Before we focus on the Somali Current, the ability of the model to simulate the general circulation of the Indian Ocean is briefly discussed. The results described here are based on the layer thicknesses and velocity fields at day 16 each month, averaged from year 11 through year 20 of the spin up. The equatorial currents and counter currents as well as the upwelling or cooling of the Arabian Sea west of India are reproduced well by the model. Climatological maps of the surface currents can be found in Wyrtki (1971), Knox and Anderson (1985), and Knox (1987).

3.1. General Circulation of the Indian Ocean

The south equatorial current (SEC) is the most persistent current in the model as well as in the Indian Ocean. Its westward flow reach from about 10° S to 20° S, a couple of degrees further south during the northern summer. This widening is in agreement with observations, which also show an increase in transport from 33 Sv to 39 Sv during the same period (e.g., Wyrtki, 1971, Schott, 1983). The average transport in the model is 25.7 Sv, while the 1.5 layer model has an average transport of 25.0 Sv. While the single layer solution has a small seasonal signal, the transport varies from 19 Sv in April to 31.6 Sv in September for the 3.5 layer case. For the upper layer the transports for the same months are 21.0 Sv and 26.4 Sv, respectively, but the maximum is seen in October and November with 26.7 Sv.

The SEC separates at 20°S into a southward and northward branch, the latter feeding the northward flowing East African Coastal Current (EAC), which is very important for the Somali Current by either enhancing or opposing its flow,

25

26
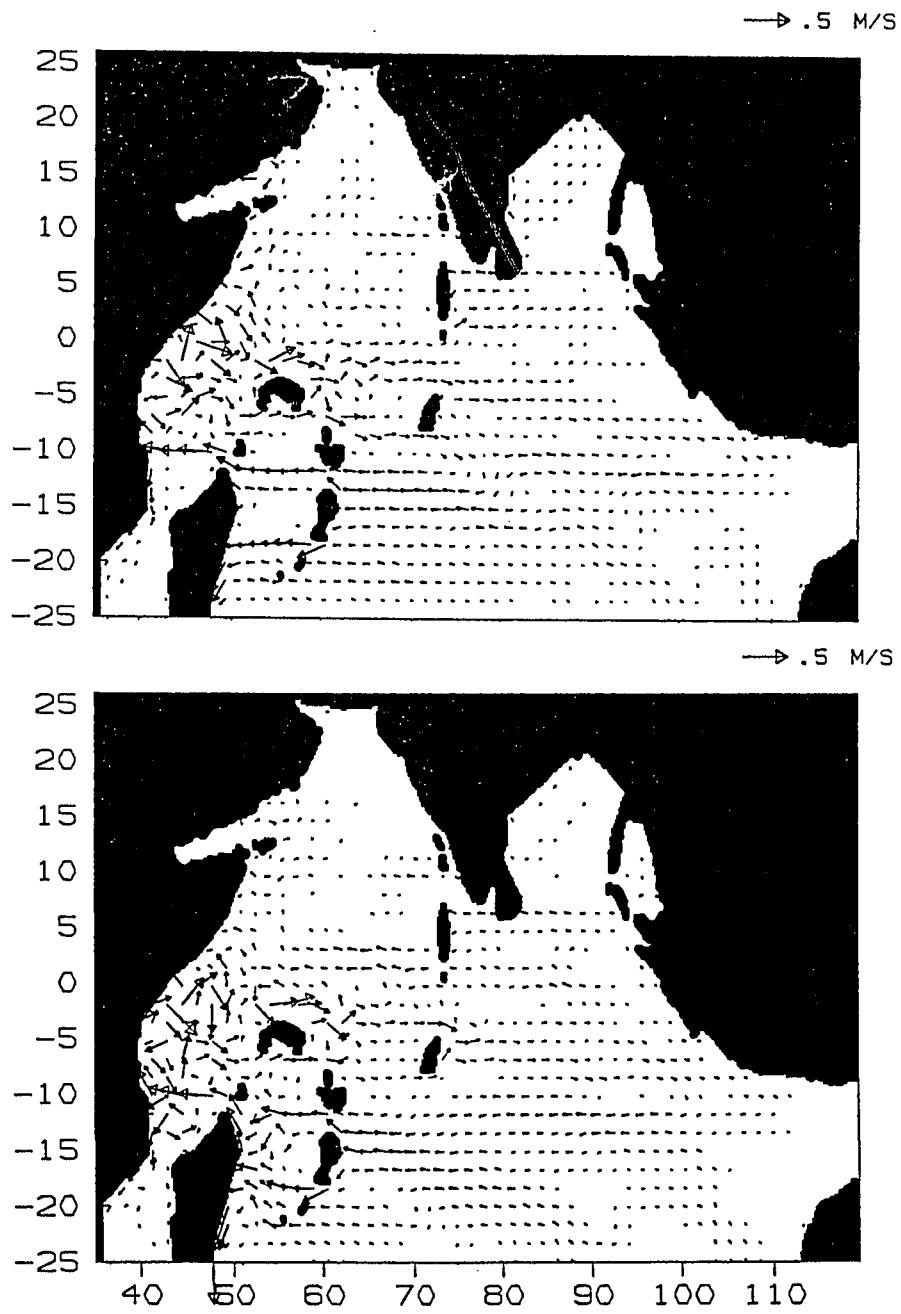
Figure 7. Current velocity in the upper layer of the Indian Ocean. Ten year average of February 16. top: 1.5 layer model. bottom: 3.5 layer model
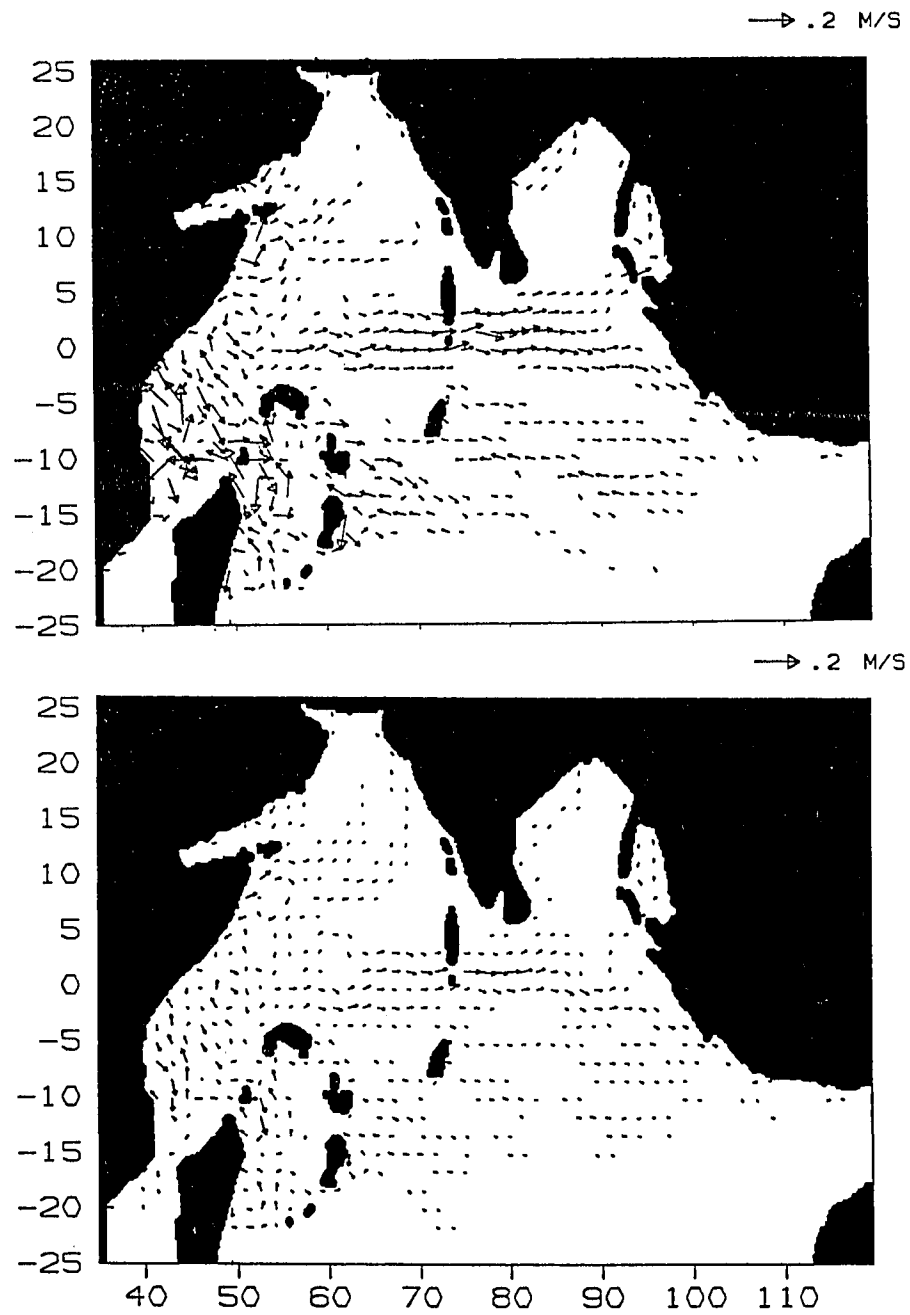
Figure 8. Current velocity in the second (top) and third (bottom) layer of the Indian Ocean. Ten year average of February 16.
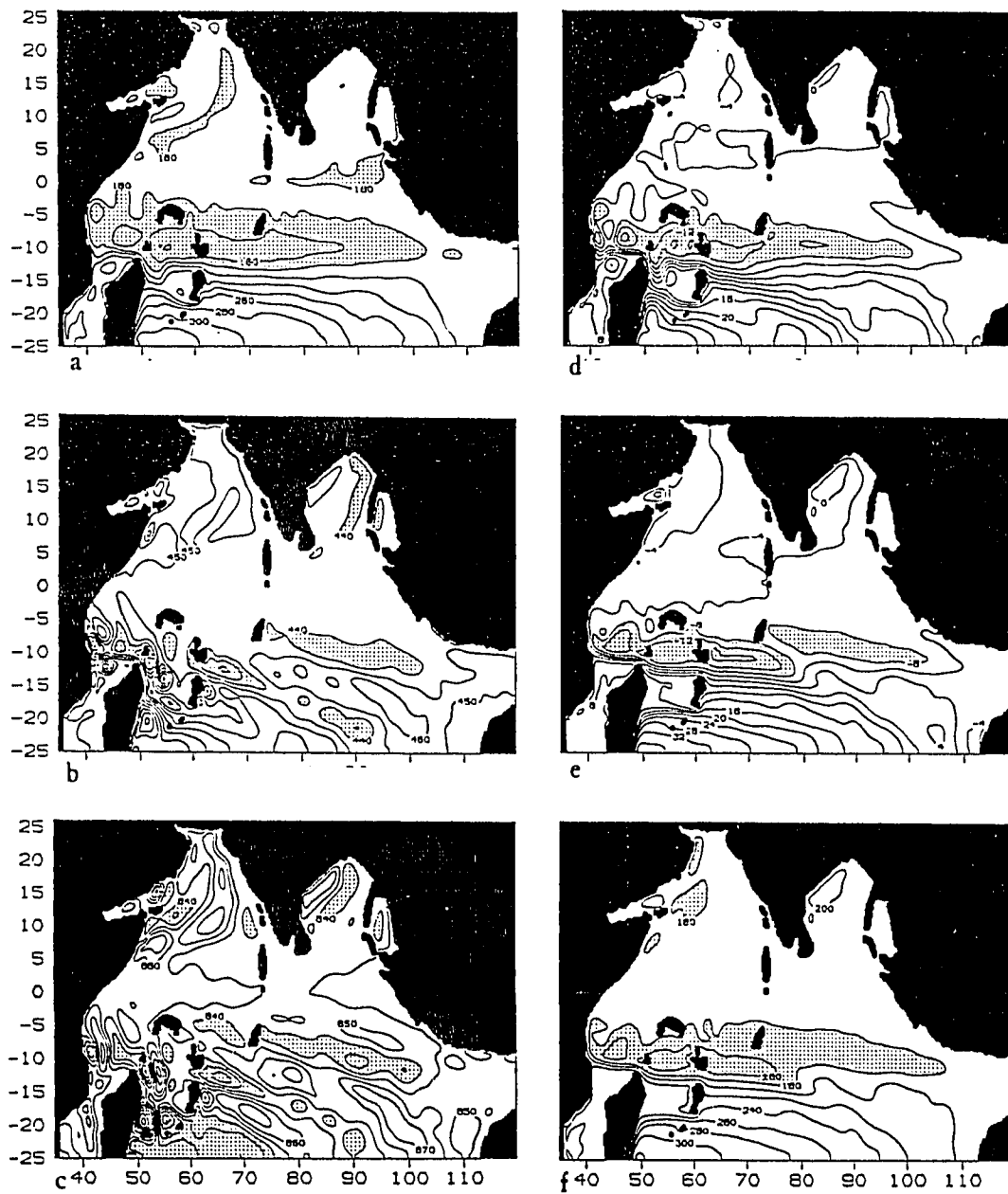
Figure 9. Ten year average February 16. Depth to the bottom of layer 1 (a), layer 2 (b), layer 3, (c) and surface elevation (d) in the 3.5 layer model. Panels (e) and (f) show the surface elevation and upper layer thickness in the 1.5 layer model.
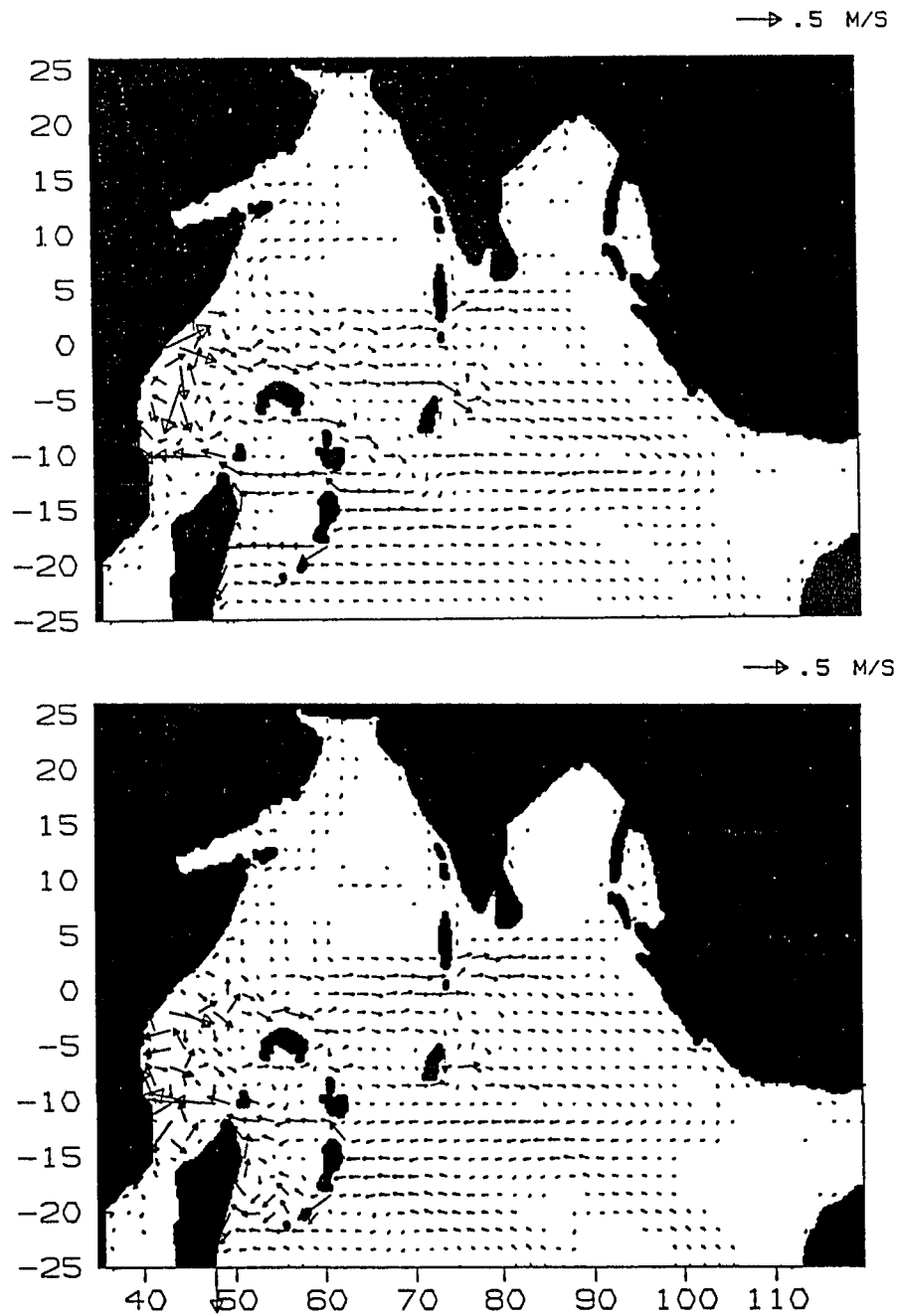
Figure 10. Current velocity in the upper layer of the Indian Ocean. Ten year average of May 16. top: 1.5 layer model. bottom: 3.5 layer model
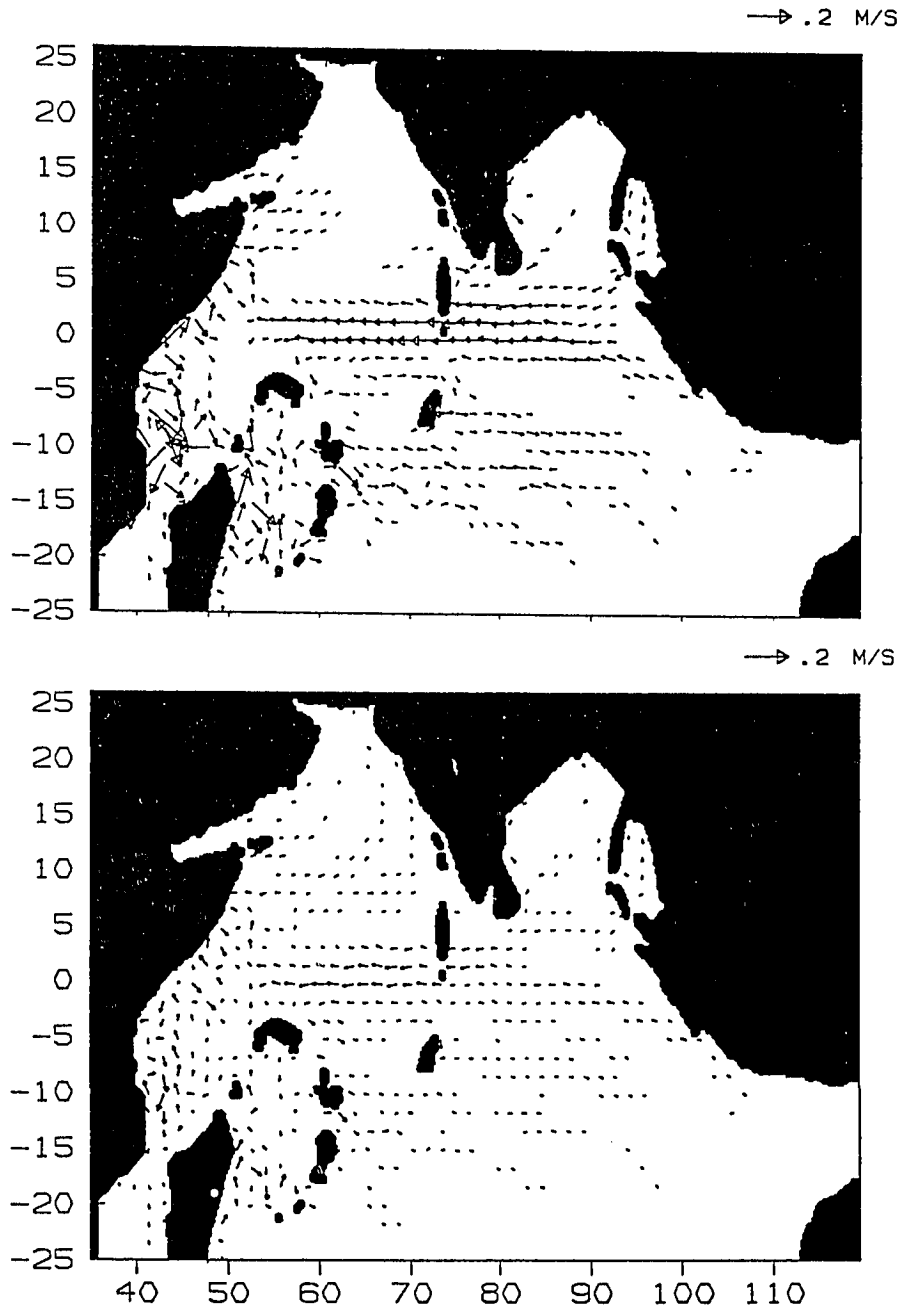
Figure 11. Current velocity in the second (top) and third (bottom) layer of the Indian Ocean. Ten year average of May 16.

31
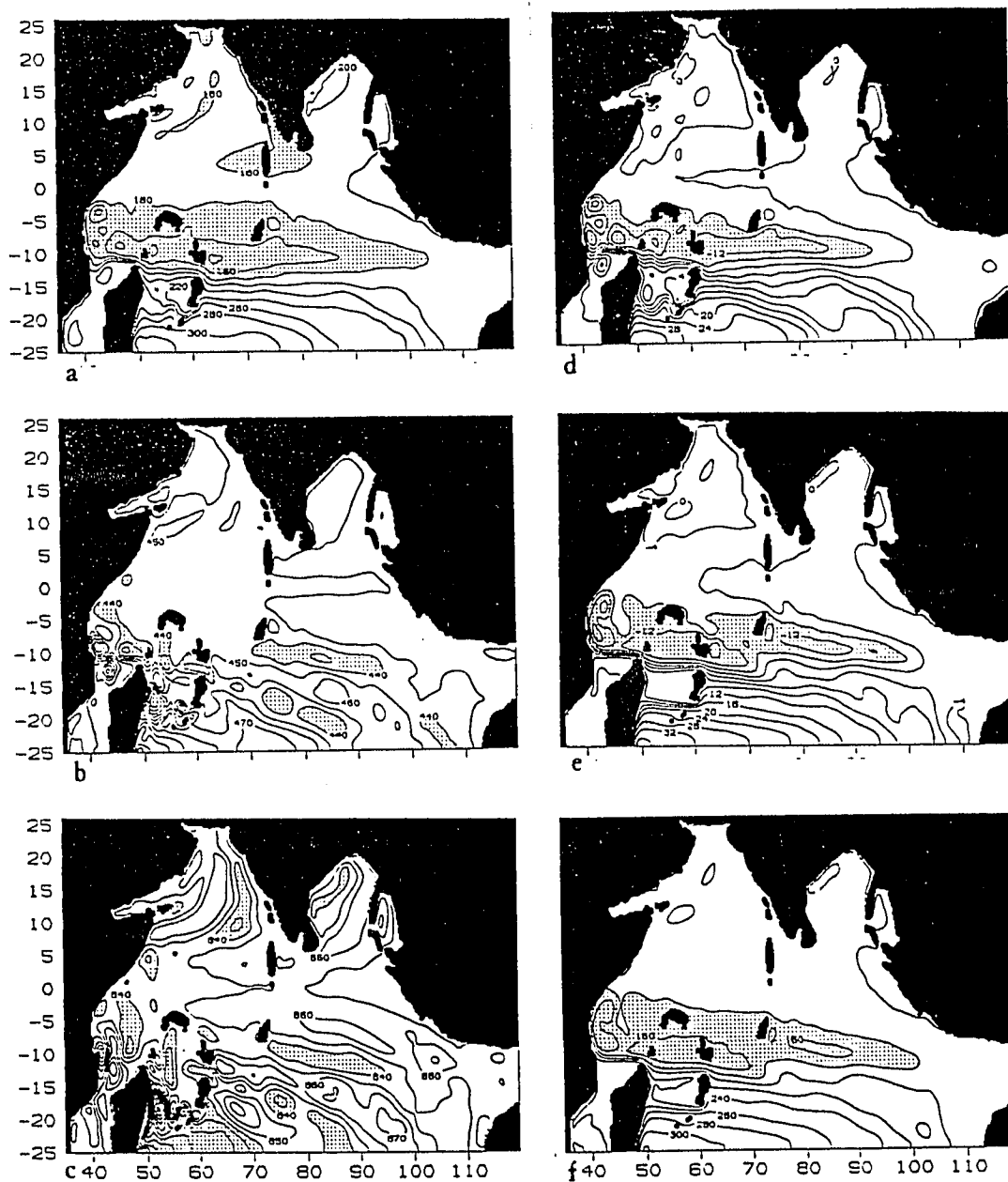
Figure 12. Ten year average May 16. Depth to the bottom of layer 1 (a), layer 2 (b), layer 3, (c) and surface elevation (d) in the 3.5 layer model. Panels (e) and (f) show the surface elevation and upper layer thickness in the 1.5 layer model.
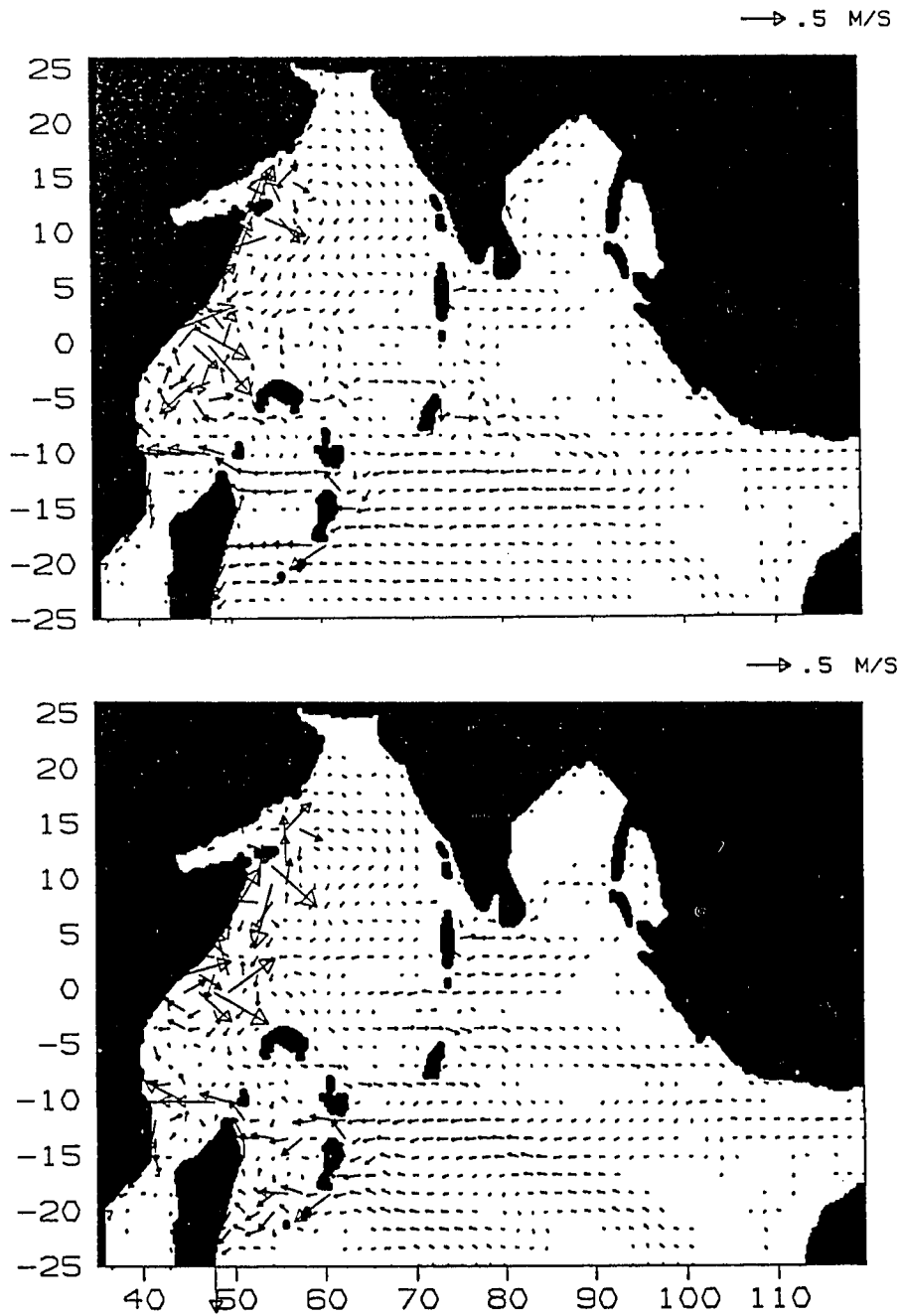
Figure 13. Current velocity in the upper layer of the Indian Ocean. Ten year average of August 16. top: 1.5 layer model. bottom: 3.5 layer model
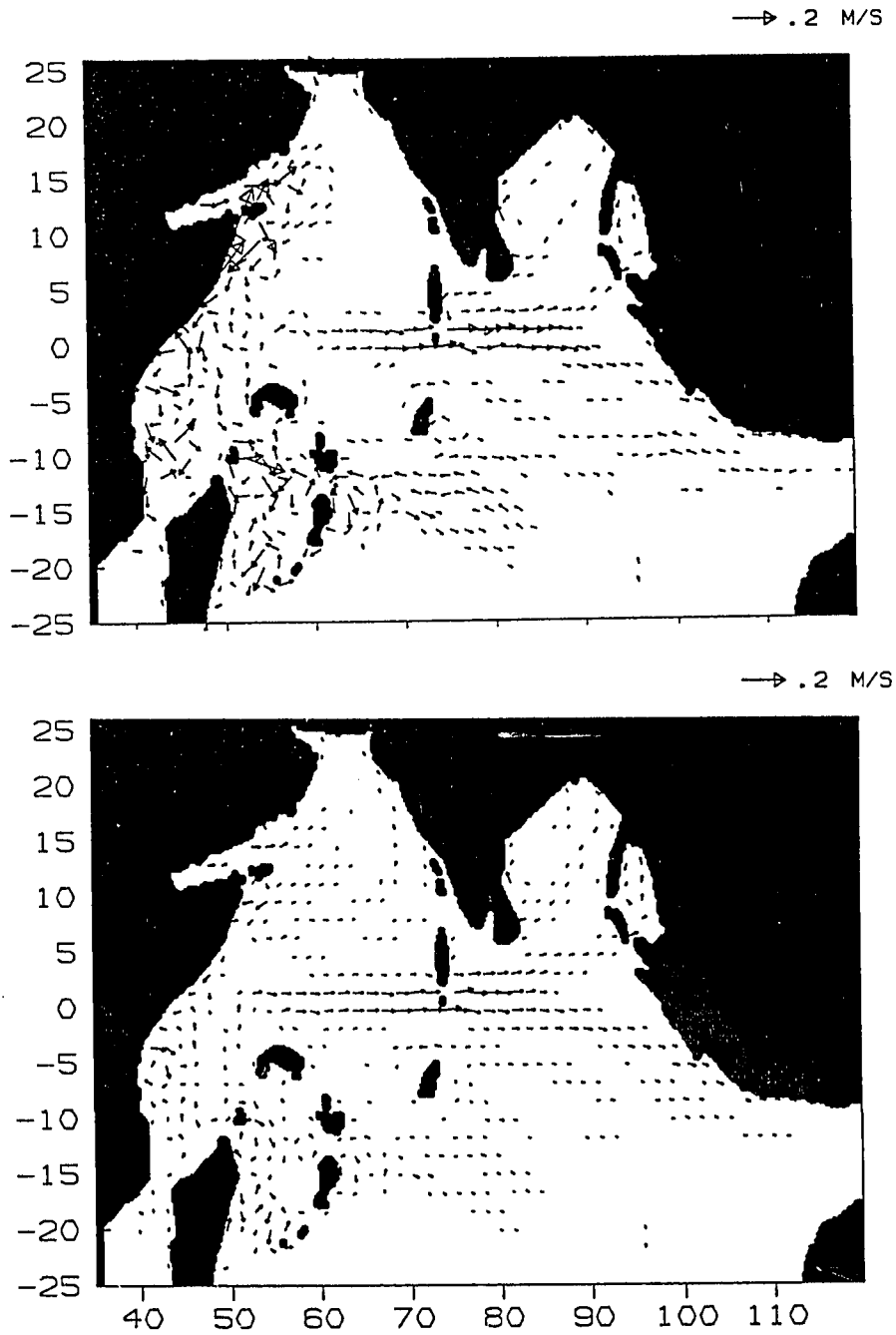
Figure 14. Current velocity in the second (top) and third (bottom) layer of the Indian Ocean. Ten year average of August 16.

Figure 15. Ten year average August 16. Depth to the bottom of layer 1
(a), layer 2 (b), layer 3, (c) and surface elevation (d) in the 3.5 layer model.
Panels (e) and (f) show the surface elevation and upper layer thickness in the
1.5 layer model.

—⊳ .5 M/S

—⊳ .5 M/S
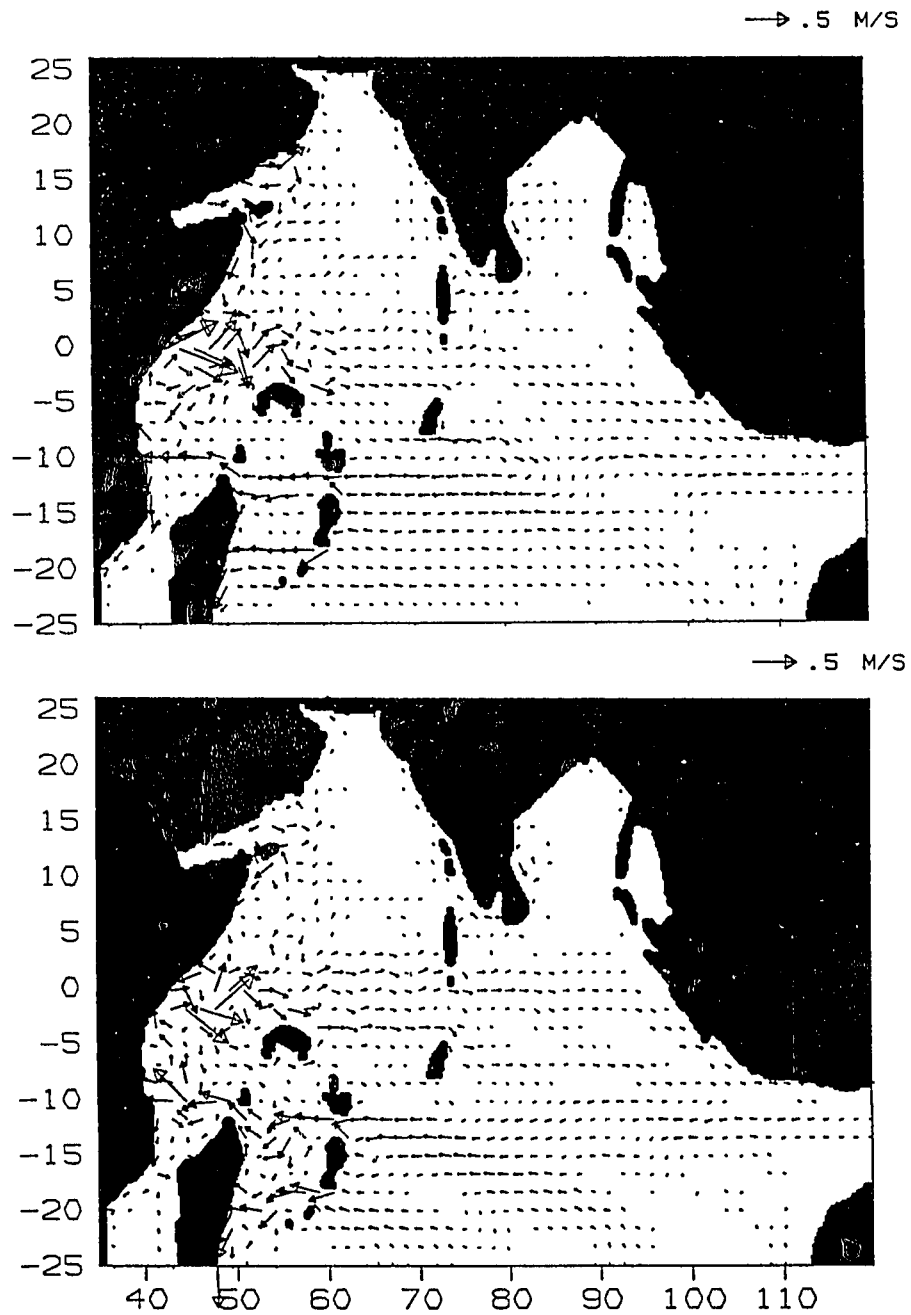
Figure 16. Current velocity in the upper layer of the Indian Ocean. Ten year average of November 16. top: 1.5 layer model. bottom: 3.5 layer model
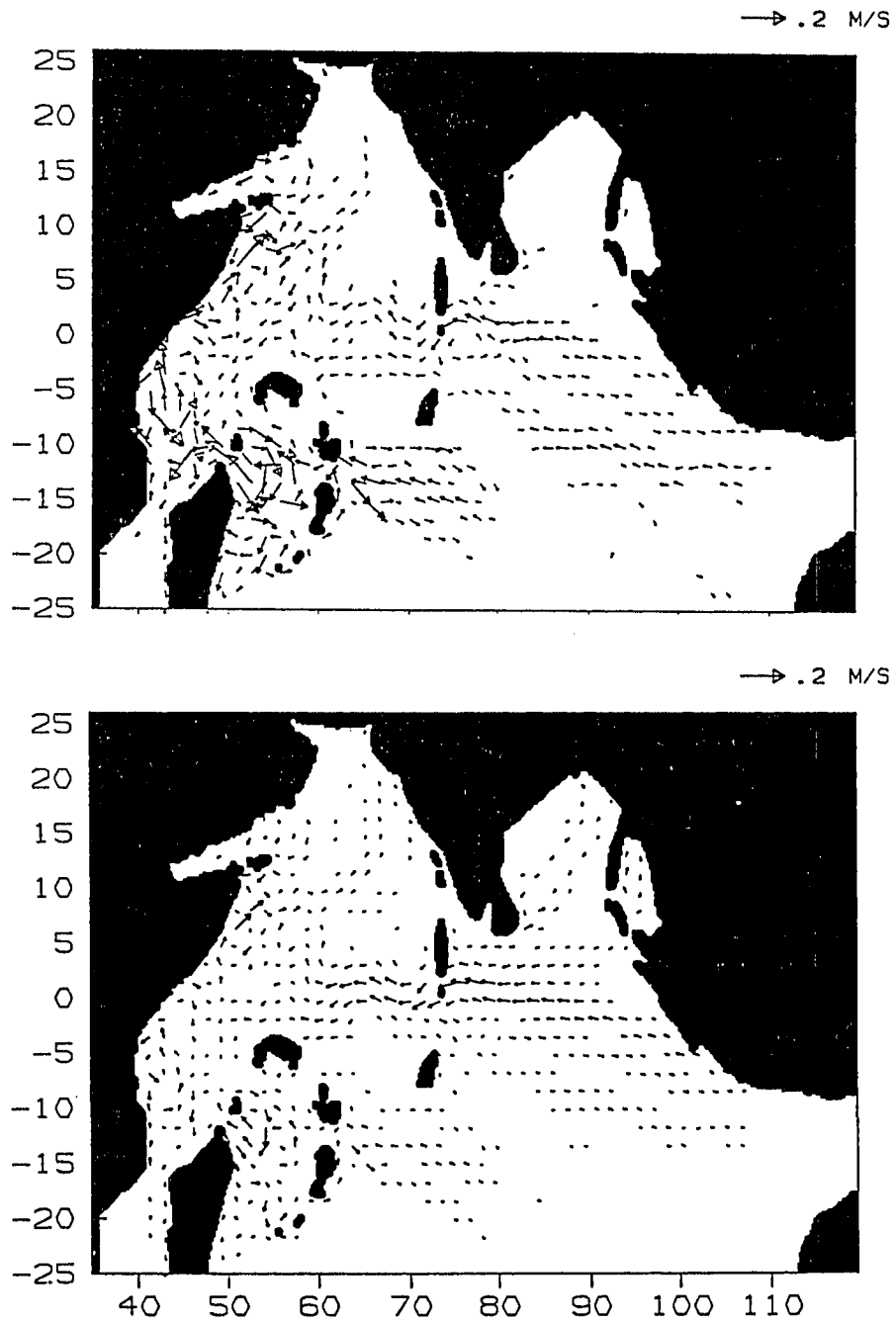
Figure 17. Current velocity in the second (top) and third (bottom) layer of the Indian Ocean. Ten year average of November 16.

37
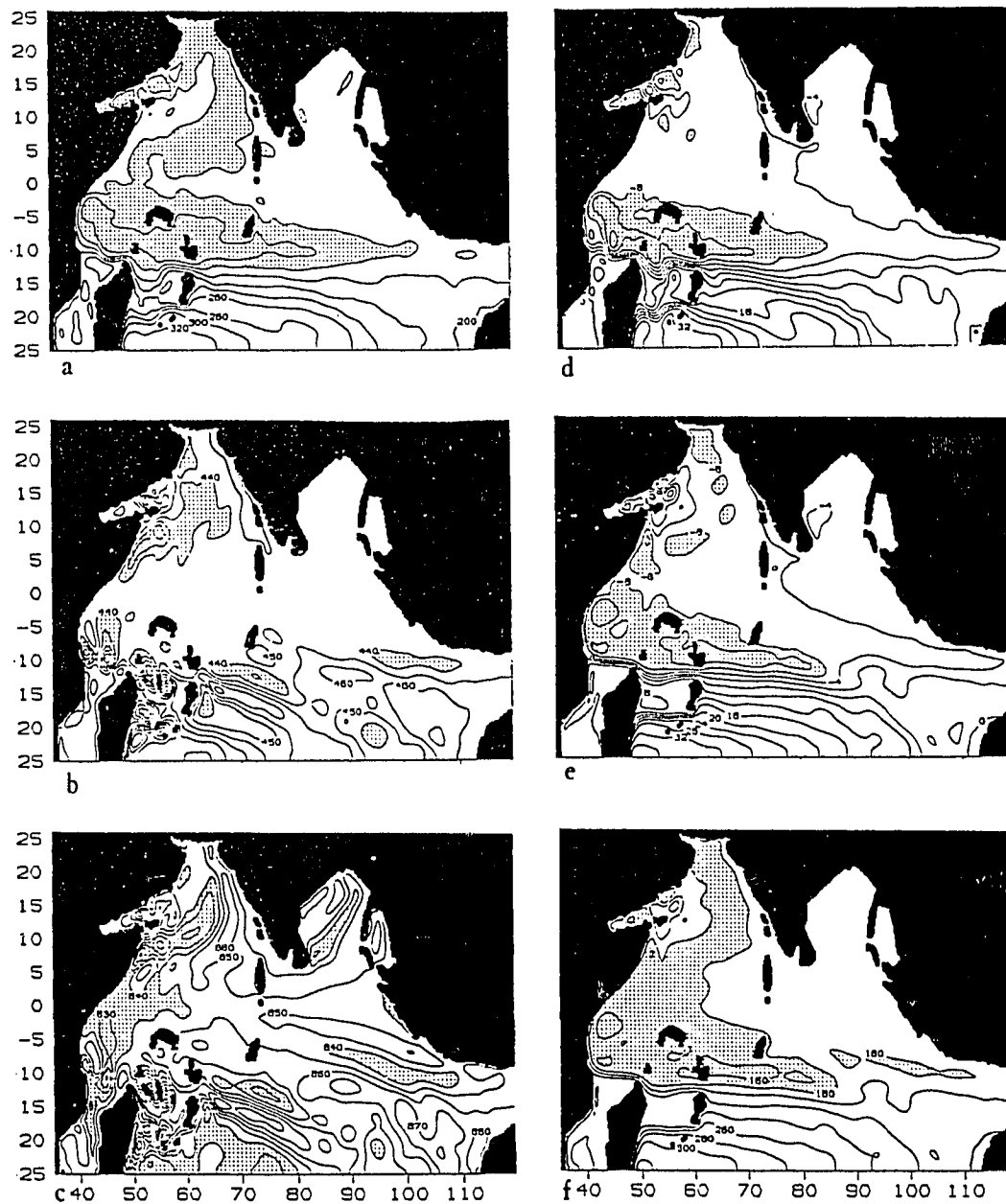
Figure 18. Ten year average November 16. Depth to the bottom of layer 1 (a), layer 2 (b), layer 3, (c) and surface elevation (d) in the 3.5 layer model. Panels (e) and (f) show the surface elevation and upper layer thickness in the 1.5 layer model.

e.g., Anderson and Moore, (1979). Its average transport at 8°S is 17 Sv in our models. The relative strength of the southward branch compared to the northward along the east coast of Madagascar is determined in part by a parameter in the open boundary condition. It was chosen in order to obtain a southward flow in agreement with observations. The average volume transport is 12 Sv in the models. A second branching is enforced at the coast of East Africa, where the strength of the southward flowing Mozambique Current relative to the East African Current also depend on a parameter choice in the open boundary condition. The southward transport is about 5 Sv. The open boundaries and the associated parameters is discussed in Appendix B.

During the winter the northern hemishere equivalent of the SEC, the north equatorial current (NEC) is present from 5°N to the equator, although it is a much weaker current. During the spring, after the first onset of the southwest monsoon in April, this current becomes erratic, and joins the Equatorial Counter Current (EEC) to the south of it, to form the eastward flowing Southeast Monsoon Current. This reaches from 3°N to 9°S, being strongest and most persistent south of the equator, in the region 2°S – 7°S, where the EEC flows during the winter. The main source of the EEC, however, is the EAC which turns offshore just south of the equator during the northeast monsoon, and north of the equator during the northern summer. In October after the transition to the northeast monsoon, the NEC returns to a westward flow. The currents in each layer, the depths of the isopycnals and the surface elevation computed by (2-9) for the two models are shown as in Fig.7-18 for February, May, August and November. The agreement for the upper layer model results and the dynamic height at 100 m relative to 1000 m in Wyrtki (1971) is good.

39

The currents in the second and third layers are in the same direction along the equator, but generally in opposite direction to the upper layer flow, e.g., second vertical mode. These deep currents change direction four times during the year (Figs. 8,11,14 and 17). At the eastern part of the ocean westward pulses of undercurrents appear in April and November, while eastward undercurrents are generated there in January and July. The patch of strong undercurrents move westward with a phase speed of about 40 cm/s, which is in agreement with linear theory for the first horizontal Rossby mode. The reversal occur first in the lowest layer indicating an upward slope to the east of lines of constant phase, e.g., upward phase propagation.

The model currents reverse with depth as in the observations of Luyten and Swallow (1976) who found an eastward upper layer flow and westward flow below in May and June 1976. The semi-annual changes in response to the Monsoon wind below the thermocline at 750 m, reported by Luyten and Roemmich (1982), and reproduced here as Fig. 19, are in excellent agreement with the model response in the second and third layer. They also found westward and upward propagation of phase. Gent, et al., (1983) presented an analytical linear model, which forced by the semi-annual zonal component of the Hellerman and Rosenstein wind stress reproduced these reversals. They found that reflection at lateral walls was essential for a realistic result.

Along the coastline in the eastern part of the Indian Ocean we have high pressure in the surface during the summer and a low during the winter. During the summer the high along the north west coast of Australia drives the southward flowing coastal Leeuwin Current. West of India, in the Bay of Bengal, a clockwise gyre is present in the late winter and early spring, while an anticlockwise circulation is found in late summer and early fall in agreement with observed flow patterns.

40
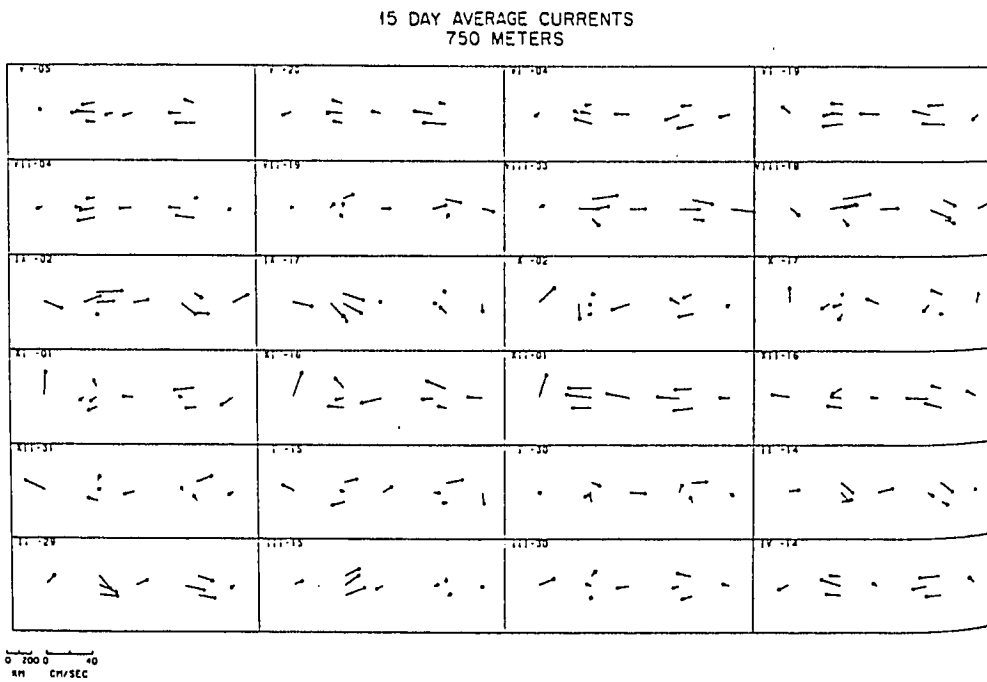
Figure 19. Time series of 15 day average equatorial current at 750 m. Data is from ten moorings from 47°E to 61°E covering the time period May 1979 to April 1980. From Luyten and Roemmich (1982).

41
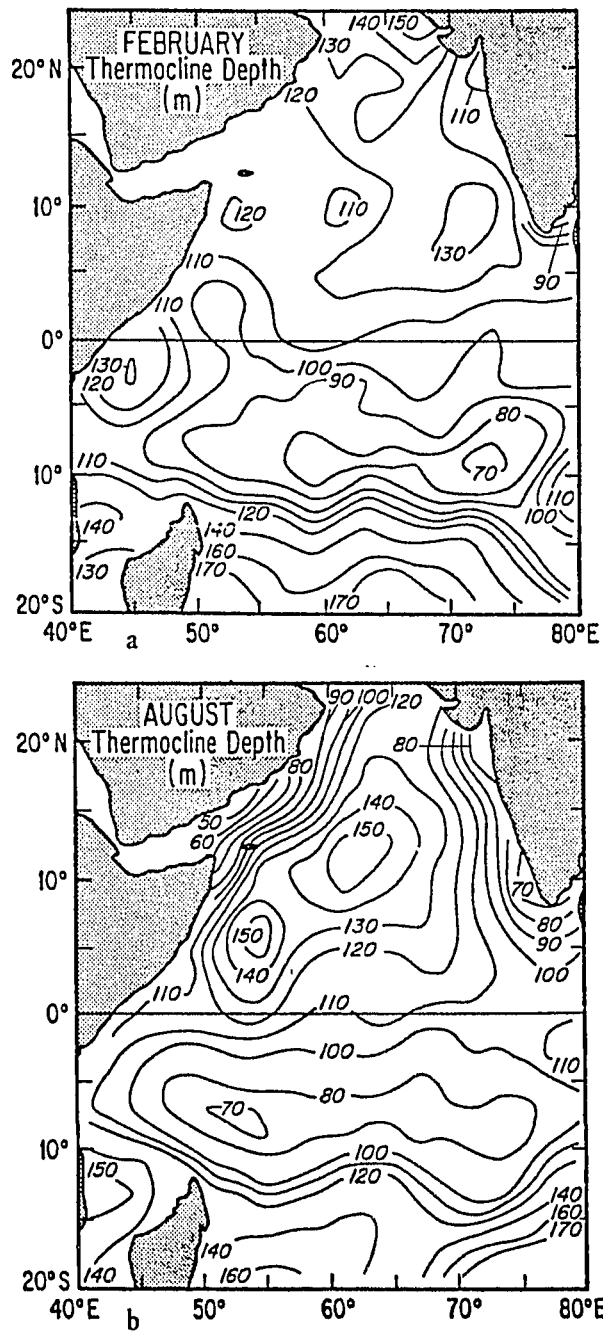
Figure 20. Thermocline depth climatology for February (a) and August (b). From Molinari, Festa and Swallow (1986).

In the Arabian Sea, west of India, a high pressure develops during the spring, creating an anticyclonic gyre in the western part of that area. In May upwelling and an associated southward current starts along the west coast of India. In June coastal upwelling is also found along the Somali Coast, and the shallowing of the thermocline is seen in the model along the coasts and the northern part of the Arabian Sea from July to October. This low surrounds a a clockwise gyre, which is found east of the Island of Socotra. It is fed from the south of the northward flowing Somali Current with an offshore return flow. These model results (Fig.9,12,15 and 18) show in general the same pattern as the climatological thermocline depths given by Molinari, Festa and Swallow, (1986). Their maps for February and August are shown as Fig. 20.

The variability due to wind forcing is clearly seen from the figures showing the total depth of the moving layers. Westward propagating planetary waves are radiated from the eastern boundaries into the interior of the ocean. For instance, annual Rossby waves are emitted from the North Coast of Australia, the Java coast and the west coast of India. The generation of highs in the winter and lows during the summer along the Indian west coast is the opposite of what would be expected from local coastal upwelling. The changes in upper layer thickness is more likely associated with the changes in wind stress curl seen over Sri Lanka. The pressure pertubation generated there will propagate northward as coastal Kelvin waves with westward radiation of planetary waves, (see for instance, Gill, 1982). At the western boundary reflection causes the wave length to decrease by a large factor (e.g., Pedlosky, 1979), which explains the small length scale and eddy activity seen along that boundary. Partial reflection takes place where islands are included in the model.

At the equator near the western boundary we find the highest variability in the model solution. The solution show strong oscillations from July to February in the meridional velocity component, (Fig. 21).

From the figure we find a period of 28 days and a westward phase velocity of 37 cm/s, corresponding to a wave length of 900 km. The group velocity is about 30 cm/s and eastward. The phase in the third layer leads the second layer which implies upward phase propagation, and accordingly, downward energy propagation. Using these values in the linear dispersion relation for equatorial waves, we can identify the oscillation as mixed planetary-gravity waves (often referred to as Yanai waves). Observations show that such oscillations are found in all oceans, (see Weisberg, 1987, for a review). They were first observed in the Indian Ocean by Luyten and Roemmich, (1982). Kindle and Thompson, (1989) studied the Yanai waves in detail using their 1.5 layer reduced-gravity model of the Indian Ocean. They forced the model by the original Hellerman and Rosenstein wind stress and found periods in the range 20–30 days and wave lengths from 800 km to 1400 km. The generation was attributed to barotropic instability of the Southern Gyre during the summer monsoon and associated with meandering of the East African Current during the winter. Maps of potential vorticity for year 21, shown in section 3.4, show that the nessessary condition for this type of instability is satisfied, so the same mechanism is suggested to be responsible in the multiple layer case.

The model solution is not strictly periodic. A comparison of individual years shown that eddies and currents appear at slightly different times and positions, although the overall pattern is the same. This internal variability is illustrated for February 16 and August 16, Fig. 22 and Fig. 23, by the variance of the velocity and standard deviation of layer thickness anomalies from the average fields at these dates taken over the last ten years of integration. The first quantity can be regarded
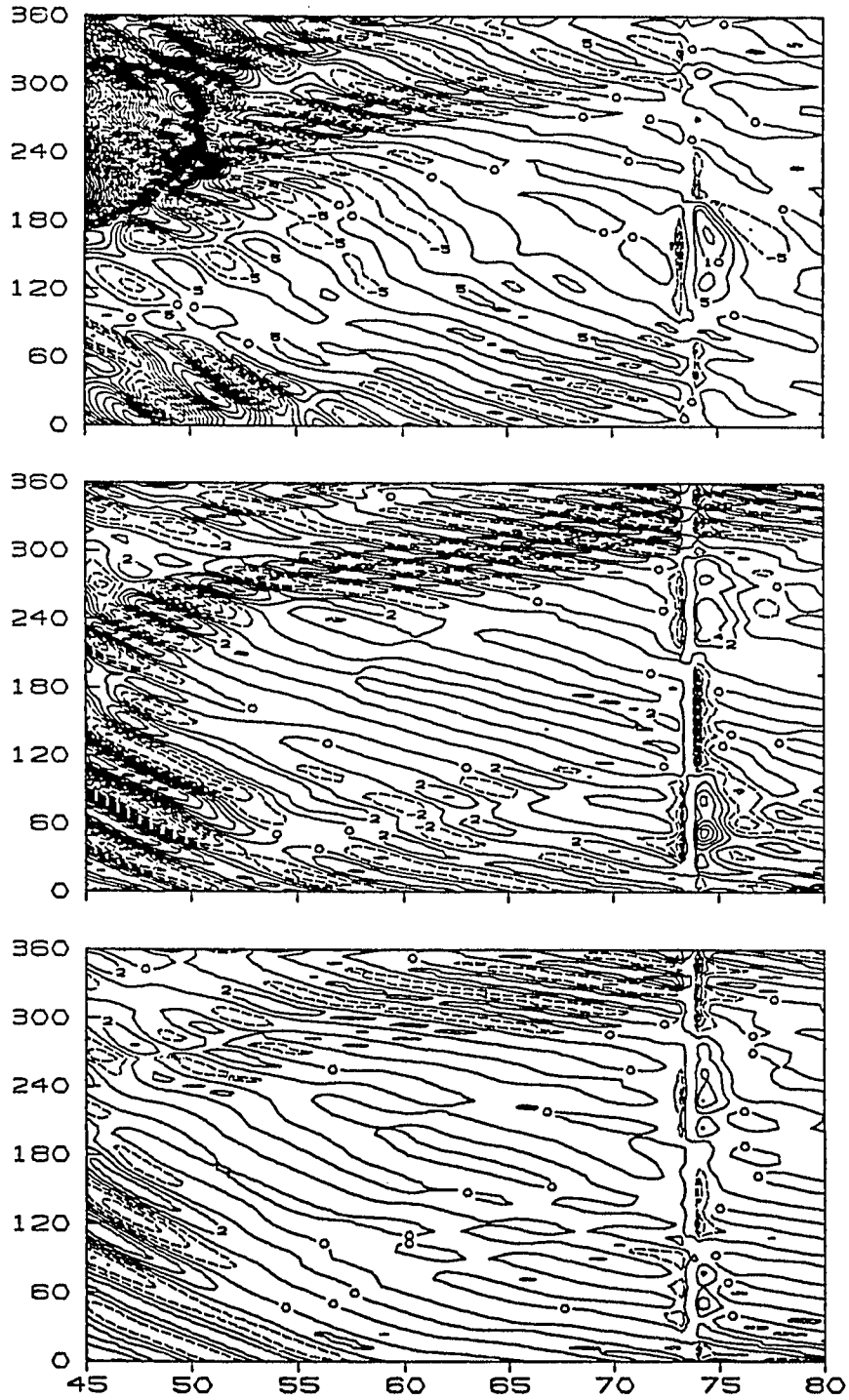
Figure 21. Longitude-time plot along the equator of the meridional velocity component (cm/s) in layer 1 to 3 (top to bottom).

45
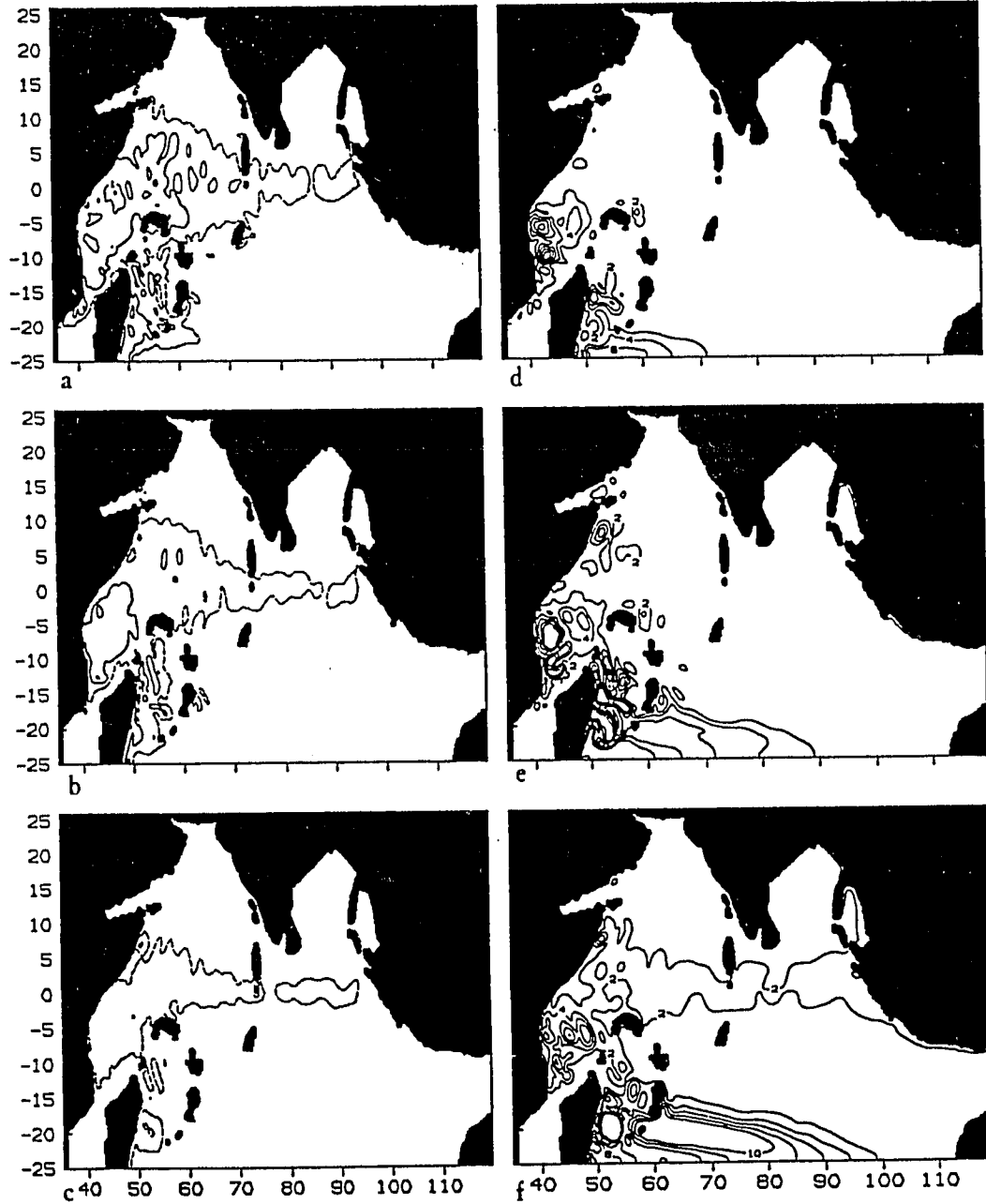
Figure 22. Based on ten year simulation of February 16: $\log_{10}$ of the velocity components (m/s) in layer 1 to 3, (panel a-c). Standard deviation of layer thickness 1 to 3, in meters, (panel d-f).

46
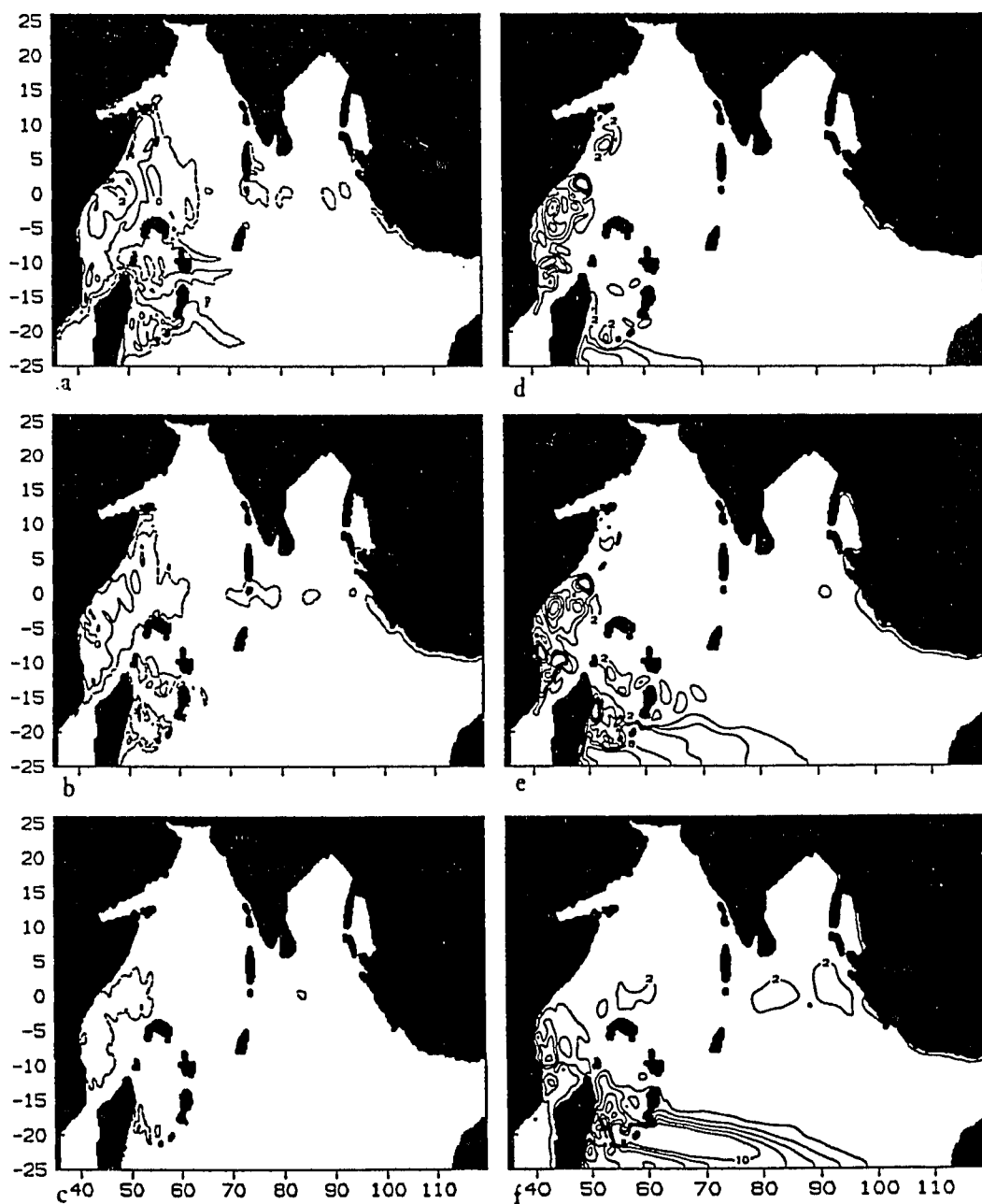
Figure 23. Based on ten year simulation of August 16: log_{10} of the velocity components (m/s) in layer 1 to 3, (panel a-c). Standard deviation of layer thickness 1 to 3, in meters, (panel d-f).

as proportional to an eddy kinetic energy, while the latter is related to the square root of the eddy potential energy. The variability in the western equatorial region is highest in the winter and is caused by the Yanai waves discussed above. In the Somali current we find that the solution is nearly periodic. The variation in upper layer thickness show the same pattern found by Luther and O'Brien, (1989) for their 1.5 layer model. Along the east coast of Madagascar we find high values in the layer thickness deviation, in particular in the lower layers. The natural variability may not be as large as shown, if the model is not fully spun up after 11 years in the southernmost part of the basin. However, the recent numerical calculation of the world ocean circulation by Semtner and Chervin, (1988), using the annual mean of the Hellerman- Rosenstein wind stress, exhibits strong eddy activity in that region.

The upper layer solution of the 1.5 layer model is not much different from the 3.5 layer solution. A comparison of the surface elevations, depth of the upper layer thickness and the upper layer currents show little differences in the large scale circulation. Since the initial value of the phase speed of the first baroclinic mode differs by about 20%, an the very long integration taken into consideration, this result is not obvious. Further it should be noted that the results from this 1.5 layer model are nearly identical to those presented by Woodberry, et al., (1989) although frictional terms and open boundary conditions are implemented differently.

3.2. Upper layer flow of the Somali Current

Here the results of both the 1.5 layer model and the 3.5 layer model will be presented. An average of the flow from year 10 to year 20 of the spin up will be discussed in this section. The discussion of the result are based on the 3.5 layer version, but differences in the solution of the single layer model are pointed out.

The model produces a southward Somali Current from November through March. The current is approximately 150 km wide, with a typical alongshore speed

of 20 cm/s, and extends as a continuous current from 10°N to the equator in that period. During January to March the current is southward to 2°S, before it meets the northward flowing East African Current and turns offshore into the equatorial counter current. The maximal southward transport, 14.4 Sv, occurs in the end of January in the 3.5 layer case. With one layer the maximal transport is 8.6 Sv in early December.

The Somali Current is fed by on shore flow along 10°N and an inflow perpendicular to the coast at 5°N. These model results for the winter Somali Current match the observations as given in the introduction, or as presented in the dynamical height charts by Wyrtki (1971). The single layer model has a southward flow only to the beginning of March, and an offshore northward flow not found in the climatological charts. The reason for this difference in models behavior is due to differences in response to the decay of the summer monsoon and will be discussed later.

During the northeast monsoon, the model has a decaying cyclonic eddy north of Socotra, while a weak anticyclonic gyre just south of the island intensifies. With one layer the circulations are in the opposite directions (Fig. 24). Judging from thermocline depth observations of Molinari, et al., (1986a,1986b), the multi layer result is the most realistic. The annual variation of the thermocline depth exhibits a maximum in March and a minimum in September with an amplitude of 35 m. The model calculations show an amplitude of 30 m, but the maximum thickness occurs in January in the 1.5 layer case.

During the transition period to the southwest monsoon, from March to early May, the multilayer model results are not in as good agreement with the observations. The weak northward surface flow, north of 5°N in March, and along the entire coast in April as shown in climatological maps and corroborated by

Schott and Quadfasel (1982) with current measurements during 1979, is missing in that version of the model. Schott (1983) attributes this to "strong wind stress curl distribution off Somalia," but the wind stress used to force the model show no evidence of such curl and one can expect that the lack of this early onset may be due to insufficient spatial and temporal resolution of the winds. However, the single layer version does have northwards currents north of $5°$ at that time. The early onset of the summer monsoon in April, due to local northward winds south of the equator as reported by Leetmaa (1972,1973) is seen in the model solutions.

In May and June coastal upwelling starts a few degrees north of the equator and is later found along all of the Arabian Peninsula. The currents are to the north along the coast. Since the local wind stress is strong at this time, we can expect the models to give similar results as seen in Fig. 25. The Great Whirl forms and migrates to the north during July and August and the anticyclonic Socotra eddy forms east of that island. The observations show that the Socotra eddy forms regularly each year at this time, and that its high salinity distinguish it from the Great Whirl (Bruce, 1979). In the model solution the eddy forms between the northeastern branch of the Somali current and a return flow from the north. Its potential vorticity corresponds to a higher latitude than that of the Great Whirl, which suggest that it consists of different water mass. The southern gyre, with offshore flow just north of the equator (Fig. 26) is seen in the solution during the entire summer. At the height of the Monsoon the offshore flow is at $2.5°N$ in agreement with observations. Fig. 27 shows the detailed observations of the surface currents and salinity from 1979.

In most years a northward migration of the southern gyre followed by a merging with the Great Whirl is observed (Swallow and Fieux, 1982). This does not happen in this simulation. Using a 1.5 layer model very similar to the one used
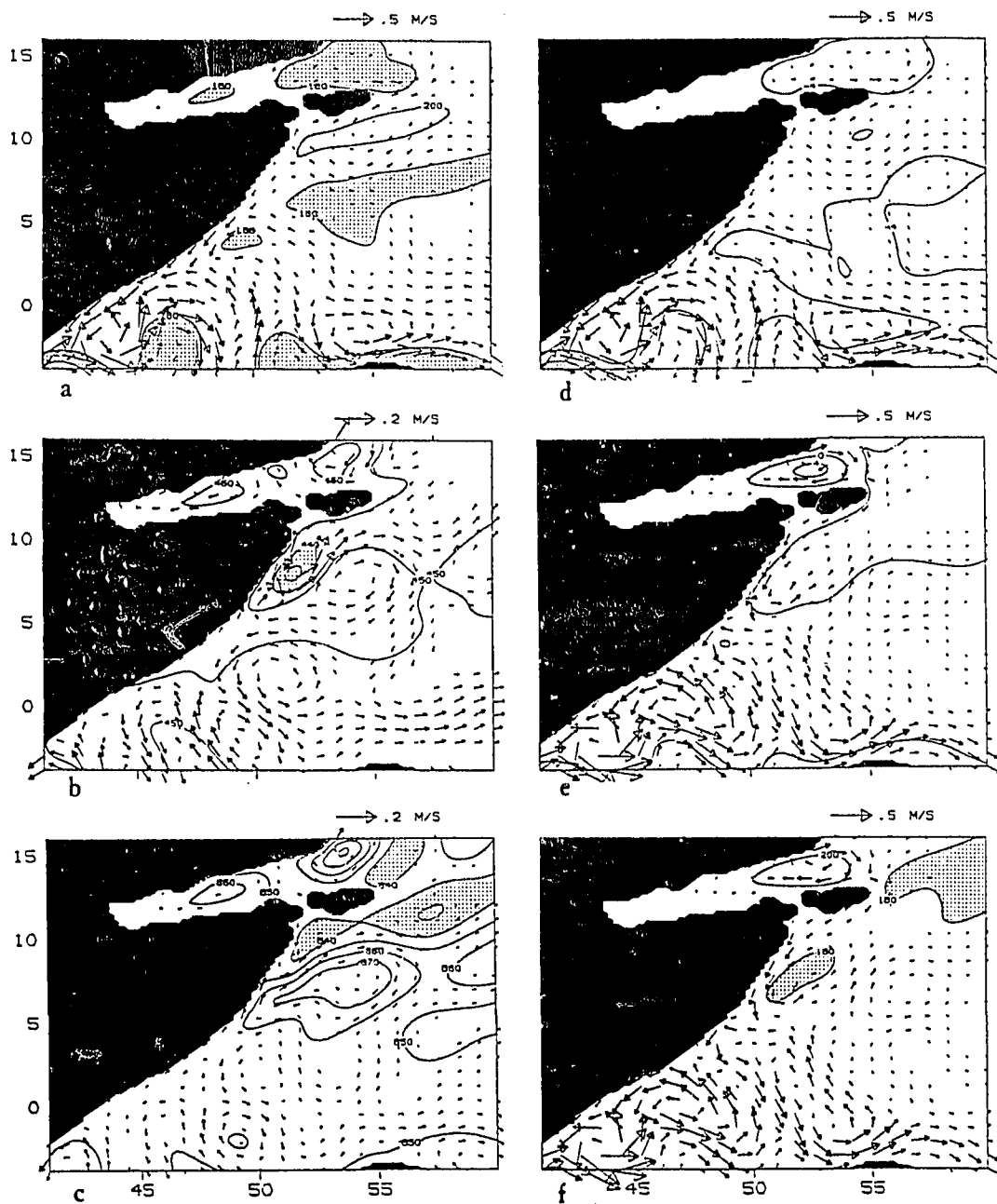
Figure 24. Ten year average February 16. Velocity and depth to the bottom of layer 1, (a), layer 2, (b), layer 3, (c) and surface elevation, (d) in the 3.5 layer model. Panels (e) and (f) show the surface elevation and upper layer thickness with velocity vectors in the 1.5 layer model.

51
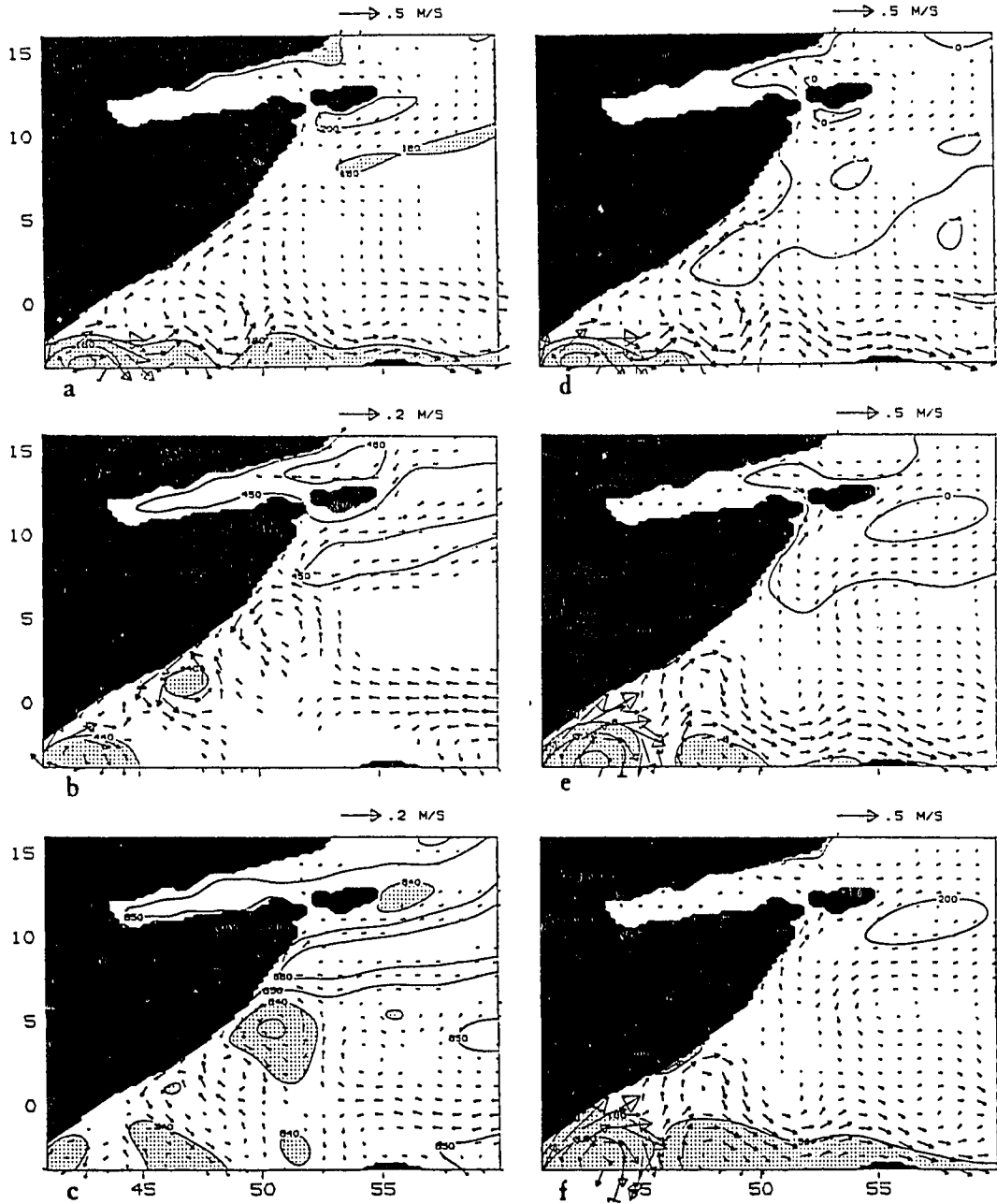
Figure 25. Ten year average May 16. Velocity and depth to the bottom of layer 1, (a), layer 2, (b), layer 3, (c) and surface elevation, (d) in the 3.5 layer model. Panels (e) and (f) show the surface elevation and upper layer thickness with velocity vectors in the 1.5 layer model.

52
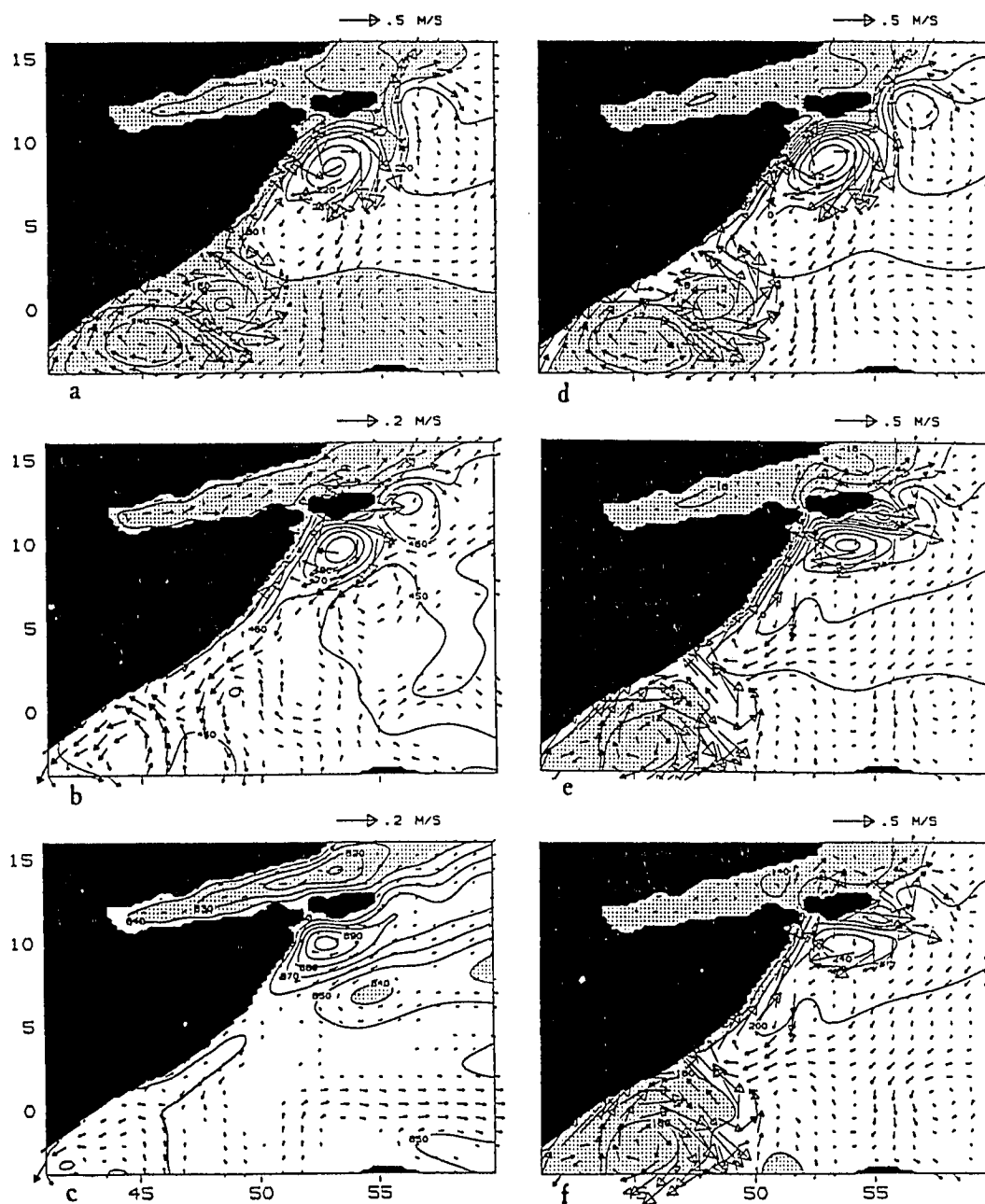
Figure 26. Ten year average August 16. Velocity and depth to the bottom of layer 1, (a), layer 2, (b), layer 3, (c) and surface elevation, (d) in the 3.5 layer model. Panels (e) and (f) show the surface elevation and upper layer thickness with velocity vectors in the 1.5 layer model.
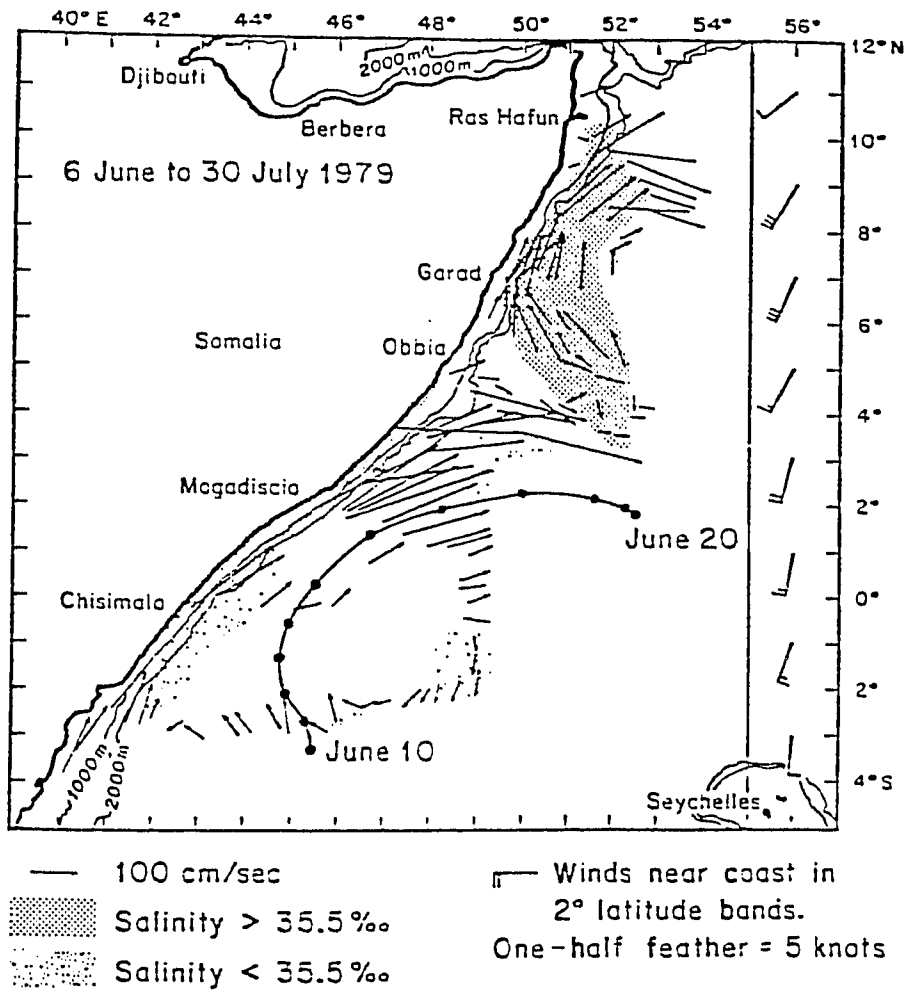
Figure 27. Observed surface current vectors, salinities and a drifter trajectory during June-July 1979. Surface winds are shown in right panel. From Düing, Molinari and Swallow (1980).
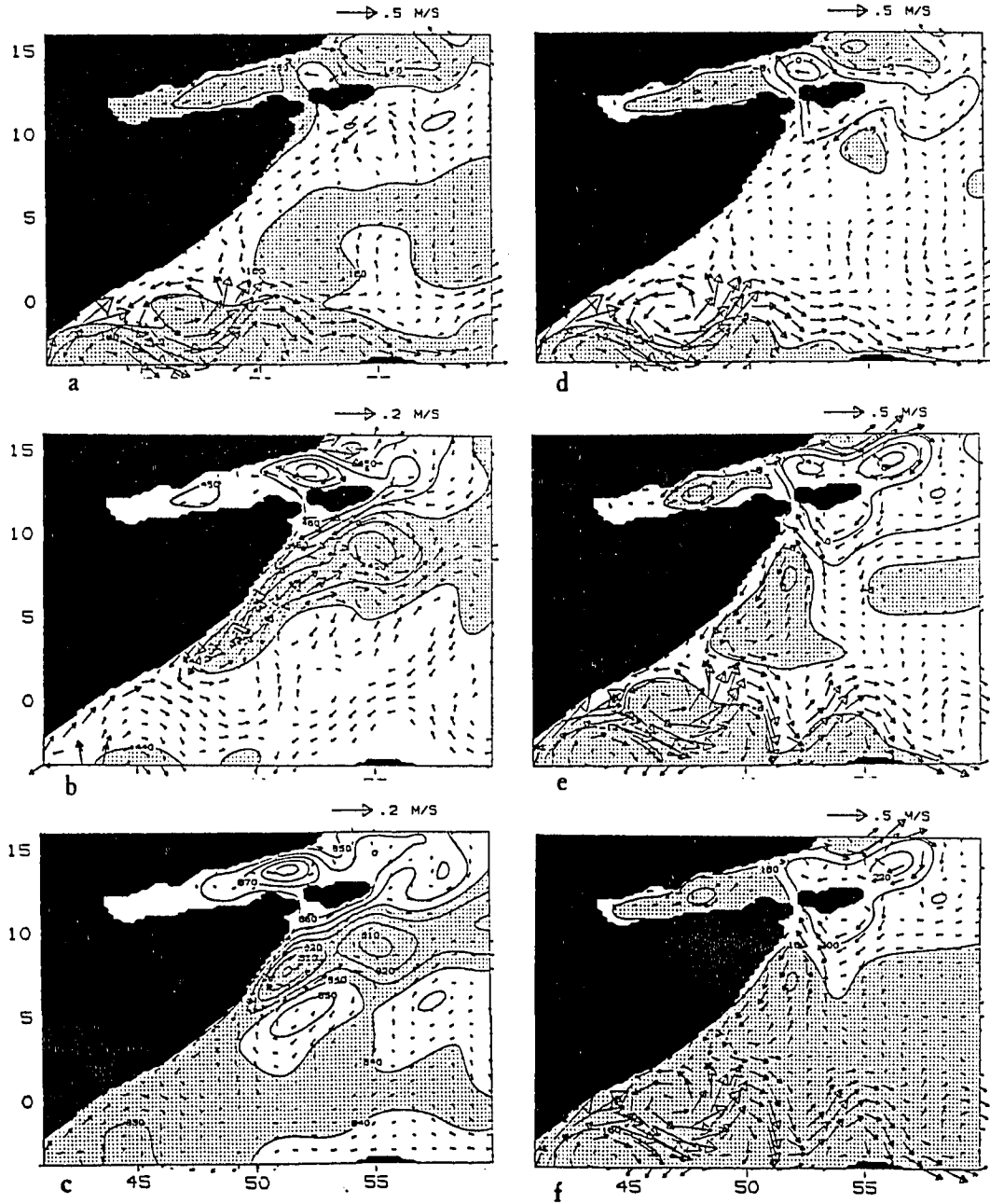
Figure 28. Ten year average November 16. Velocity and depth to the bottom of layer 1, (a), layer 2, (b), layer 3, (c) and surface elevation, (d) in the 3.5 layer model. Paneis (e) and (f) show the surface elevation and upper layer thickness with velocity vectors in the 1.5 layer model.

here, Luther and O'Brien (1989) produced this merging when applied to observed monthly wind for most years. However, using the same model merging did not occur when the Hellerman and Rosenstein wind stress was applied as forcing, (Luther, personal communication). The results here, in spite climatological averaged winds are used, does therefore correspond to the less common situation where the southern gyre stays near the equator. During the summer the transport in the model reaches a maximum northeastward transport of 19.2 Sv in July with three layers. The 1.5 layer version has a maximum of 18.3 Sv in August.

In September a cyclonic eddy is created between the Great Whirl and the Socotra Eddy, after a wedge of cold water is advected offshore by the Great Whirl. At this time the two versions of the model starts to show different results. In the single layer case a small anticyclonic eddy forms north west of Socotra. In October the 3.5 layer version still has a northward Somali current, and the Great Whirl has weakened considerably. With one active layer, the whirl is stronger, positioned further north and northward flow is confined to north of 5°N.

In November the northeast monsoon has arrived, but a northward coastal flow is still found north of 7°N as indicated by observations. In the multilayer version, the anticyclonic eddies have essentially disappeared, while they are still present in the single layer model (Fig.28).

The main reason for these differences between the 1.5 and 3.5 layer model during the transition from summer to winter monsoon, is that kinetic energy can be transferred vertically in the latter version. During this time we see that the currents in the second and third layer are strongly accelerated.

3.3. The undercurrents off Somalia

The observations of the subsurface flow are sparse. Adding to this the fact that the horizontal correlation scale decrease from 160 km at the surface to 90 km

at 700 m, (Leetmaa, et al., 1980), our knowledge of the actual undercurrent are unfortunately rather limited. Furthermore, observations from shipboard profiling obtained in May 1979, differs from the long term measurements composed of current meter records near 5°N (Quadfasel and Schott, 1983, Fig. 29).

Recent results, Schott (1987), from the French-U.S. cooperative program in the western Indian Ocean show that the undercurrents at the equator differs from these current meter results. The model results in the lower layers are displayed in Figs. 24, 25, 26, and 28.

The narrow undercurrents require very fine resolution of the numerical model, and no ocean model is available which can reproduce all observations. This is also true for the present study, but as will be clear from the discussion below, the model results are in agreement with many of the observed characteristics of the undercurrents.

During the winter monsoon, from the onset in November until it weakens in February, a subsurface cyclonic gyre in the model solution is causing a southward current along the Somali Coast. It reaches from from 10°N to 2°N in November and is weakening with its northern latitude decreasing to 7°N in mid February. The flow turns offshore and returns north about 200 km away from the coast. At the equator the deeper currents are northward except for December. In January and February the northward flow is very weak. Quadfasel and Schott's (1983) results from 5°N show a continuous southward flow. The model flow does not quite reach that far south during the last month. On the other hand the rather strong southward flow during December in the model's deeper layers is in contrast to the observations.

A remarkable agreement is found between the structure of the model currents for February and the measurements by Bruce and Volkmann (1969). They found a deep cyclonic subsurface eddy with maximum velocities at 52.5°E (to the
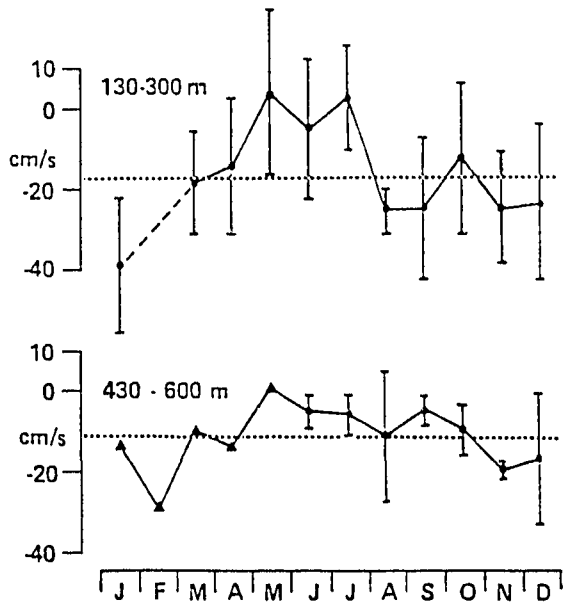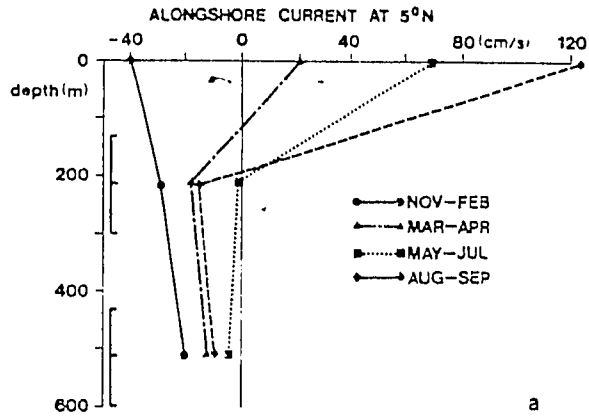
Figure 29. Observed alongshore currents at 5° N based on all available complete monthly values from 1975 to 1979. (a): Vertical profiles, (b): Time series at two levels. From Quadfasel and Schott, (1983).
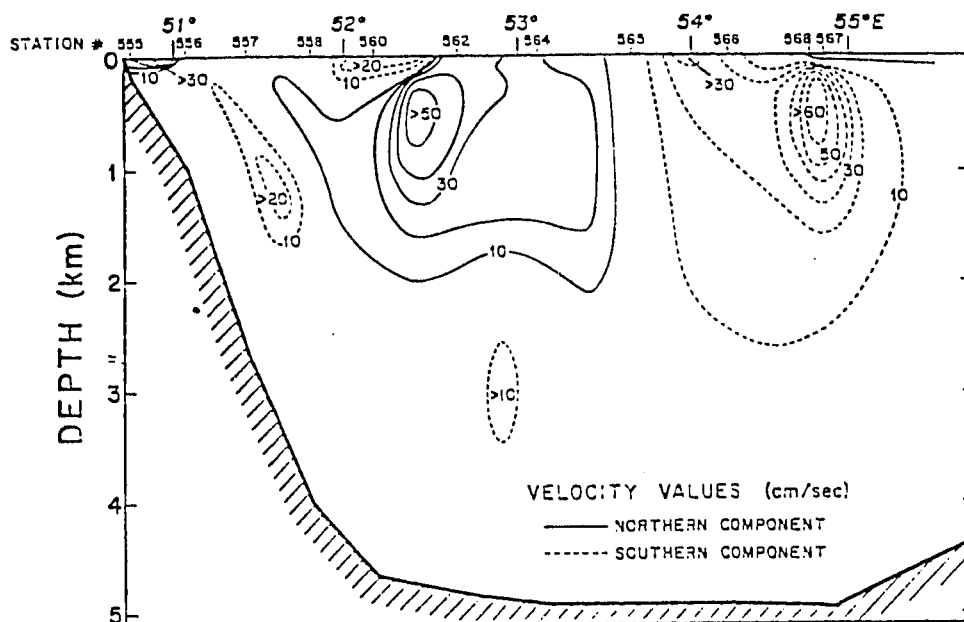
Figure 30. Deep eddy observed in February to March 1965 along 9° N. Geostrophic currents are based on hydrography with reference level obtained from neutrally-buoyant floats. From Bruce and Volkmann, (1969).

north) and at 55° (to the south), with a weaker southward current (Fig. 30). This is position where the Great Whirl is found in the late summer. It has therefore been suggested, that since the surface currents of the Great Whirl can be observed a couple of months after the summer monsoon weakens, this submerged eddy might be the remnants of the Great Whirl, which persisted beneath the surface, Knox (1987). It will be clear from the model results shown later, that such a scenario is not supported by the present calculations.

As discussed in the previous section, the upper layer currents are not simulated very well in March and April, so discrepancies may also be expected in the layers below. In March we find in the second layer a northward undercurrent north of 5°N and south of 1°N, with southward flow in between, caused by an cyclonic eddy connected with strong cross equatorial flow. An equatorial undercurrent with eastward velocities of 10 cm/s are found east of 50°E in the second layer, while southwestward flow is found at 7°N. The latter turns westward in April and the cyclonic eddy moves a couple of degrees northward. The equatorial undercurrent has nearly disappeared at this time. Schott and Quadfasel (1980) reported mean current reversals along the coast during the spring. At 5°N and 7°N the mean current was southwestward, but at 6° a northeastward flow was observed. The climatological results given in Quadfasel and Schott (1983) suggest a southwestward current of 15 cm/s at 5°N, found in the model only where the cyclonic eddy touches the coast. The complicated flowpattern in the model suggests that the alongshore intermediate flow may depend very much on the location along the coast.

In May and early June the upper layer flow is northeastward, and an undercurrent is found south of 6°, but not north of that latitude where an onshore undercurrent is seen under offshore surface flow. A westward equatorial jet develops in May and last through July. This jet was observed in May and June in 1976 and

during INDEX in 1979 (Leetmaa, et al., 1980, 1982). The authors of the second paper observed a splitting of the equatorial undercurrent into a northeastward and southeastward branch before it reached the coast, with an intensification of the undercurrent in June. The model show the same flow pattern. The disappearence of the model coastal undercurrent in June is possibly caused by arrival of this equatorial flow. However, the increasing northward winds, causing coastal upwelling, set up an onshore pressure gradient, which help decrease the southward deep flow. Quadfasel and Schott (1983) found that the Somali undercurrent ceased in May. The observations in 1979 by the same authors, Schott and Quadfasel (1980), show a reversal from southwestward to northeastward currents in early July.

A relatively detailed synoptic map of the flow at 700 m between May 10 and June 4 1979 is given by Leetmaa, et al., (1980) and reproduced here as Fig. 31. This should be compared with the model solution in Fig. 33 from May 28 year 21 of the integration. We notice that the actual currents are larger than in the model by a factor of 3 to 4 or more. However, the directions are in good correspondance with the observed flow. There is offshore flow north of 8°N, onshore south of that latitude with northward coastal flow between. We have onshore flow at the equator with southward currents along the coast. The observed flow from 2°N to 5°N is not well resolved, but exhibits a spatial structure not inconsistent with the model results. The northward undercurrent in the model is also in agreement with the findings by Schott (1987). However, the branch of the clockwise gyre that produce this flow in the model is further south in early May.

Since deep currents are relatively weak, linear theory should be adequate to explain the results, unless of course the deep flow is caused by instabilities. For this reason it is encouraging that the spatial pattern and direction of the currents in the lower layer agree with the observations. To pursue this further, we will consider the
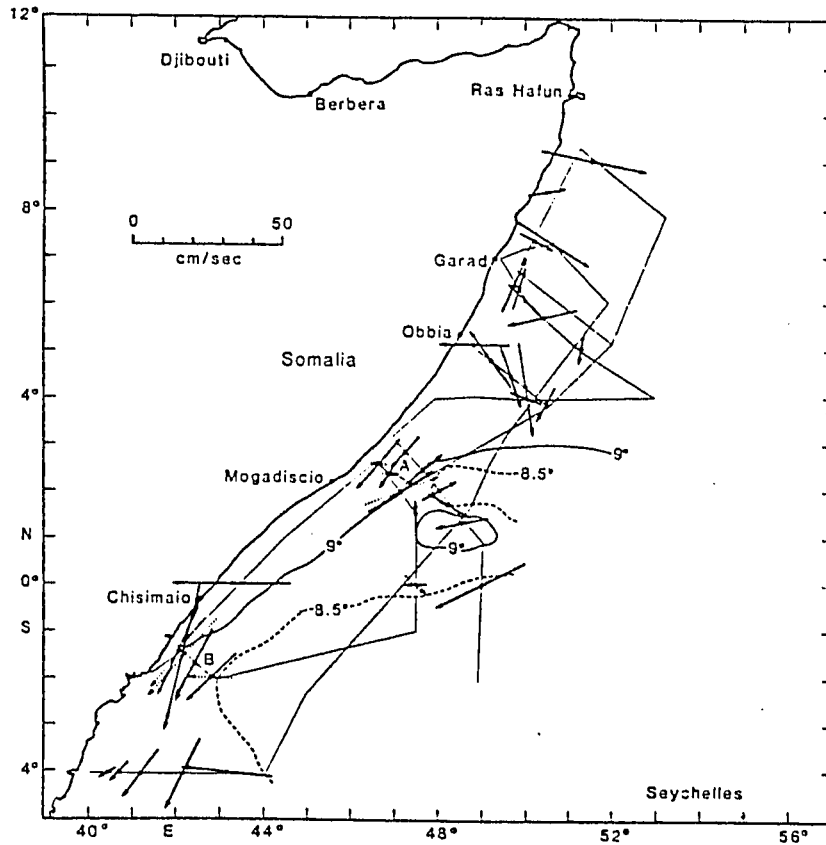
Figure 31. Velocities at 700 m. Solid arrows represent data observed between May 16 and 22, 1979. Dashed arrows indicate data from May 26 to 31, 1979. Temperature was measured along ship track (light line). From Leetmaa, et al., (1980).
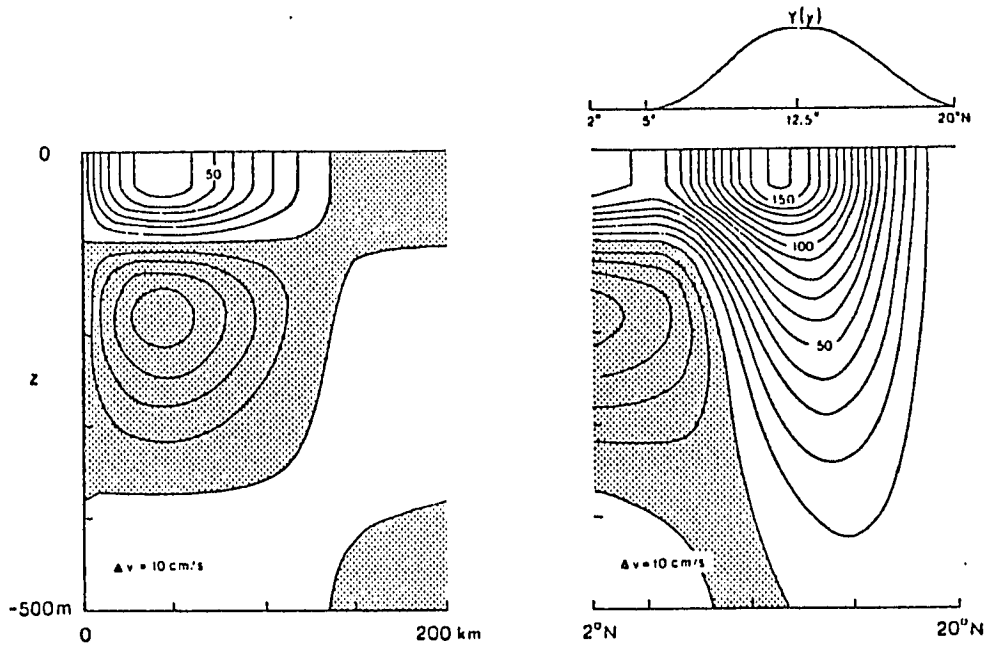
Figure 32. Linear mode solution. Section perpendicular to the coast at 5° N (left panel) and section of alongshore flow 44 km from the coast. The magnitude of the alongshore wind stress is shown above (right panel). Contour interval is 10 cm/s. Shaded areas indicate southward flow. From McCreary and Kundu, (1985).

linear theory of McCreary and Kundu (1985). Using separation into normal modes they solve the steady problem along a western boundary forced by local alongshore winds north of the equator. Their solution should be valid during the initial phase of the summer monsoon when local forcing is dominating and before non-linear effects become important. Fig.32 show their solution. A southwestward undercurrent is found only to the south of the wind forcing. They found that onshore deep flow along the southern edge of the wind field separated into a northward and southward branch at the coast. We also note that offshore countercurrents are present in their solutions. The numerical model solution from May 28, year 21 (see Fig. 33, next section) show the same features.

During July and August the Great Whirl moves northward and deepens to reach all three layers in the model. There is no undercurrent north of the equator, which agrees well with the July observations of Quadfasel and Schott (1983). However, a southward recirculation develops offshore and moves westward, which produces a southward coastal undercurrent in September. The observations show an onset in August. The southward undercurrent reach to 4°N where it turns offshore into an eastward equatorial undercurrent.

In September a cyclonic eddy forms between the Great Whirl and the Socotra eddy and the flow changes rapidly. It will be clear from the figures shown in the next section, that the eddies are tilted with depth, the warm eddies to the northwest and the cold to the south. In October the Great Whirl has collapsed and the deep part been replaced by a large subsurface cyclonic eddy. The formation of this flow will be further discussed in the next section.

3.4. The Great Whirl

The results after 20 years of spin up will be used in this section to analyze the generation and decay of the Great Whirl. The model result was recorded every

6 days and most of the conclusions are based upon observing a computer animation of the evolution, and may not be obvious from the figures shown here. The results from the 1.5 layer model are also from year 21 of the integration. We define the following diagnostic quantities to be used in the subsequent analysis:

Vertical component of the relative vorticity in layer j:

$$\zeta_j \equiv \nabla \times \vec{v}_j \qquad (3-1)$$

where $\vec{v}_j$ is the velocity vector in layer j and $\nabla\times$ the curl operator in spherical coordinates.

Vertical component of the absolute vorticity in layer j:

$$\zeta_{aj} \equiv \zeta_j + f \qquad (3-2)$$

where f is the Coriolis parameter.

Vertical component of the potential vorticity in layer j:

$$\Pi_j \equiv \zeta_{aj}/H_j \qquad (3-3)$$

Kinetic energy per area unit for each layer:

$$E_{kin,j} \equiv \frac{1}{2}\rho_j \vec{v}_j H_j \qquad (3-4)$$

which is the vertical integral of the kinetic energy density.

Available potential energy:

$$\mathcal{A} \equiv \frac{1}{2}g\left((\rho_1 - \rho_a)\eta + \sum_{j=1}^{N-1}(\rho_{j+1} - \rho_j)(H_j - H_{0j})\right) \qquad (3-5)$$

where ρ_a is the density of air and η the surface elevation and H_{0j} the layer thickness of the ocean at rest. The first term which involve the free surface is negligble compared to the contribution from the isopycnal displacements of the deeper layers.

Different levels of zero available potential can be chosen. Here a constant have been preferred compared to a background field, *i.e.*, a climatology, which may vary in time and space.

The evolution of the flow during the summer monsoon is shown in Fig. 33-48. A velocity vector is shown for each layer for every 16 grid points in the model, i.e., 0.8° between the vectors. These plots show also the depth to the bottom of each layer. For the first layer this is simply the layer thickness, which corresponds to the thermocline depth in this model. For the second layer this depth is the sum of the thicknesses of layer 1 and 2, while the 3. layer depth is defined as the total thickness of the active layers. The surface elevation, which is proportional to the dynamic pressure for the first layer, is calculated according to (2-9) and shown with the velocities for layer 1. The quantities defined above are shown for the same dates and help identify dynamic active regions. For instance, westward propagating Rossby waves are seen in the relative vorticity maps than in the velocity and pressure fields.

In late May and early June, Fig. 33 and Fig. 34, the Somali Current is well developed. The flow split in a northward and offshore branch at 6°N. The latter turns southeastward, but no closed eddy is formed. This flow is associated with a local surface depression to the north of that latitude. A westward equatorial undercurrent dominates the flow in the two deep layers. The available potential energy is low except in the gyre south of the equator.

By June 16 it is clear that a weak eddy has formed offshore at 5° N, (Fig. 35). Using a three-dimensional numerical model with a meridional coast, Cox (1976) showed that mean kinetic to eddy kinetic energy transfer took place during the formation of the Great Whirl. The mechanism was identified as horizontal shear instability. Water with low potential vorticity is advected to the north, Fig. 36. The

fluid also conserves its absolute vorticity, sice vortex stretching is weak. Because of the non-zonal character of the Somali Current and the presence of the coast, classical barotropic instability theory, i.e. Kuo's (1949) nessessary condition for instability, is not valid. However, flows with an angle to the east–west direction generally are less stable than zonal flows, Gill, et al., (1974), Pedlosky (1979). The more general nessessary condition for mixed barotropic-baroclinic instability is that the potential vorticity gradient of the mean flow changes sign, (Pedlosky, 1979), i.e. that

$$\nabla_3 \Pi = 0 \qquad\qquad (3-6)$$

somewhere in the mean flow. The subscript indicates that the gradient operator is three-dimensional. A sign change in $\nabla \Pi$ along isopycnals indicates a possibility of barotropic instability, Charney and Stern, (1962), Boudra, et al., (1988). This condition is fullfilled prior to the generation of the whirl, Fig. 34, and a vertical reversal of $\nabla \Pi$ nessessary for baroclinic instability is also found. An increase in Π is found in the second layer. In case of the 1.5 layer model the generation of the Great Whirl looks very similar. The main difference is that the coastal upwelling is less intense due to the larger density difference between the upper and second layer than in the multilayer case. This causes weaker alongshore currents in that model. A high pressure situated southeast of Socotra compensates for this north of 10°N and along Socotra and produces a stronger alongshore flow there, but a weaker offshore flow is found at 6°N. This may be the reason that the generation of the eddy is delayed by about a week compared to the 3.5 layer case. The fact that the eddy formation is essentially the same in the two models and no decrease in available potential energy was observed indicates that baroclinic instability does not play a role. At the time of generation the available potential energy, $\mathcal{A}$, was increasing along the coast as well as the kinetic energy of the Somali Current, i.e.,
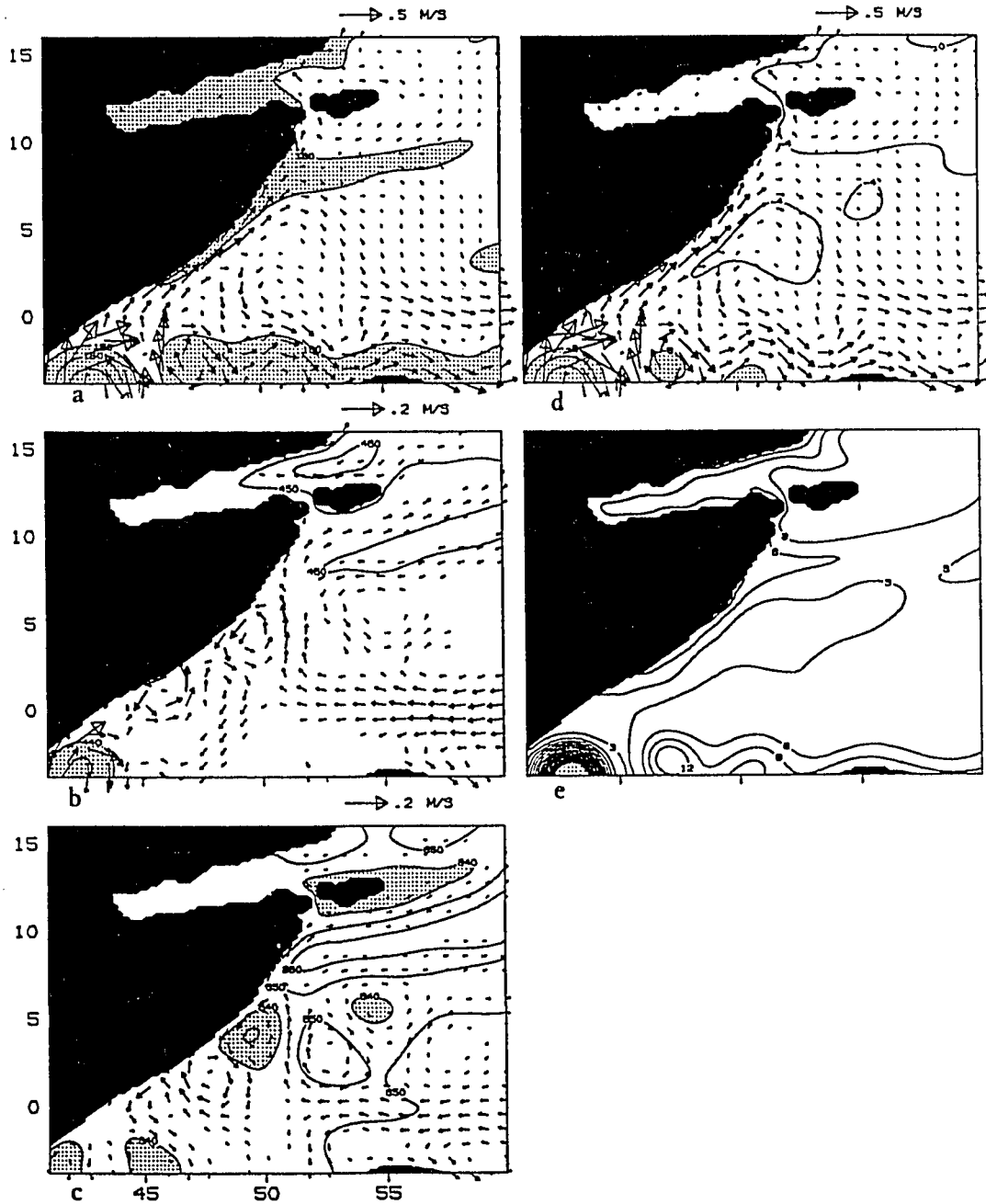
Figure 33. May 28, year 21, 3.5 layer model. Velocity and depth (m) to the bottom of layer 1, (a), layer 2, (b), layer 3, (c), velocity of upper layer and surface elevation (cm), (d). Panel (e): Available potential energy, (kJ/m²).
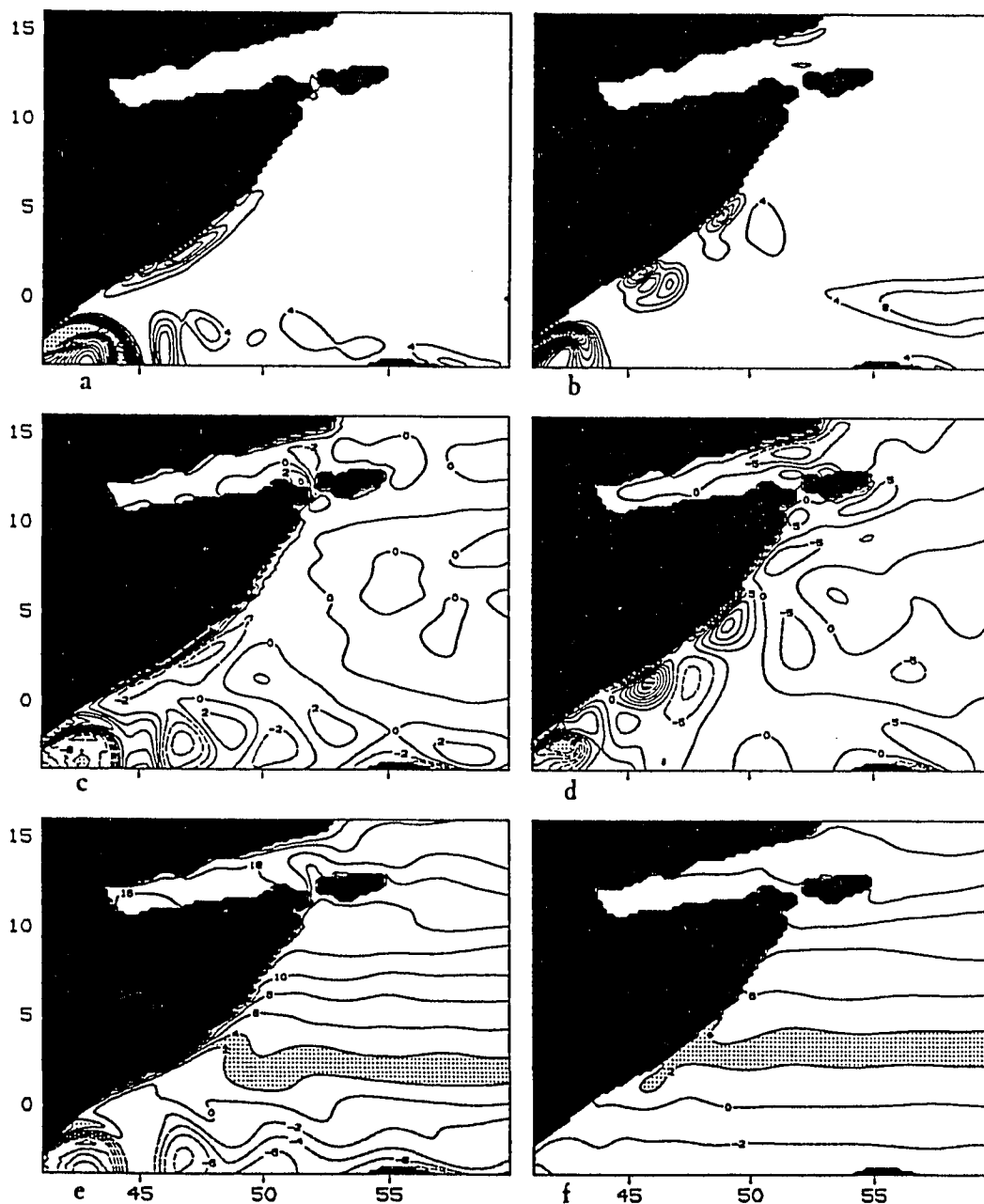
Figure 34. May 28, year 21, 3.5 layer model. Kinetic energy $(kJ/m^2$, shading: $E_{kin} > 40)$ in layer 1, (a), and layer (2), (b), (100 J/m^2, shading: $E_{kin} > 50)$. Relative vorticity in layer 1 $(10^{-6}s^{-1}$, shading: $|\zeta| > 10)$,(c), and layer 2 $(10^{-7}s^{-1}$, shading: $|\zeta| > 30)$,(d). Potential vorticity in layer 1, (e), and layer 2, (f), $(10^{-8}m^{-1}s^{-1}$, $2 \leq \Pi \leq 4$ is shaded).
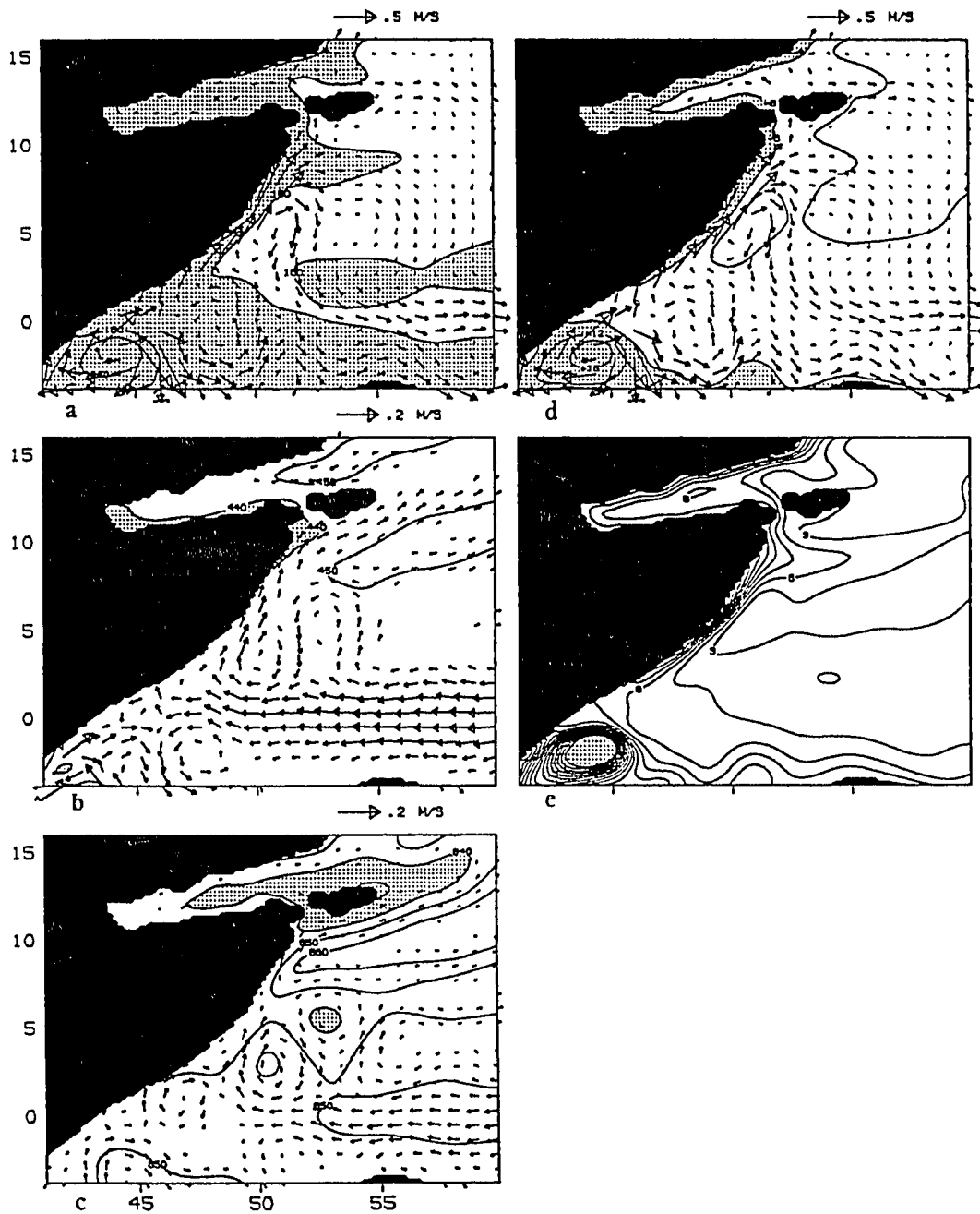
Figure 35. June 16, year 21, 3.5 layer model. Velocity and depth (m) to the bottom of layer 1, (a), layer 2, (b), layer 3, (c), velocity of upper layer and surface elevation (cm), (d). Panel (e): Available potential energy, (kJ/m^2).
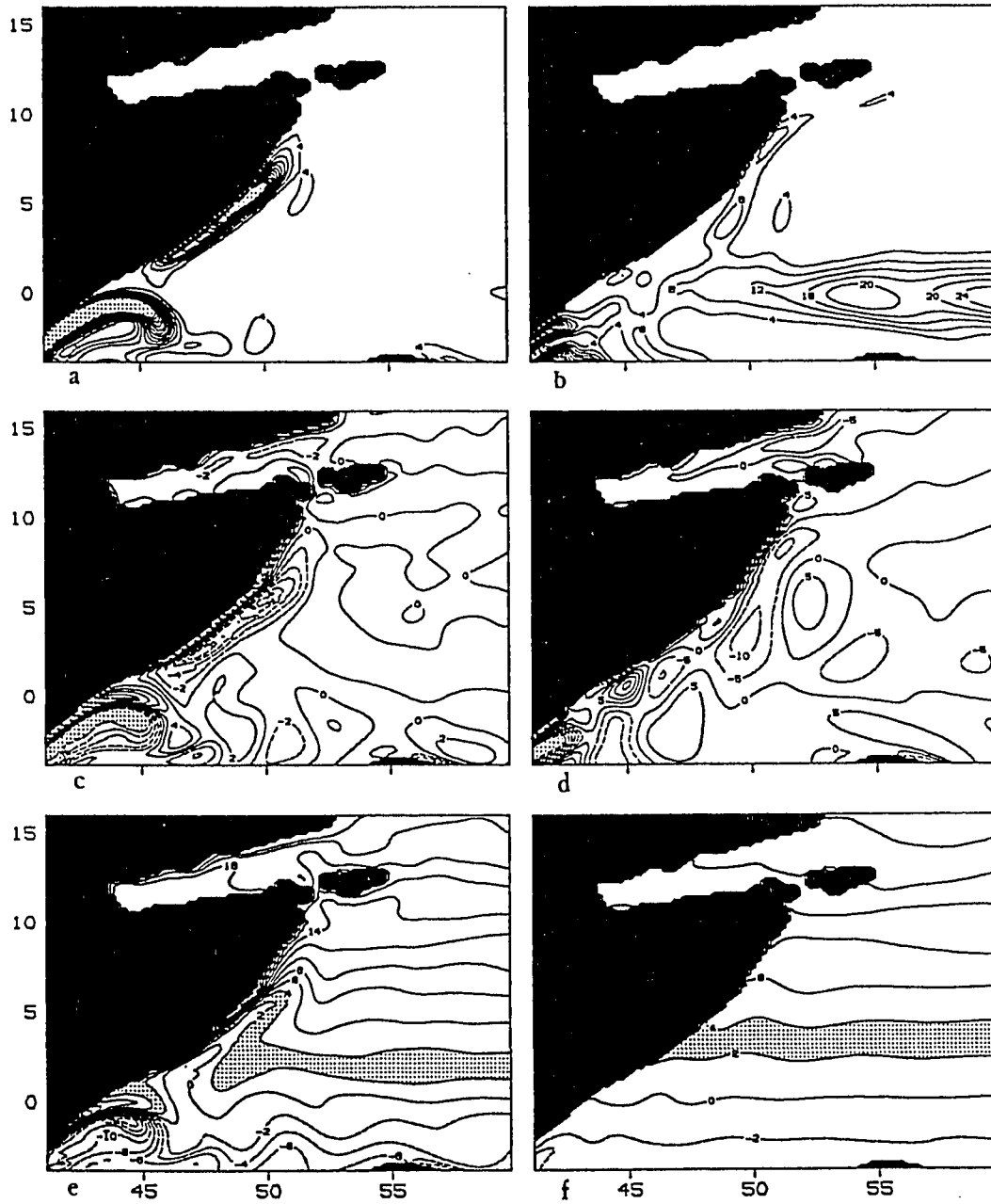
Figure 36. June 16, year 21, 3.5 layer model. Kinetic energy (kJ/m^2, shading: $E_{kin} > 40$) in layer 1, (a), and layer (2), (b), (100 J/m^2, shading: $E_{kin} > 50$). Relative vorticity in layer 1 ($10^{-6} s^{-1}$, shading: $|\zeta| > 10$),(c), and layer 2 ($10^{-7} s^{-1}$, shading: $|\zeta| > 30$),(d). Potential vorticity in layer 1, (e), and layer 2, (f), ($10^{-8} m^{-1} s^{-1}$, $2 \leq \Pi \leq 4$ is shaded).
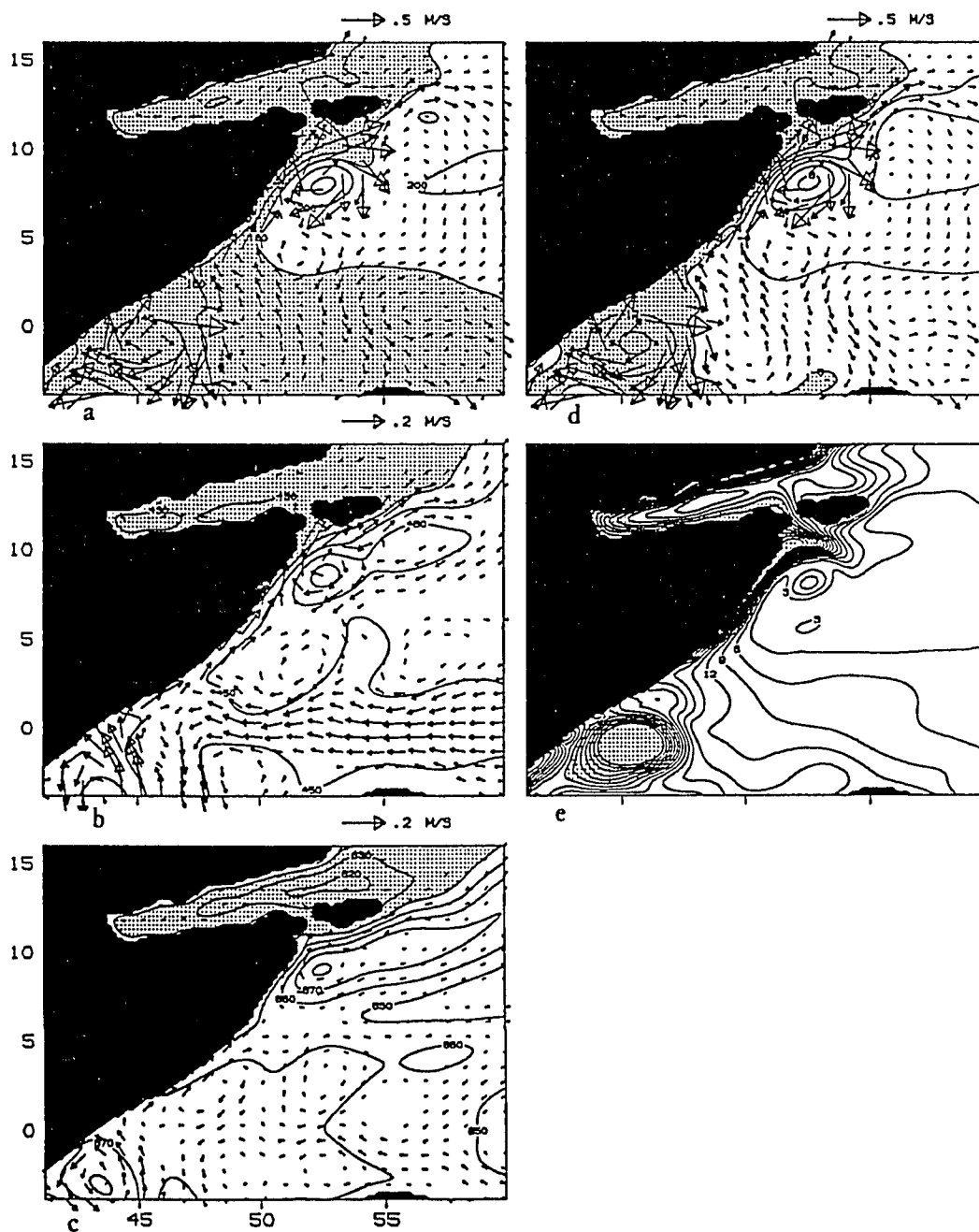
Figure 37. July 16, year 21, 3.5 layer model. Velocity and depth (m) to the bottom of layer 1, (a), layer 2, (b), layer 3, (c), velocity of upper layer and surface elevation (cm), (d). Panel (e): Available potential energy, (kJ/m²).
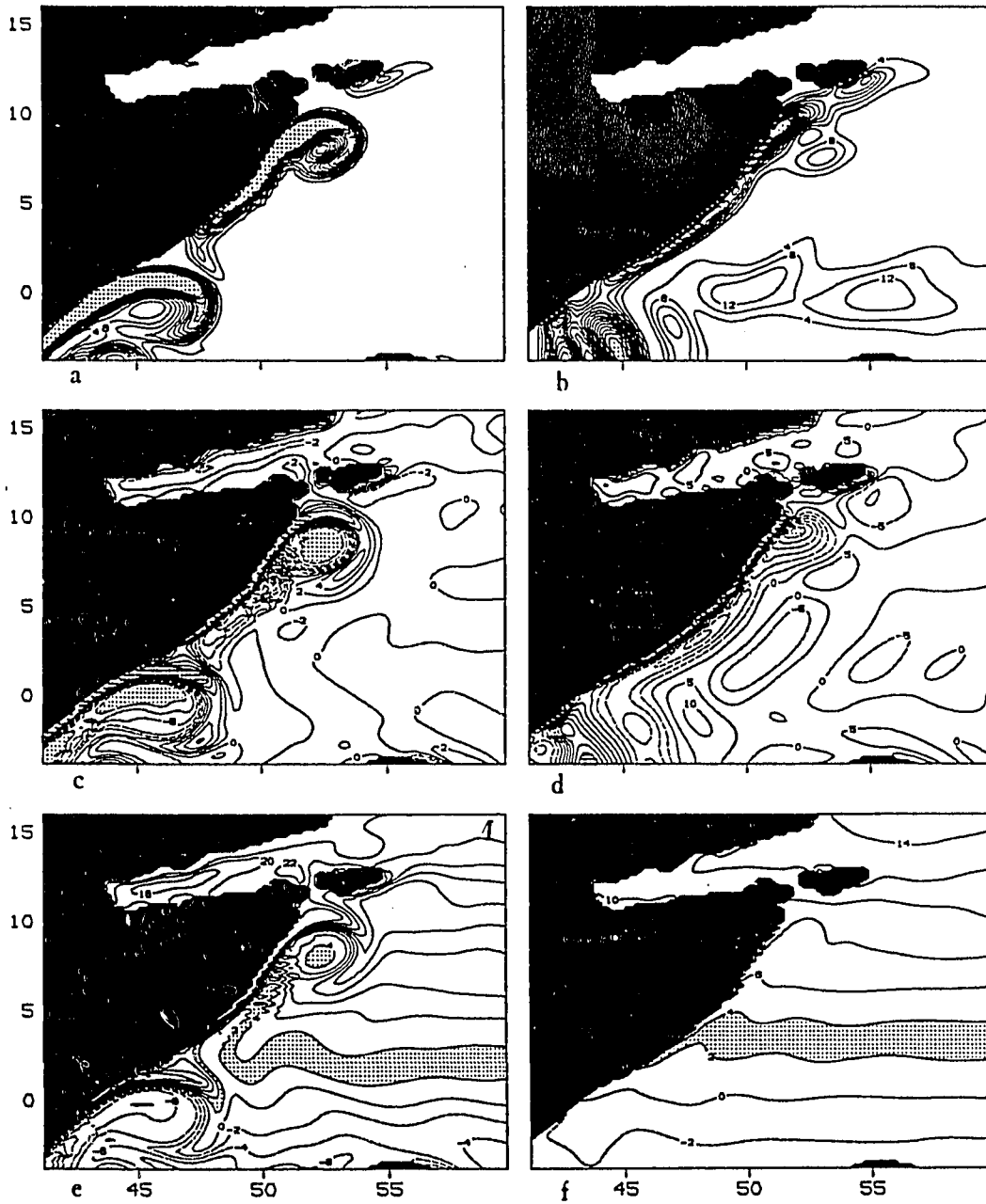
Figure 38. July 16, year 21, 3.5 layer model. Kinetic energy (kJ/m², shading: E_{kin} >40) in layer 1, (a), and layer (2), (b), (100 J/m², shading: E_{kin} >50). Relative vorticity in layer 1 ($10^{-6}s^{-1}$, shading: $|\zeta|$ >10),(c), and layer 2 ($10^{-7}s^{-1}$, shading: $|\zeta|$ >30),(d). Potential vorticity in layer 1, (e), and layer 2, (f), ($10^{-8}m^{-1}s^{-1}$, $2 \leq \Pi \leq 4$ is shaded).

the current was still in a state of acceleration. The local wind is northeastward and intensifying, with negative curl offshore, but has too large scales to be able to force the whirl directly. The eddy forms at the place along the coast where the kinetic energy in the current is maximum and the largest gradient in relative vorticity.

The Great Whirl intensifies and moves northward along the coast. It is seen in the second layer motion 12 days after the generation and after 18 days in the third layer. Since the field is only saved from the computation every six days, a more accurate estimate cannot be given. During July the northward migration and strengthening of the whirl continues, Figs. 37–38. A band of positive vorticity along the coast show the width of the frictional boundary layer. The discontinuation of the northward flow at 2°N due to offshore flow at that latitude is clearly seen at this time. Positive vorticity is advected offshore by the Great Whirl on its northern side and wraps around the "Golf club" like negative vorticity region. The numerical solution by Cox (1979) showed the same structure of the relative vorticity field. The kinetic energy fields at the same date, show that the strongest currents are found where the Somali Current turns offshore into the whirl, while currents are much weaker on the southern side in agreement with observations (see for instance Swallow, et al., 1983).

Fig. 38 (c) shows that the potential vorticity for the upper layer in the center of the Great Whirl correspond to that at 2–3°N. Some flux of positive relative vorticity can be expected from the boundary layer and by wind stress curl, but from the time when the whirl is formed in mid June to late August, the potential vorticity of its center is changed very little. This implies that the whirl is capable of carrying mass during its northward migration.

The Somali Current is stable until the beginning of August. A low of the westward propagating Rossby waves reach the eastern edge of the Great Whirl and

cyclonic motion is amplified as seen in Figs. 39–42, showing the field variables and derived quantities at August 10 and August 22. The cyclonic spinup starts in the lower layers first. The result is that a small cold eddy pinches off the wedge north of the Great Whirl, intensifying the flow along the southern edge of the whirl, in particular in the deep layers. This is the process that restores the undercurrent under the Great Whirl. The available potential energy of the whirl is essentially unchanged, while we observe a decrease in kinetic energy in the upper layer and an increase in the second layer.

The available potential energy of the Great Whirl reach its maximum at September 4, Fig. 43. The axis of the whirl is now tilting towards the northwest with depth. A new strong cyclonic eddy is generated between the whirl and Socotra. To the south of the whirl and to the north of the cyclonic eddy, weaker eddies exist. The two large eddies starts to migrate, initially southeastward. Then the cyclonic eddy moves southward to be nearly at the same latitude as the Great Whirl, i.e., a clockwise rotation of the axis through the eddy centers, and the pair moves westward. The initial movement is most likely due to mutual advection. A theoretical study of eddies by Matsuura and Yamagata (1982), showed a similar initial clockwise rotation of an eddy dipole with the cyclonic eddy to the north.

During the process the Great Whirl is losing potential energy, while kinetic energy is increased in the lower layers east of the whirl, Fig. 43-46. The low to the southeast of the whirl, due to the seasonal Rossby wave field, is amplified at the same time. The nessessary condition for baroclinic instability that the vertical gradient of potential vorticity changes sign, (Pedlosky, 1979) is satisfied in the area. This evolution suggest that the eddy pair is subject to a barotropic-baroclinic instability. Naturally, other mechanisms may play a role in the complicated flow in the area. The northeastward wind stress starts to relax in the model after mid

August although the pattern of wind stress and its curl does not start to change until after September 16. Model results, discussed below, show that this relaxation is not the major cause for change of the flow. There is an equatorial influence on the flow in the region: The deep flow south of the eddies is connected with the deep eastward equatorial undercurrent; the potential vorticity map from September 4 also show an influx of water originated south of the equator, which form a small anticyclonic eddy at 6°N. This development in the flow, with the collapse of the Great Whirl, is seen by comparing the results for September 4 and September 22. As previously noted, the Hellerman-Rosenstein wind stress results in the anomalous situation that the Southern Gyre remains in the vicinity of the equator. The formation of the small eddy which joins the Great Whirl and adds negative vorticity is the only indication of this tendency. In the two deep layers westward propagation of the eddy field causes a increased northward current through the strait between Somalia and Socotra and a negative vorticity flux from the whirl along the coast of Socotra to its northern shore.

Fig. 47-48 from October 4 shows that the subsurface part of the Great Whirl has been detached and a southwestward undercurrent now exist beneath it. The flow south of Socotra consist now of a series of eddies along a nearly zonally oriented axis, which moves westward towards the Somali coast. The whirl decays further during October, while the Socotra Warm eddy intensifies until the middle of the month, when it becomes subject to an instability process similar to that described above for the Great Whirl. The Socotra eddy moves south of the island in its westward movement, and by the end of November the anticyclonic eddies have dissappeared.

The effect of the weakening monsoon winds in August and September on this development is investigated by recomputing the solution for year 21, but

extending the length of the summer monsoon. In the first experiment, case 1, observed winds was used until August 16 and then kept constant. The wind stress pattern and it curl is nearly identical in July and August, but the magnitudes are larger in July. In this case we have a monsoon which reaches a maximum and then relaxes to be a weaker forcing. The second, case 2, kept the winds constant from July 16, so that Somali Current spins up under maximal forcing.

Both cases show an evolution of the flow very similar to the standard solution, case 0, forced by seasonal winds, until late September. The generation of deep cyclonic eddies to the southeast of the whirl takes place in the same fashion, with a decrease in available potential energy of the Great Whirl, but the intensity of the eddies is smaller than before. The explanation for this may be as follows: With the weakening of the monsoon, case 0 and case 1, the magnitude of the eastward pressure gradient and the associated deep northward flow along the coast of Somalia decreases. This allows a westward movement of the deep part of the whirl, causing the tilt towards the northwest with depth of the Great Whirl, observed prior to this event, to increase. Accordingly, the vertical shear under the whirl increases with decreasing southwest winds. Thus vertical shear instability is enhanced compared to the case where the wind continues to blow at full strength. In case 0 the cyclonic eddy generated in August moves westward and reach the Somali coast, which creates an undercurrent. In case 1 and 2 the deep flow is only slowed down, but continues to be northward. However, the second larger deep cyclonic eddy creates a coastal undercurrent in late October (case 1).

The further development in the cases with extended summer monsoon season gives an interesting result. Instead of decaying as in case 0, the Great Whirl recover its loss of energy during a clockwise rotation. By the end of October the solution looks like the standard case in early September, and a new cyclonic eddy

is generated. The instability is thus an important mechanism by which the Great Whirl is able to dissipate its excess energy.

The evolution in the 1.5 layer standard case with seasonal forcing is different than described above. When the low pressure arrives in the beginning of August, a southwestward current appears between this low and the Great Whirl, which is squeezed slightly northward as seen in Fig. 49, showing the results from August 10. No cyclonic eddy is generated to the south in this case, but the cyclonic flow in the wedge between the whirl and the Socotra eddy is weaker in this case. The Great Whirl and the cyclonic to the northeast are increasing in strength until early September, then they both start to lose potential and kinetic energy. The available potential energy decrease fastest for the Great Whirl, but at a slower rate than in the 3.5 layer case. The solution for September 16 is representative during this time, (Fig. 51). The Socotra eddy is intensified, indicating eastward energy propagation. The eddies south and east of Socotra, most clearly seen in the relative vorticity plot, move slowly westward after this time. Negative vorticity from the Great Whirl leaks northward as in the 3.5 layer case (Fig. 46), but the Socotra eddy moves to the north of the Island in this case instead of south of it as before.

78
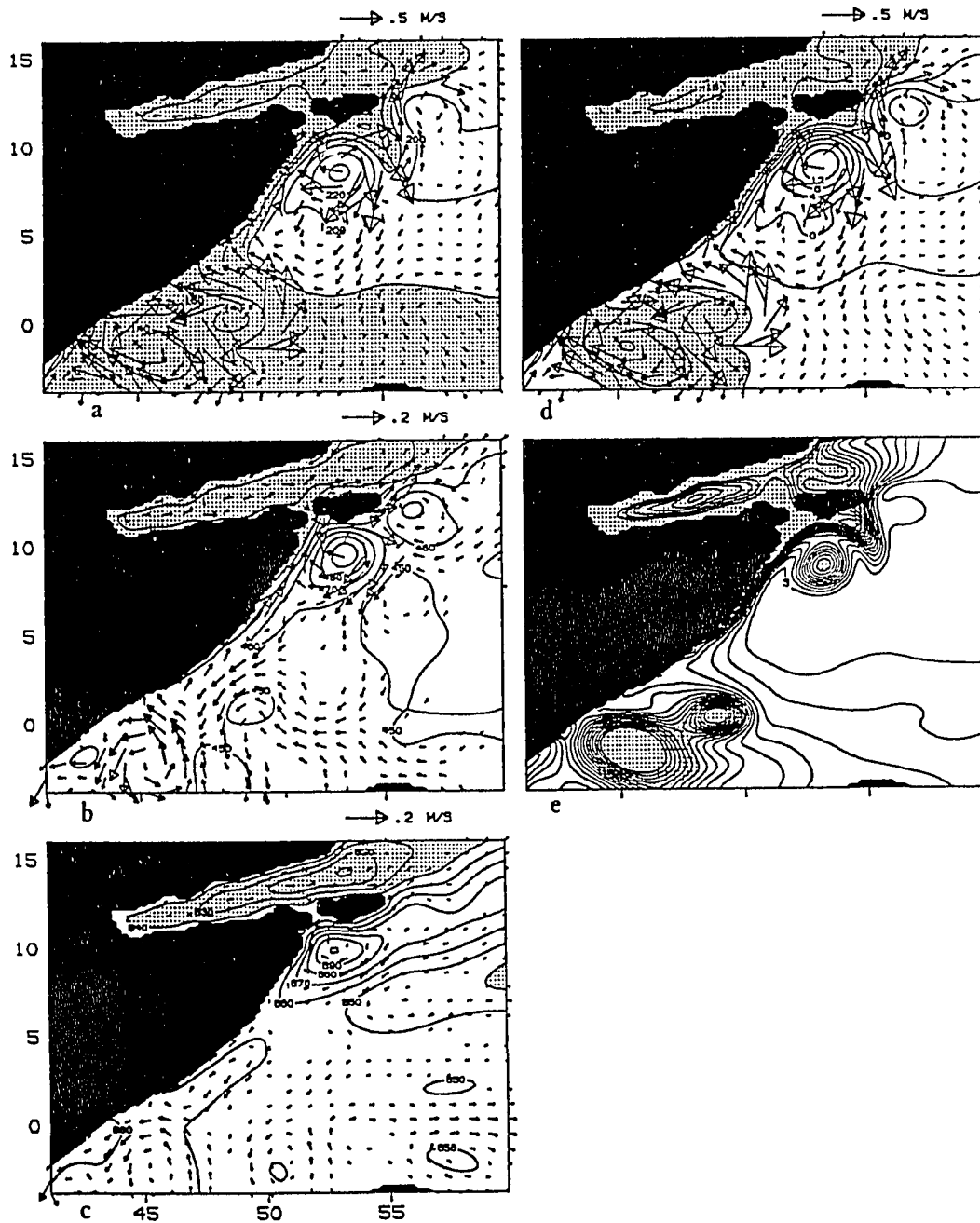
Figure 39. August 10, year 21, 3.5 layer model. Velocity and depth (m) to the bottom of layer 1, (a), layer 2, (b), layer 3, (c), velocity of upper layer and surface elevation (cm), (d). Panel (e): Available potential energy, (kJ/m²).
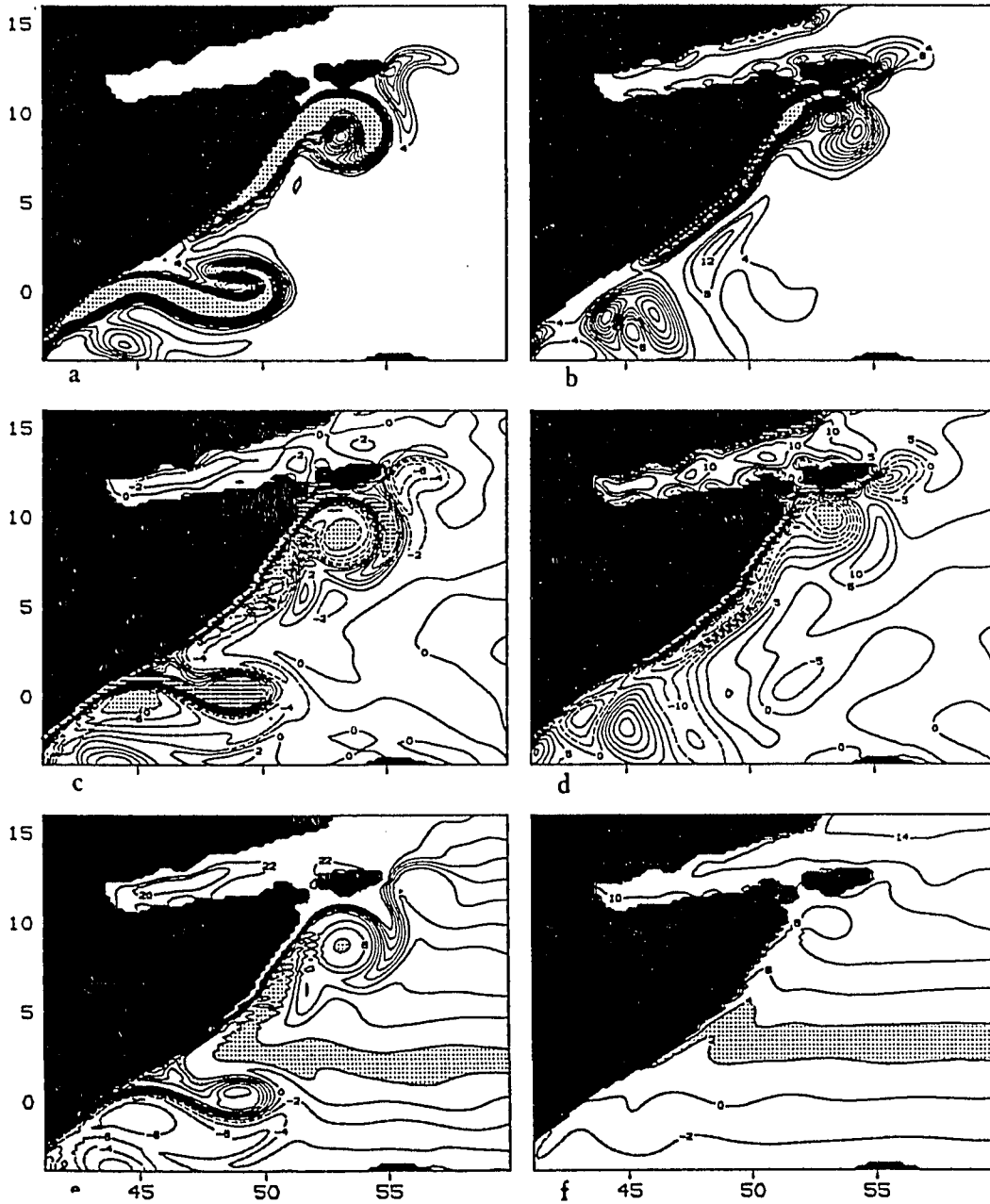
Figure 40. August 10, year 21, 3.5 layer model. Kinetic energy (kJ/m^2, shading: $E_{kin} > 40$) in layer 1, (a), and layer (2), (b), (100 J/m^2, shading: $E_{kin} > 50$). Relative vorticity in layer 1 ($10^{-6}s^{-1}$, shading: $|\zeta| > 10$),(c), and layer 2 ($10^{-7}s^{-1}$, shading: $|\zeta| > 30$),(d). Potential vorticity in layer 1, (e), and layer 2, (f), ($10^{-8}m^{-1}s^{-1}$, $2 \leq \Pi \leq 4$ is shaded).

80
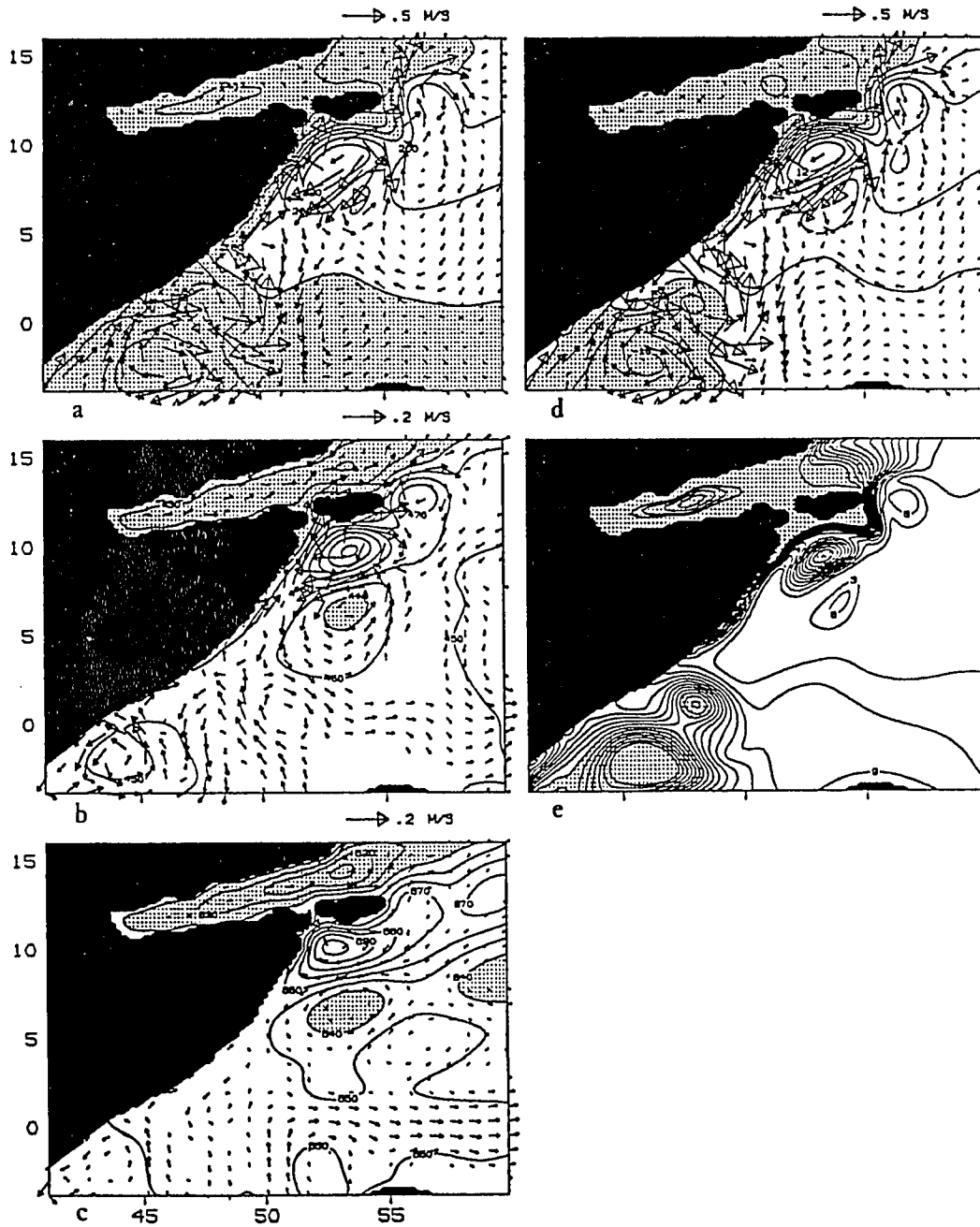
Figure 41. August 22, year 21, 3.5 layer model. Velocity and depth (m) to the bottom of layer 1, (a), layer 2, (b), layer 3, (c), velocity of upper layer and surface elevation (cm), (d). Panel (e): Available potential energy, (kJ/m²).
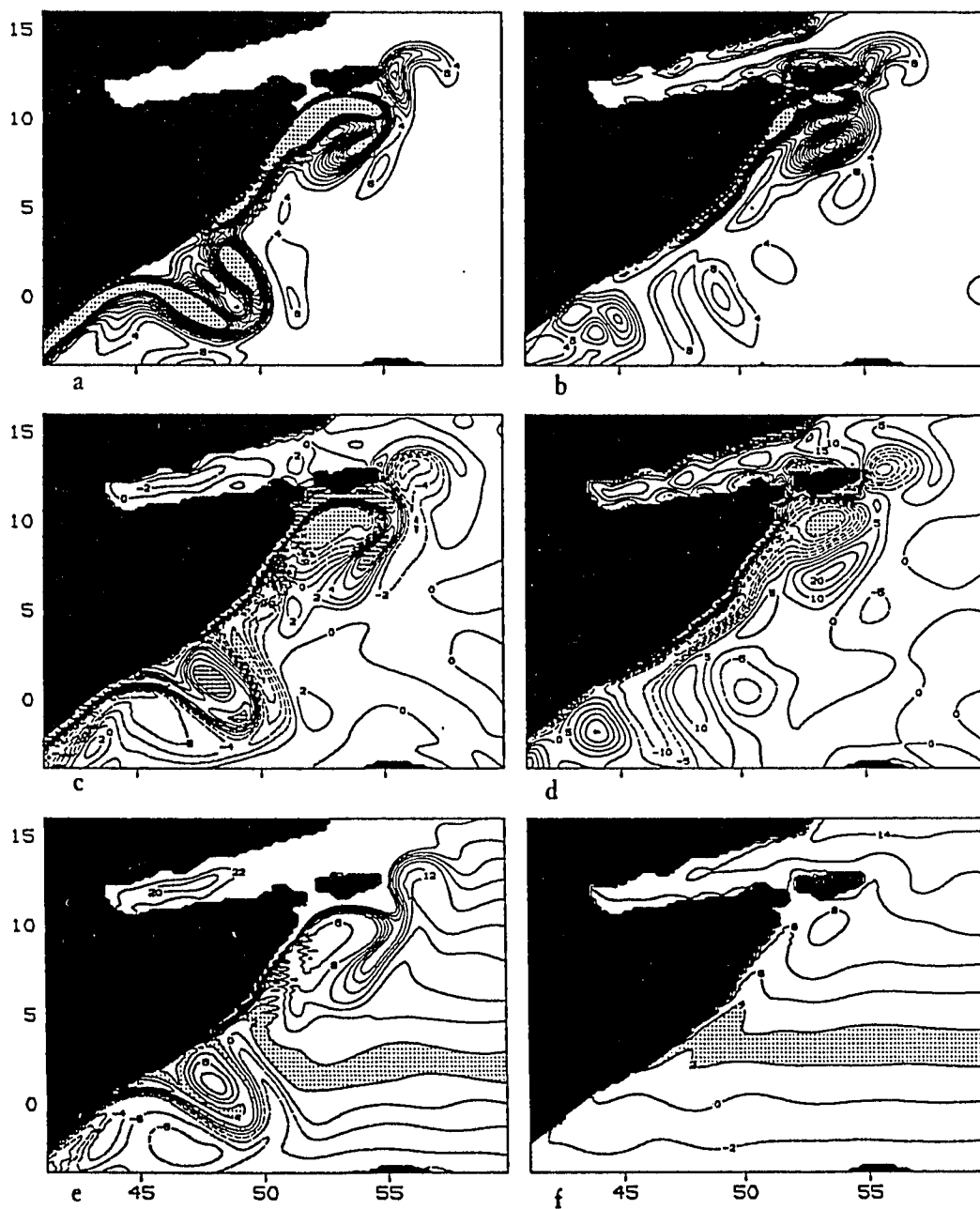
Figure 42. August 22, year 21, 3.5 layer model. Kinetic energy (kJ/m², shading: E_{kin} >40) in layer 1, (a), and layer (2), (b), (100 J/m², shading: E_{kin} >50). Relative vorticity in layer 1 ($10^{-6}s^{-1}$, shading: $|\zeta|$ >10),(c), and layer 2 ($10^{-7}s^{-1}$, shading: $|\zeta|$ >30),(d). Potential vorticity in layer 1, (e),and layer 2, (f), ($10^{-8}m^{-1}s^{-1}$, $2 \leq \Pi \leq 4$ is shaded).
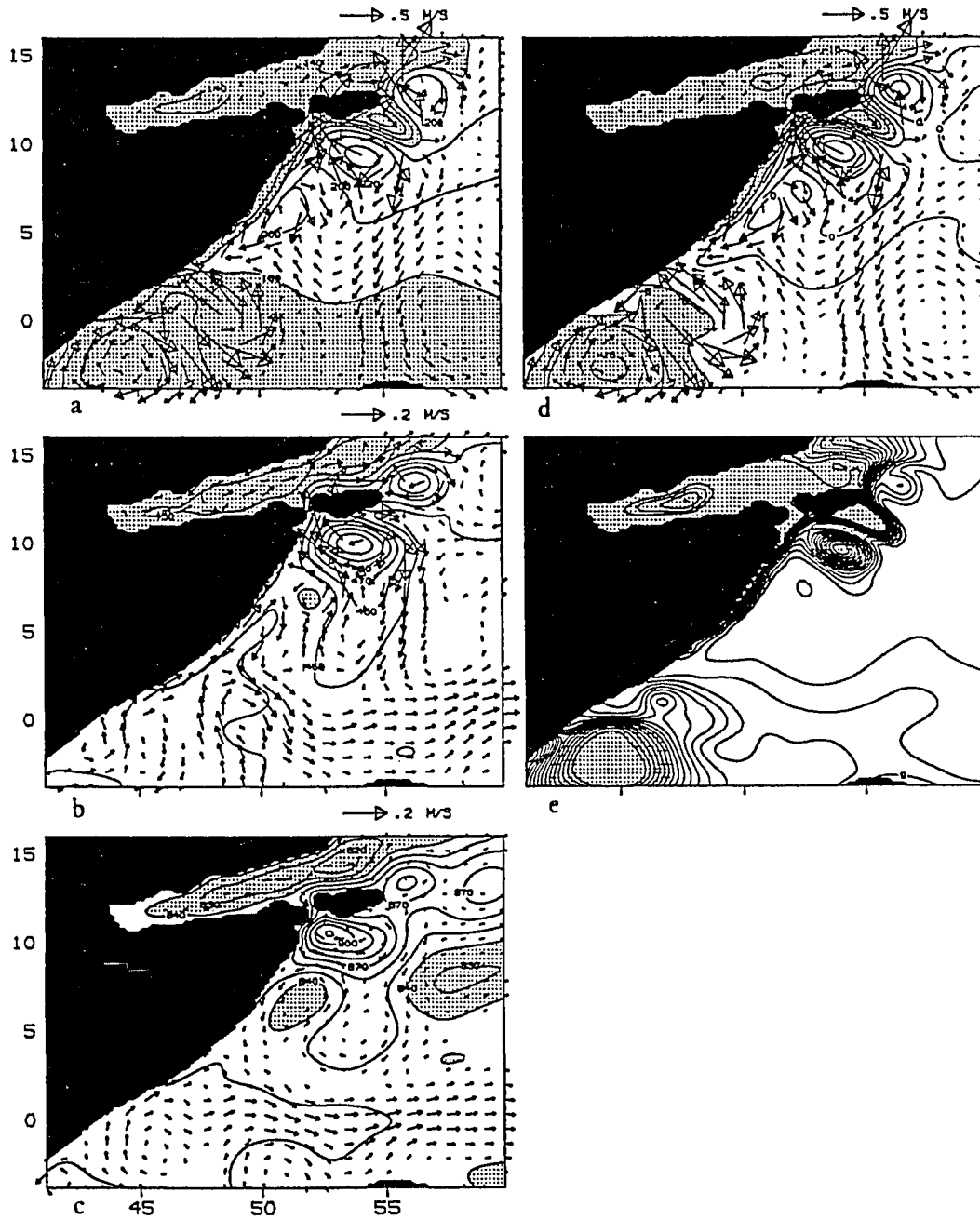
Figure 43. September 4, year 21, 3.5 layer model. Velocity and depth (m) to the bottom of layer 1, (a), layer 2, (b), layer 3, (c), velocity of upper layer and surface elevation (cm), (d). Panel (e): Available potential energy, (kJ/m².)

83
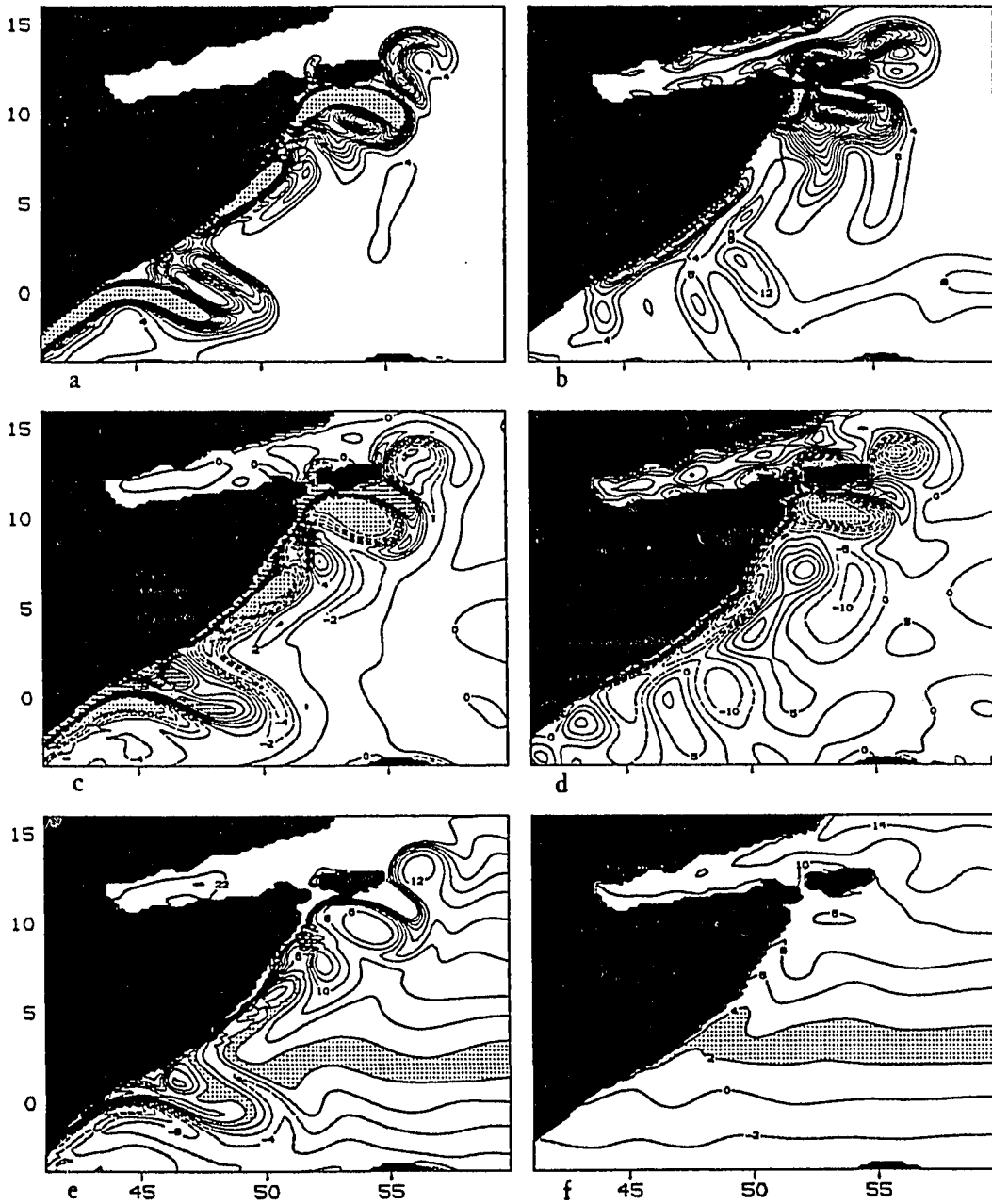
Figure 44. September 4, year 21, 3.5 layer model. Kinetic energy $(kJ/m^2$, shading: $E_{kin} >40)$ in layer 1, (a), and layer (2), (b), (100 J/m^2, shading: $E_{kin} >50)$. Relative vorticity in layer 1 $(10^{-6}s^{-1}$, shading: $|\zeta| >10)$,(c), and layer 2 $(10^{-7}s^{-1}$, shading: $|\zeta| >30)$,(d). Potential vorticity in layer 1, (e), and layer 2, (f), $(10^{-8}m^{-1}s^{-1}$, $2 \leq \Pi \leq 4$ is shaded).
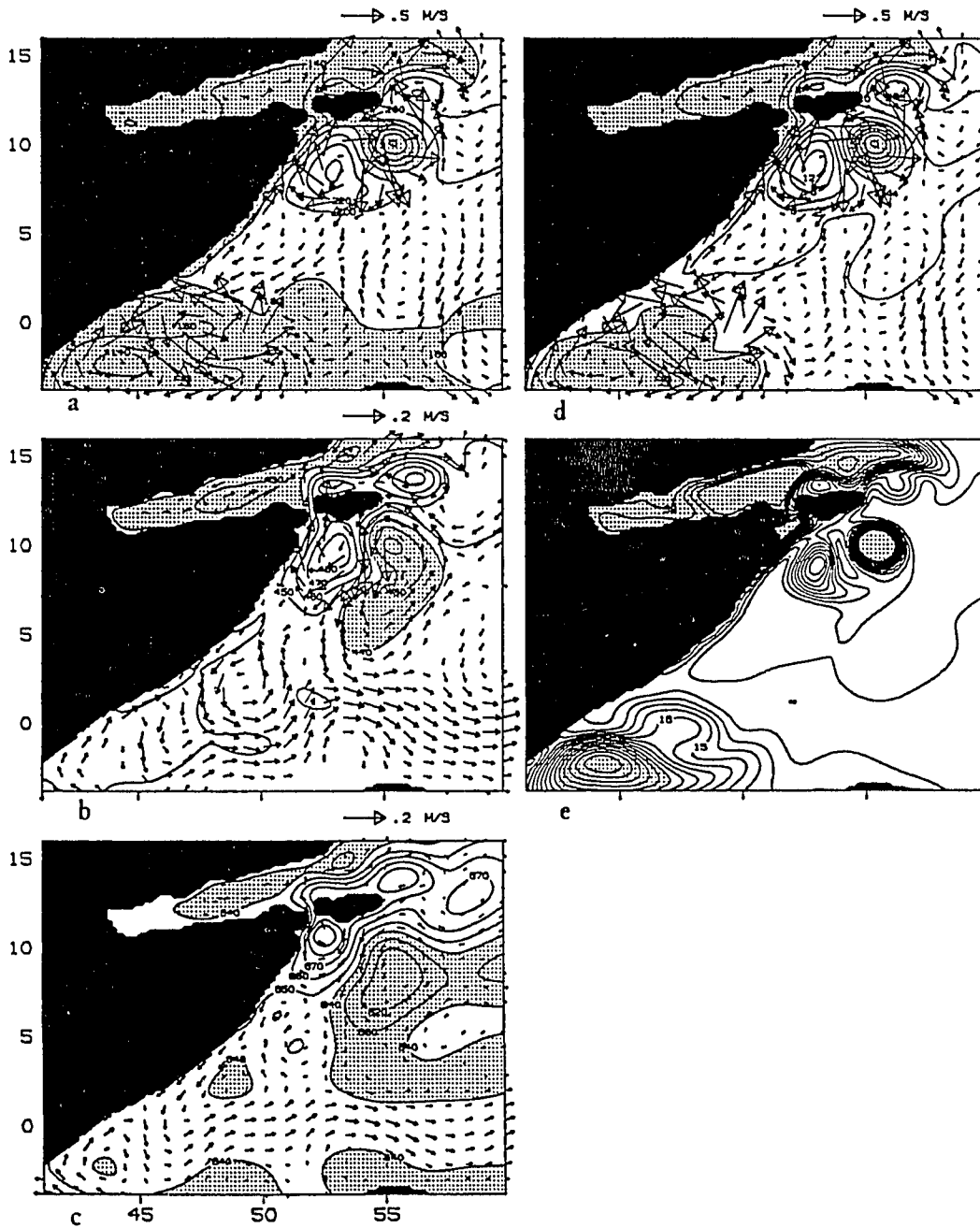
Figure 45. September 22, year 21, 3.5 layer model. Velocity and depth (m) to the bottom of layer 1, (a), layer 2, (b), layer 3, (c), velocity of upper layer and surface elevation (cm), (d). Panel (e): Available potential energy, (kJ/m²).
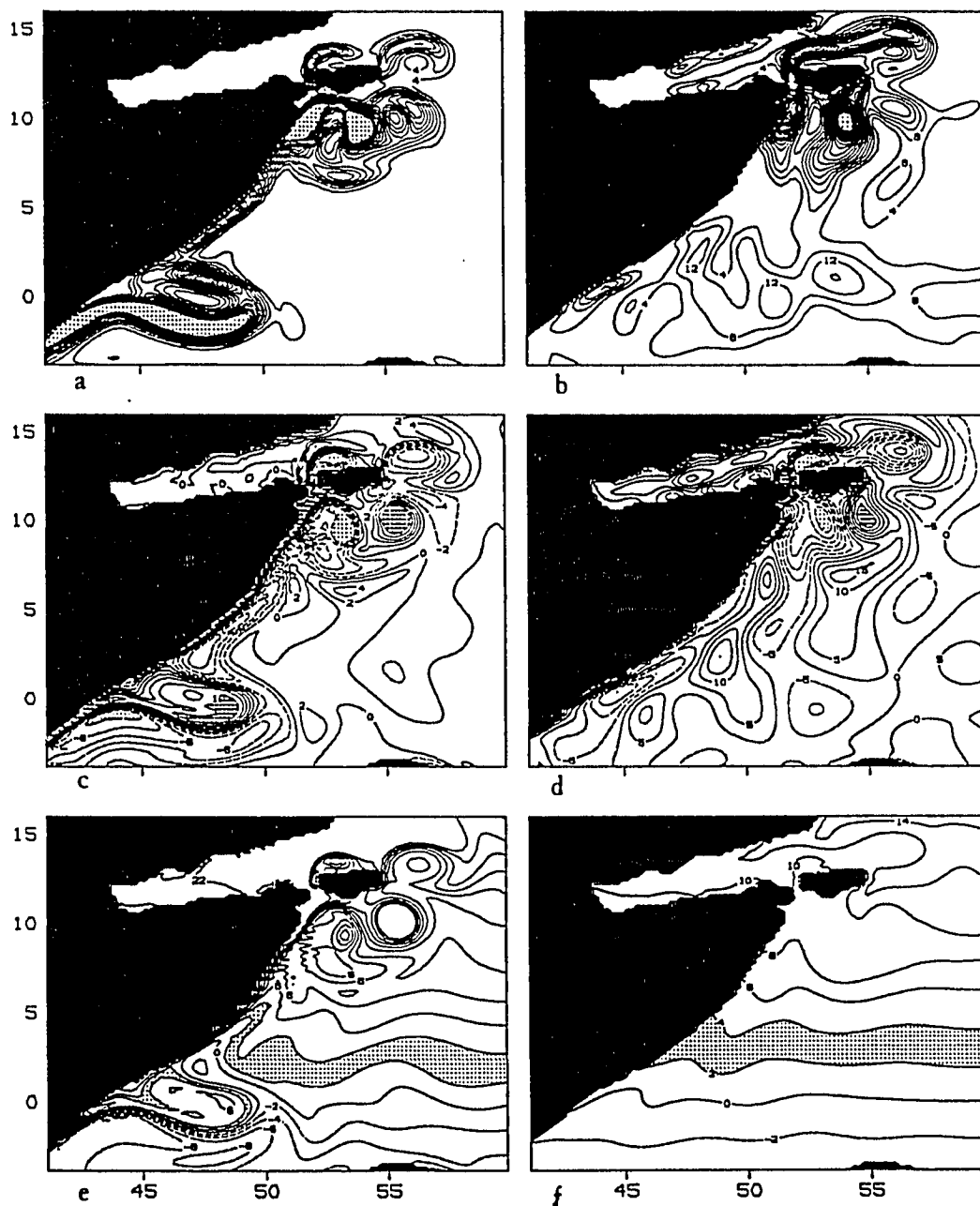
Figure 46. September 22, year 21, 3.5 layer model. Kinetic energy (kJ/m^2, shading: $E_{kin} > 40$) in layer 1, (a), and layer (2), (b), (100 J/m^2, shading: $E_{kin} > 50$). Relative vorticity in layer 1 ($10^{-6}s^{-1}$, shading: $|\zeta| > 10$),(c), and layer 2 ($10^{-7}s^{-1}$, shading: $|\zeta| > 30$),(d). Potential vorticity in layer 1, (e), and layer 2, (f), ($10^{-8}m^{-1}s^{-1}$, $2 \leq \Pi \leq 4$ is shaded).
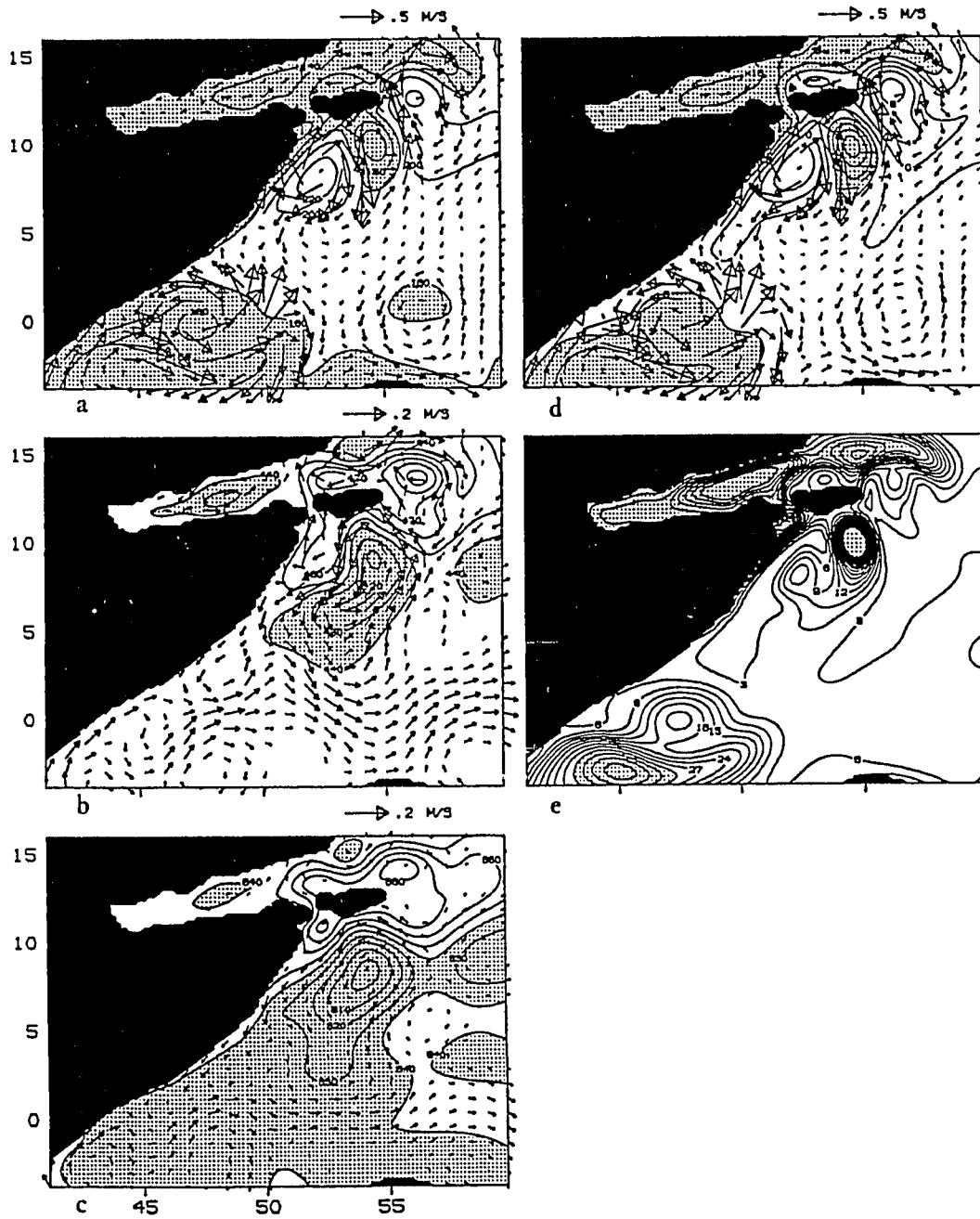
Figure 47. October 4, year 21, 3.5 layer model. Velocity and depth (m) to the bottom of layer 1, (a), layer 2, (b), layer 3, (c), velocity of upper layer and surface elevation (cm), (d). Panel (e): Available potential energy, (kJ/m²).
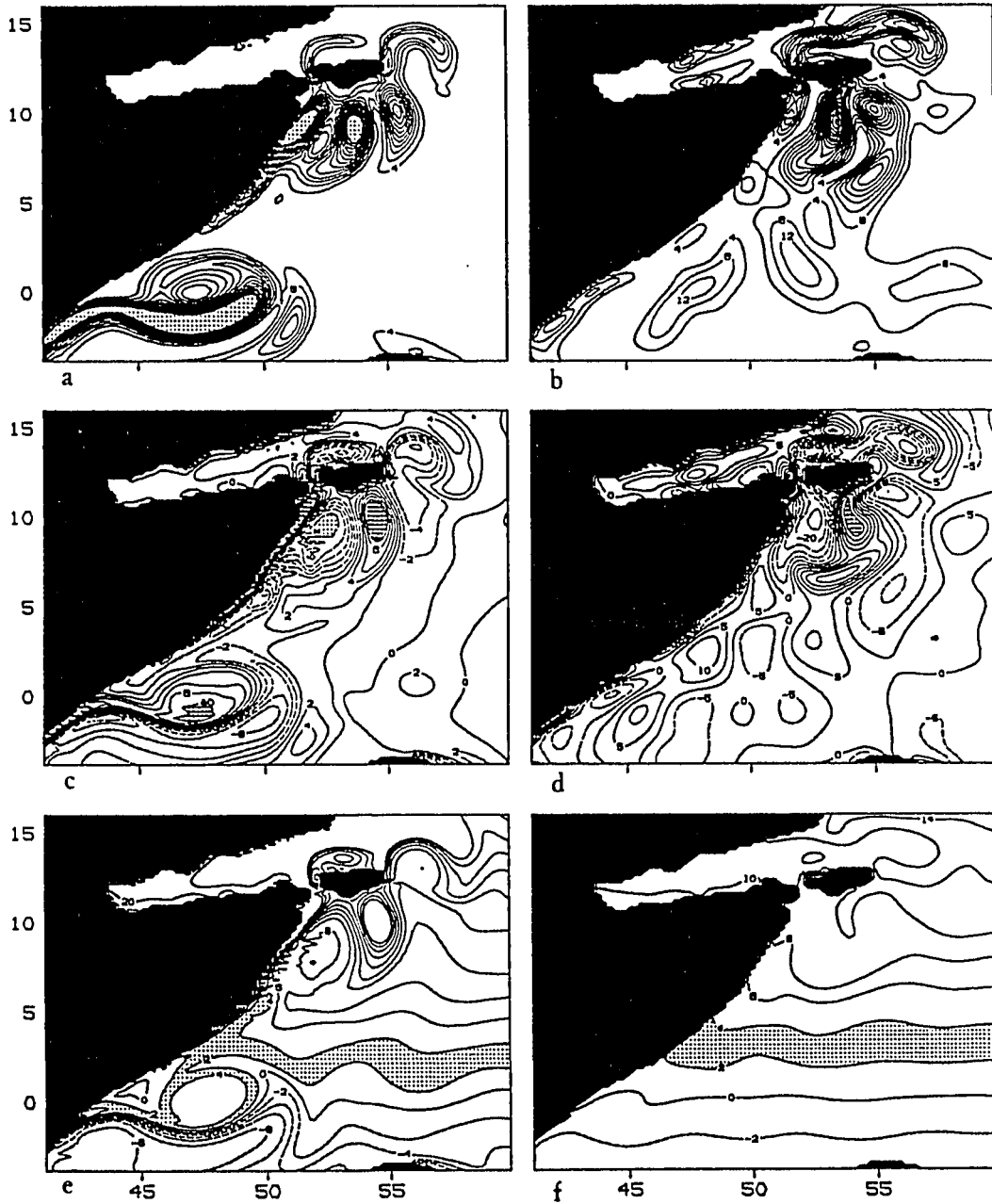
Figure 48. October 4, year 21, 3.5 layer model. Kinetic energy (kJ/m^2, shading: $E_{kin} > 40$) in layer 1, (a), and layer (2), (b), ($100\ J/m^2$, shading: $E_{kin} > 50$). Relative vorticity in layer 1 ($10^{-6}s^{-1}$, shading: $|\zeta| > 10$),(c), and layer 2 ($10^{-7}s^{-1}$, shading: $|\zeta| > 30$),(d). Potential vorticity in layer 1, (e), and layer 2, (f), ($10^{-8}m^{-1}s^{-1}$, $2 \leq \Pi \leq 4$ is shaded).
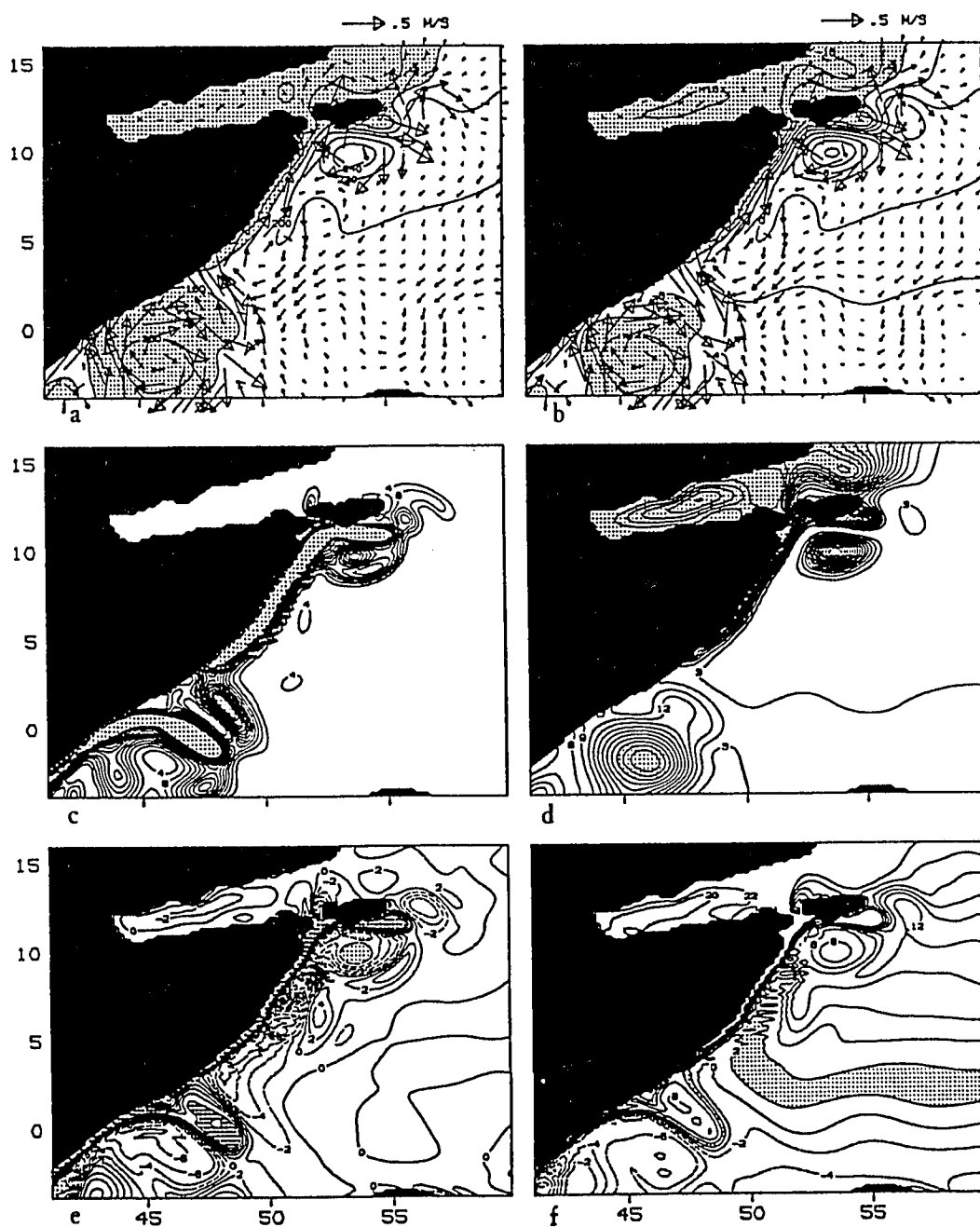
Figure 49. August 10, year 21, 1.5 layer model. Velocity and depth (m) to the bottom of active layer, (a) and surface elevation, (b). Kinetic energy $(kJ/m^2$, shading: $E_{kin} >40)$, (c). Available potential energy, (kJ/m^2), (d). Relative vorticity $(10^{-6}s^{-1}$, shading: $|\zeta| >10),(e)$. Potential vorticity, (f), $(10^{-8}m^{-1}s^{-1}, 2 \leq \Pi \leq 4)$ is shaded.
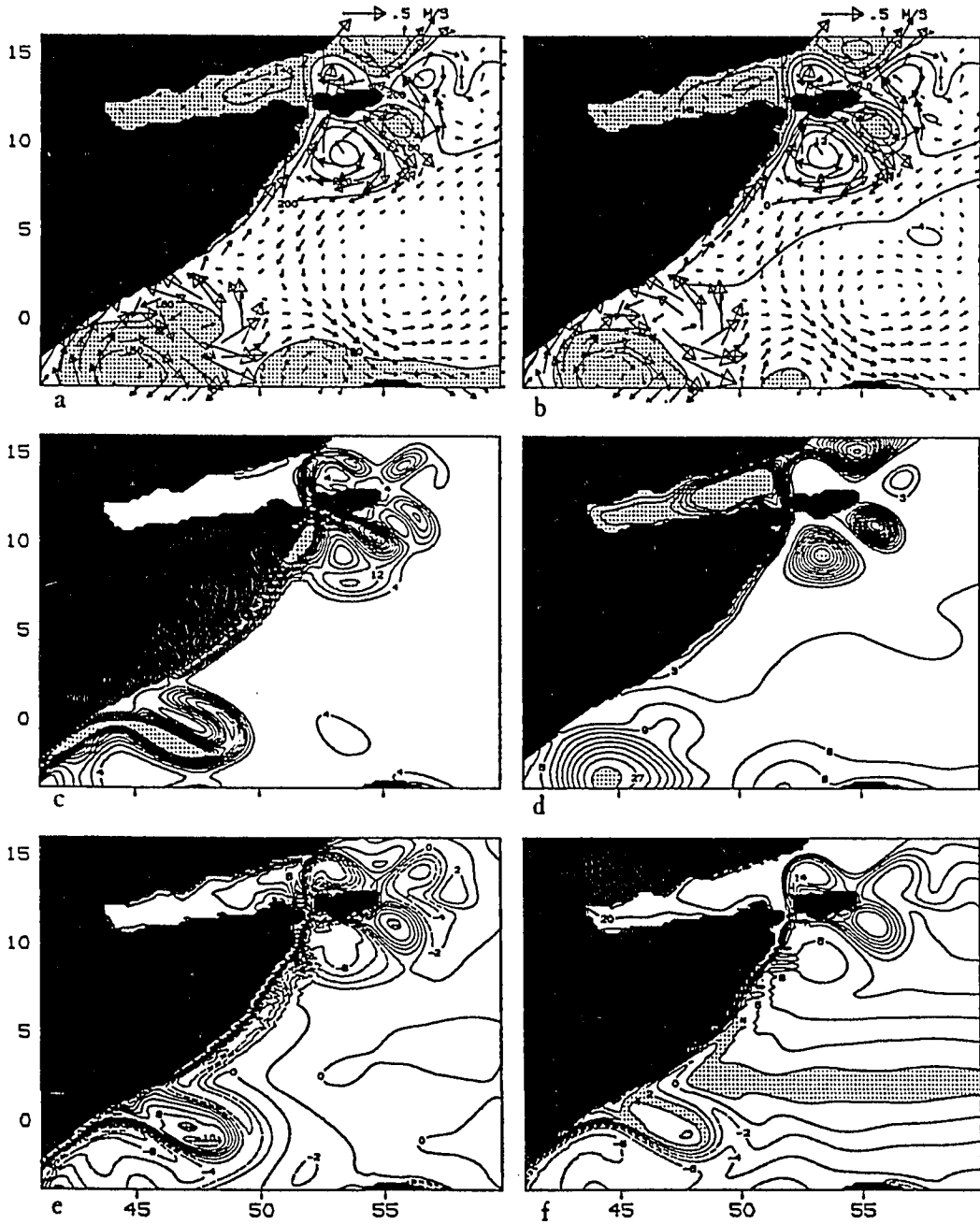
Figure 50. September 22, year 21, 1.5 layer model. Velocity and depth (m) to the bottom of active layer, (a) and surface elevation, (b). Kinetic energy (kJ/m², shading: $E_{kin} > 40$), (c). Available potential energy, (kJ/m²), (d). Relative vorticity ($10^{-6}s^{-1}$, shading: $|\zeta| > 10$),(e). Potential vorticity, (f), ($10^{-8}m^{-1}s^{-1}$, $2 \leq \Pi \leq 4$ is shaded).

4. SUMMARY

In the introduction the present observational knowledge and various modelling efforts in the past was reviewed. Major oceanographic field programs in the sixties and late seventies have increased our knowledge about the equatorial and northwestern Indian Ocean, in particular the Somali Current system. While the near-surface flow is well documented during the summer monsoon, observations are sparse during the northern winter and below the thermocline. However, the available data show that the deeper flow is quite energetic and consist of eddies with small horizontal scale near the Somali Coast (e.g., Leetmaa, et al., 1980, Quadfasel and Schott, 1982.).

Previous models have fallen into one of two categories. The first type is that of process models with simple geometries and forcing, which explain the physics involved in certain problems. An example is the generation of the Somali Current system by local wind, (Hurlburt and Thompson, 1976, Lin and Hurlburt, 1981). The second type is models, which simulate the circulation with realistic geometries and forcing. Examples are the models by Cox (1970), Luther and O'Brien, (1985, 1989) and Woodberry, et al., (1989). The first of these studies had inadequate horizontal resolution to resolve eddies, while the latter authors had only one active layer. The present study falls in the second category and is the the first Indian Ocean isopycnal model to be eddy resolving with vertical structure.

The objectives of this study are: 1. Verify that the model reproduces the observed features of the Indian Ocean circulation and in the Somali Current system.

90

2. Use the model results to explain the observed undercurrent structure. 3. Find a possible explanation for the decay of the Great Whirl.

Section 2 presents the new general multi-layer model. It is formulated in spherical coordinates with few approximations. To prevent ventilation of the upper layer, its initial thickness has been chosen as 200 m, and an entrainment scheme was added, (McCreary and Kundu, 1988). A reduced-gravity formulation in which the pressure gradient vanish in the lowest layer filters out the external modes. The computer implementation allows any number of active layers to be specified within memory limitations.

The model geometry is realistic with open boundaries in the east and the south. The forcing is the climatological seasonal wind stress. The initial condition and the open boundary conditions are determined using normal vertical modes. The formulation of the open boundary conditions for multi-layer models, based on Camerlengo and O'Brien, (1980), is new. The fine horizontal resolution ensures that the internal radius of deformation for the three baroclinic modes in the model are resolved.

In section 3 the results from numerical simulations with one and three active layers are presented. The general circulation in the upper layer is essentially the same as found by 1.5 layer models (Woodberry, et al., 1989) and is in good agreement with observations. The semi-annual reversals of the undercurrents observed by Luyten and Roemmich, (1982), at intermediate depths are reproduced. In agreement with their observations, the phase propagation is westward and upward. Generation of planetary waves along eastern land boundaries are important for the interior time-dependent flow and the solution near the western boundary. Here the long planetary waves reflect by decreasing their wave length and eddies and meanders are generated through nonlinearities. Compared to 1.5 layer models,

e.g., Luther and O'Brien, (1989), we find an increased variability when the lower layers are active.

At the equator and along the Somali Coast the most energetic eddies are found. Yanai waves are responsible for eastward propagation of energy along the equator in the late summer and during the northeast monsoon. The model produces a reversing Somali Current with southward flow during the northeast Monsoon and northward flow during the northeast monsoon. The eddies associated with the latter, The Southern Gyre, the Great Whirl and the Socotra eddy are all reproduced in the solution. The northward migration of the southern gyre in the final phase of the Monsoon is absent with the wind forcing used here.

Considering the low vertical resolution in the model, the observed seasonal behaviour of the undercurrents in the Somali Current system is remarkably well reproduced. Linear theories, e.g. Ligthill, (1969), McCreary and Kundu, (1985), show that the first few vertical modes dominate the oceanic response to the wind, so this result could be anticipated. The vertical structure observed along the Somali coast is also dominated by the lowest modes, see for instance Leetmaa *et al.*, (1982), while higher modes also play a role in the equatorial flow (Luyten and Swallow, 1976).

The disappearence of the Somali coastal undercurrent in the spring is found to be caused in part by the arrival of the deep equatorial undercurrents due to semi-annual zonal wind forcing. The regeneration of the undercurrent in the fall, which agrees with the observations, is associated with the decay of the Great Whirl in our model solution. In addition to these new results, the model solution shows a complicated pattern of eddies between the equator and the southern Arabian Coast in the deeper layers where observations are sparse. Since there is no thermodynamic forcing, our model results suggest these undercurrents to be mainly wind-driven.

93

The generation and decay of the Great Whirl is described in detail for year 21 of the model solution. During the initial phase of the summer monsoon the numerical solution show the characteristics of an analytical linear vertical mode solution of McCreary and Kundu, (1985). It is demonstrated that horizontal shear instability is the most likely mechanism involved in its formation. This corroborates earlier findings, e.g., Cox (1979). Maps of potential vorticity, relative vorticity, kinetic energy and available potential energy are presented to help understanding the dynamics in the region.

Many physical processes are involved during the decay of the Great Whirl. The generation of a cyclonic eddy between the whirl and Socotra is followed by southeastward mutual advection of the eddies. A rapid decrease in available potential energy of the Great Whirl and an increase of cyclonic kinetic energy in the lower layers, suggest that baroclinic instability is partly responsible for the decay in the 3.5 layer case.

Two experiments where the duration of the summer monsoon was extended by keeping the wind stress constant after July 16 and August 16, respectively, showed a similar solution. This demonstrates that the formation of the cyclonic eddies are not caused by wind forcing, but is due to redistribution of energy in the flow itself.

With a single layer, vertical energy exchange is impossible, and the transition to the winter monsoon is therefore different. Here energy is transfered from the Great Whirl eastward to the Socotra eddy. As a result of the changed decay mechanism this case is different from the 3.5 layer solution during the following winter monsoon.

5. DISCUSSION AND CONCLUSIONS

Many authors have been successful in modelling some aspects of the response of the Somali Current to the summer monsoon, but no model has been presented to date that is capable of reproducing the observed features of the undercurrents. It is clear from earlier studies that realistic coastlines and winds are nessessary to obtain the observed configuration in numerical models, e.g., Knox and Anderson, (1985). Because of the small horizontal scales along the western boundary, the internal radius of deformation must also be resolved. These requirements made it nessessary for us to use the latest supercomputer technology and a very efficient code.

The fine horizontal resolution enables our model to reproduce more of the detailed structure in the Somali Current system than in earlier studies. The solution includes the coastal upwelling in the spring and generation of the Great Whirl at the correct latitude with following northward migration. This has previously been modelled for the upper layer using reduced-gravity models with fine horizontal resolution, but our model simulates in addition the seasonal variability of the undercurrents in very good agreement with the sparse observations. The results are surprisingly good in spite of the very limited vertical resolution, lack of bottom topography and thermodynamic forcing.

The most important physical process in this model compared to single-layer simulations is the vertical transfer of energy, which allows baroclinic instability. During the transition from summer to winter monsoon the results from the model

suggest that several mechanisms play a role in the decay of the Great Whirl. These are migration through eddy-eddy interaction, eddy-wave interaction and downward energy propagation, indicating that baroclinic instability is an important part.

Compared to large ocean general-circulation models, the advantage of our simple model is that it requires relatively modest computer resources. This allows experiments with additional physics, for instance inclusion of a mixed layer or interfacial friction between layers, or simulations with other wind fields or geometries.

REFERENCES

Anderson, D. L. T. and D. W. Moore, 1979: Cross-equatorial jets with special relevance to very remote forcing of the Somali Current. *Deep Sea Res.*, **26**, 1–22.

Anderson, D. L. T. and P. B. Rowlands, 1976: The Somali Current response to the monsoon: The relative importance of local and remote forcing. *J. Mar. Res.*, **34**, 395–417.

Arakawa, A. and Lamb, V. R., 1977: Computational design of the basic dynamical processes of the UCLA general circulation model. In: *Methods in Computational Physics*, Vol. 17, Academic Press, 174–265.

Bleck, R. and D. B. Boudra, 1981: Initial testing of a numerical ocean circulation model using a hybrid (quasi-isopycnic) vertical coordinate. *J. Phys. Oceanogr.*, **11**, 755–770.

Bleck, R. and D. B. Boudra, 1986: Wind-driven spin-up in eddy-resolving ocean models formulated in isopycnic and isobaric coordinates. *J. Geophys. Res.*, **91**, 7611–7622.

Boudra, D. B., R. Bleck and F. Schott, 1988: A numerical model of instabilities in the Florida Current. *J. Mar. Res.*, **46**, 715–751.

Boudra, D. B. and W. P. M. de Ruijter, 1986: The wind-driven circulation of the South Atlantic-Indian Ocean – II. Experiments using a multi-layer numerical model. *Deep-Sea Res.*, **33**, 447–482.

Bruce, J. G., 1973: Large scale variations of the Somali Current during the southwest monsoon. *Deep Sea Res.*, **20**, 837–846.

Bruce, J. G., 1979: Eddies off the Somali coast during the southwest monsoon. *J. Geophys. Res.*, **84**, 7742–7748.

Bruce, J. G. and G. H. Volkmann, 1969: Some measurements of current off the Somali coast during the northeast monsoon. *J. Geophys. Res.*, **74**, 1958–1967.

Bryan, K., 1969: A numerical method for the study of the circulation of the world ocean. *J. Comput. Phys.*, **4**, 347–376.

Busalacchi, A. J. and J. J. O'Brien, 1980: The seasonal variability in a model of the Tropical Pacific. *J. Phys. Oceanogr.*, **10**, 1929–1951.

Camerlengo, A. L. and J. J. O'Brien, 1980: Open boundary conditions in rotating fluids. *J. Comput. Phys.*, **35**, 12–35.

Charney, J. G. and M. E. Stern, 1962: On the stability of internal baroclinic jets in a rotating atmosphere. *J. Atmos. Sci.*, **19**, 159–172.

Cho, H. R. and T. L. Clark, 1981: A numerical investigation of the structure of vorticity fields associated with a deep convective cloud. *Mon. Wea. Rev.*, **109**, 1654–1670.

Cox, M. D., 1970: A mathematical model of the Indian Ocean. *Deep-Sea Res.*, **17**, 47–75.

Cox, M. D., 1976: Equatorially trapped waves and the generation of the Somali Current. *Deep Sea Res.*, **23**, 1139–1152.

Cox, M. D., 1979: A numerical study of the Somali Current eddies. *J. Phys. Oceanogr.*, **9**, 311–326.

Cushman-Roisin, B. and J. J. O'Brien, 1983: The influence of bottom topography on baroclinic transports. *J. Phys. Oceanogr.*, **9**, 1600–1611.

Düing, W., R. L. Molinari and J. C. Swallow, 1980: Somali Current: Evolution of surface current. *Science*, **209**, 588–590.

Findlay, A. G., 1866: *A directory for the navigation of the Indian Ocean*. Richard Holmes Laurie, London, 1062 pp.

Gates, L. W., 1966: On the dynamical formulation of the large-scale momentum exchange between atmosphere and ocean. *J. Mar. Res.*, **24**, 105–112.

Gent, P. R., K. O'Neill and M. A. Cane, 1983: A model of the semiannual oscillation in the equatorial Indian Ocean. *J. Phys. Oceanogr.*, **13**, 2148–2160.

Gill, A. E., 1982: *Atmosphere-Ocean Dynamics*, Academic Press, 662 pp.

Gill, A. E., J. S. A. Green and A. J. Simmons, 1974: Energy partition in the large-scale ocean circulation and the production of mid-ocean eddies. *Deep-Sea Res.*, **21**, 497–528.

Hedley, M. and M. K. Yau, 1988: Radiation boundary conditions in numerical modeling. *Mon. Wea. Rev.*, **116**, 1721–1736.

Hellerman, S. and M. Rosenstein, 1983: Normal monthly wind stress over the world ocean with error estimates. *J. Phys. Oceanogr.*,**13**, 1093–1104.

Huang, R. X., 1987: A three-layer model for wind-driven circulation in a subtropical-subpolar basin. Part I: Model formulation and the subcritical state. *J. Phys. Oceanogr.*, **17**, 664–678.

Hurlburt, H. E., 1974: The influence of coastline geometry and bottom topography on the eastern ocean circulation. Ph.D. thesis, The Florida State University, 103 pp.

Hurlburt, H. E. and J. D. Thompson, 1976: A numerical model of the Somali Current. *J. Phys. Oceanogr.*, **6**, 646–664.

Hurlburt, H. E. and J. D. Thompson, 1980: A numerical study of the loop current intrusions and eddy shedding. *J. Phys. Oceanogr.*, **10**, 1611–1651.

Kindle, J. C. and J. D. Thompson, 1989: The 26- and 50-day oscillations in the Western Indian Ocean: Model Results. J. Geophys. Res., **94**, 4721–4736.

Knox, R. A., 1987: The Indian Ocean: Interaction with the Monsoon. In: *Monsoons*. Eds. J. S. Fein and P. L. Stephens. Wiley & Sons, 632 pp.

Knox, R. A. and D. L. T. Anderson, 1985: Recent advances in the study of the low-latitude ocean circulation. *Prog. Oceanogr.*, **14**, 259–317.

Kuo, H. L., 1949: Dynamic instability of two-dimensional nondivergent flow in a barotropic atmosphere. J. Meteor., **6**, 105–122.

Leetmaa, A., 1972: The response of the Somali Current to the southwest monsoon of 1970. *Deep-Sea Res.*, **19**, 319–325.

Leetmaa, A., 1973: The response of the Somali Current at 2°S to the southwest monsoon of 1971. *Deep-Sea Res.*, **20**, 397–400.

Leetmaa, A. H., D. R. Quadfasel and D. Wilson, 1982: Development of the flow field during the onset of the Somali Current. *J. Phys. Oceanogr.*, **12**, 1325–1342.

Leetmaa, A., H. T. Rossby, P. M. Saunders and P. Wilson, 1980: Subsurface circulation in the Somali Current. *Science*, **209**, 590–592.

Levitus, S., 1982: Climatological atlas of the world ocean. NOAA Prof. Paper, U.S. Dept. Commerce, 13, 173pp.

Lighthill, M. J., 1969: Dynamic response of the Indian Ocean to the onset of the Southwest Monsoon. *Phil. Trans. Roy. Soc.*, **A265**, 45–92.

Lilly, D. K., 1965: On the computational stability of numerical solutions of the time-dependent non-linear geophysical fluid dynamics problems. *Mon. Weather Rev.*,**93**, 11–26.

Lin, L. B. and H. E. Hurlburt, 1981: Maximum simplification of nonlinear Somali Current dynamics. In: *Monsoon Dynamics*. Eds. M. J. Lighthill and R. P. Pearce. Cambridge University Press.

Luther, M. E., 1987: Indian Ocean modelling. In: *Further progress in equatorial oceanography.* Eds. E.J. Katz and J. M. Witte. U.S. TOGA workshop rep., Nova University Press. 303–316.

Luther, M. E. and J. J. O'Brien, 1985: A model of the seasonal circulation in the Arabian Sea forced by observed winds. *Prog. Oceanogr.,*14, 353–385.

Luther, M. E. and J. J. O'Brien, 1989: Modelling the variability in the Somali Current. In: *Mesoscale/Synoptic Coherent Structures in Geophysical Turbulence.* Eds. J. C. J. Nihoul and B. M. Jamart, Elsivier Science Publ., Amsterdam, 373–386.

Luther, M. E., J. J. O'Brien and A. Meng, 1985: Morphology of the Somali Current system during the southwest monsoon. In: *Coupled Ocean-Atmosphere Models.* Ed. J. C. J. Nihoul, Elsevier, Amsterdam, 405–437.

Luyten, J. R. and D. H. Roemmich, 1982: Equatorial currents at semi-annual period in the Indian Ocean. *J. Phys. Oceanogr.,* **12**, 406–413.

Matsuura, T. and T. Yamagata, 1982: On the evolution of nonlinear planetary eddies larger than the radius of deformation. *J. Phys. Oceanogr.,* **12**, 440–456.

McCreary, J. P. and P. K. Kundu, 1985: Western boundary circulation driven by an alongshore wind: with application to the Somali Current system. *J. Mar. Res.,* **43**, 493–516.

McCreary, J. P. and P. K. Kundu, 1988: A numerical investigation of the Somali Current during the Southwest Monsoon. *J. Mar. Res.,* **46**, 25–58.

McNider, R. T. and J. J. O'Brien, 1973: A Multi-layer transient model of coastal upwelling. *J. Phys. Oceanogr.,* **3**, 258–273.

Mesinger, F. and A. Arakawa, 1976. Numerical methods used in atmospheric models. *GARP Publ. Ser. 17.* WMO, p. 45

Miller, M. J. and Thorpe, A. J., 1981: Radiation conditions for the lateral boundaries of limited area numerical models. *Quart. J. Roy. Soc. Meteor. Soc.*, **107**, 615–628.

Molinari, R. L., J. F. Festa and J. C. Swallow, 1986: Mixed layer and thermocline depth climatologies in the Western Indian Ocean. NOAA Tech. Memo. ERL AOML-64.

O'Brien, J. J., 1986: The diffusive problem. In: *Advanced Physical Oceanographic Numerical Modelling.* Ed. J. J. O'Brien. D. Reidel Publ., 127–144.

O'Brien, J. J. and H. E. Hurlburt, 1972: A numerical model of coastal upwelling. *J. Phys. Oceanogr.*, **2**, 14–26.

Orlanski, I., 1976: A simple boundary condition for unbounded hyperbolic flows. *J. Comput. Phys.*, **21**, 251–269.

Pedlosky, J., 1979: *Geophysical Fluid Dynamics*, Springer Verlag, 624 pp.

Perigaud, C. and P. Delecluse, 1988: Simulations of dynamic topography in the Northwestern Indian Ocean with input of Seasat altimeter and scatterometer data. *Ocean Air Interaction.* In press.

Philander, S. G. H. and R. C. Pacanowski, 1984: Simulations of the seasonal cycle in the tropical Atlantic Ocean. *Geophys. Res. Lett.*, **11**, 802–804.

Philander, S. G. H. and R. C. Pacanowski, 1986: A model of the seasonal cycle in the tropical atlantic ocean. *J. Geophys. Res.*, **91**, 14192–14206.

Quadfasel, D. R. and F. Schott, 1982: Water-mass distributions at intermediate layers off the Somali Coast during the onset of the southwest monsoon, 1979. *J. Phys. Oceanogr.*, **12**, 1358–1372.

Quadfasel, D. R. and F. Schott, 1983: Southward subsurface flow below the Somali Current. *J. Geophys. Res.*, **88**, 5973–5979.

Røed, L. P. and C. K. Cooper, 1986: Open boundary conditions in numerical ocean models. In: *Advanced Physical Oceanographic Numerical Modelling*. Ed. J. J. O'Brien. D. Reidel Publ. 411–436.

Røed, L. P. and C. K. Cooper, 1987: A study of various open boundary conditions for wind-forced barotropic numerical ocean models. In :*Three-Dimensional Models of Marine and Estuarine Dynamics*. Eds. J. C. J. Nihoul and B. M. Jamart. Elsevier. 305–335.

Røed, L. P. and O. M. Smedstad, 1984: Open boundary conditions for forced waves in a rotating fluid. *SIAM J. Sci. Stat. Comput.*, 5, 414–426.

Semtner, A. J., 1986: Finite-difference formulation of a world ocean model. In: *Advanced Physical Oceanographic Numerical Modelling*. Ed. J. J. O'Brien. D. Reidel Publ. 187–202.

Semtner, Jr., A. J. and R. M. Chervin, 1988: A simulation of the global ocean circulation with resolved eddies. *J. Geophys. Res.*, 93, 15502-15522.

Schopf, P. S. and M. Suarez, 1988: Vacillations in a coupled ocean-atmosphere model. *J. Atmos. Sci.*, 45, 549–566.

Schott, F., 1983: Monsoon response of the Somali Current and associated upwelling. *Prog. Oceanogr.*, 12, 357–381.

Schott, F., 1987: Recent studies of western Indian Ocean circulation. In: *Further progress in equatorial oceanography*. Eds. E.J. Katz and J. M. Witte. U.S. TOGA workshop rep., Nova University Press. 287–302.

Schott, F. and D. R. Quadfasel, 1980: Development of the subsurface currents of the Northern Somali Current Gyre from March to July 1979. *Science*, 209, 593–595.

Schott, F. and D. R. Quadfasel, 1982: Variability of the Somali Current system during the onset of the southwest monsoon. *J. Phys. Oceanogr.*, **12**, 1343–1357.

Simmons, R. C., M. E. Luther, J. J. O'Brien and D. M. Legler, 1988: Verification of a numerical ocean model of the Arabian Sea. *J. Geophys. Res.*, **93**, 15437–15461.

Swallow, J. C. and J. G. Bruce, 1966: Current measurements off the Somali coast during the southwest monsoon of 1964. *Deep-Sea Res.*, **13**, 861–888.

Swallow, J. C. and M. Fieux, 1982: Historical evidence for two gyres in the Somali Current. *J. Mar. Res.*, **40**, Suppl., 747–755.

Swallow, J. C., R. L. Molinari, J. G. Bruce, O. B. Brown and R. H. Evans, 1983: Development of near-surface flow pattern and water mass distribution in the Somali Basin in response to the southwest monsoon of 1979. *J. Phys. Oceanogr.*, **13**, 1398–1415.

Thompson, J. D. and W. J. Schmitz Jr., 1989: A limited-area model of the Gulf Stream: Design, initial experiments, and model-data intercomparison. *J. Phys. Oceanogr.*, **19**, 791–814.

Weisberg, R. H., 1987: Observations pertinent to instability waves in the equatorial oceans. In: *Further progress in Equatorial Oceanography*, Nova University Press, Fort Lauderdale, Fla., 335–350.

Woodberry, K., M. E. Luther and J. J. O'Brien, 1989: The wind driven seasonal circulation in the southern tropical Indian Ocean. To appear in *J. Geophys. Res.*, Dec. 1989.

Wyrtki, K., 1971: *Oceanographic Atlas of the International Indian Ocean Expedition*. National Science Foundation, Washington, DC, 531 pp.

Zalesak, S. T., 1979: Fully multidimensional flux-corrected transport algorithms for fluids. *J. Comput. Phys.*, **31**, 335–362.

Zebiak, S. E. and M. A. Cane, 1987: A model El Niño-Southern Oscillation. *Mon. Wea. Rev.*, **115**, 2262–2278.

Appendix A: Derivation of model equations

In this section the derivation of the transport equation will be presented in more detail. Assuming that the aspect ratio for the motion is small, *i.e.*, that the horizontal scale of motion is much larger than the vertical, we can neglect the vertical velocity everywhere, except in the continuity equation. The governing equations in spherical coordinates, which can be found in textbooks (for instance Pedlosky, 1979 or Gill, 1982) can in that case be written as follows. The velocity component in the east-west direction, positive towards east, must satisfy

$$\frac{Du}{Dt} - \left(2\Omega + \frac{u}{a\cos\phi}\right)v = -\frac{1}{\rho a\cos\theta}\frac{\partial p}{\partial\phi} + \frac{\partial}{\partial z}\left(A_V\frac{\partial u}{\partial z}\right) + \mathcal{G}^{\phi} \qquad (A-1)$$

where the total (or substantial) derivative is defined as

$$\frac{D}{Dt} \equiv \frac{\partial}{\partial t} + \vec{v}\cdot\nabla \qquad (A-2)$$

Here $\vec{v}$ is the horizontal velocity, Ω the rate of rotation of the Earth and A_V a vertical kinematic viscosity coefficient. Assuming a constant eddy viscosity A_H, the horizontal friction term for the u equation is given by

$$\mathcal{G}^{\phi} = A_H\left[\nabla^2 u - \frac{1}{a^2\cos^2\theta}\left[u(1 - 2\cos^2\theta) + 2\sin\theta\,\frac{\partial v}{\partial\phi}\right]\right] \qquad (A-3)$$

This form ensures that a fluid in solid-body rotation around an axis through a sphere does not experience any horizontal shear stress in spite of the fact that the velocity varies around the sphere. For instance a zonal flow with a velocity distribution with latitude given by $u = u_0\cos\theta$ should have no friction. The terms in addition to the Laplacian, which often is seen used alone in many models, are needed to satisfy this

condition. It is easily seen from a scale analysis, that these terms are very small except near the poles. However, for the sake of generality they are retained in this model.

For the velocity component in the north-south direction,v, we have

$$\frac{\partial v}{\partial t} + \left(2\Omega + \frac{u}{a\cos\phi}\right)u = -\frac{1}{\rho a}\frac{\partial p}{\partial \theta} + \frac{\partial}{\partial z}\left(A_V\frac{\partial u}{\partial z}\right) + \mathcal{G}^\theta \qquad (A-4)$$

with the horizontal friction term

$$\mathcal{G}^\theta = A_H\left[\nabla^2 v - \frac{1}{a^2\cos^2\theta}\left[v(1 - 2\cos^2\theta) + 2\sin\theta\,\frac{\partial}{\partial\phi}u\right]\right] \qquad (A-5)$$

In each layer, we will assume that the density is constant, i.e.,

$$\frac{D\rho}{Dt} = 0 \qquad (A-6)$$

This implies that the conservation of mass is governed by the continuity equation

$$\frac{1}{a\cos\theta}\frac{\partial u}{\partial\phi} + \frac{1}{a\cos\theta}\frac{\partial}{\partial\theta}(v\cos\theta) + \frac{\partial w}{\partial z} = 0 \qquad (A-7)$$

where w is the vertical velocity component.

To derive the transport equations we integrate across a layer of constant density and velocity. For instance we define the zonal volume transport

$$U = \int_{z_B}^{z_T} u\,dz \qquad (A-7)$$

over a layer of thickness

$$H = z_T - z_B \qquad (A-8)$$

The meridional transport component V is defined similarly.

Let us first consider the continuity equation. The first term becomes, using Leibnitz rule

$$\int_{z_B}^{z_T} \frac{1}{a\cos\theta}\frac{\partial u}{\partial\phi}dz = \frac{1}{a\cos\theta}\left[\frac{\partial U}{\partial\phi} - u\frac{\partial H}{\partial\phi}\right] \qquad (A-9)$$

The second term yields

$$\int\limits_{z_B}^{z_T} \frac{1}{a\cos\theta} \frac{\partial}{\partial\theta}(v\cos\theta)dz = \int\limits_{z_B}^{z_T} \left(-\frac{\tan\theta}{a}v + \frac{1}{a}\frac{\partial v}{\partial\theta}\right)dz$$

$$= -\frac{\tan\theta}{a}V + \frac{1}{a}\frac{\partial V}{\partial\theta} - \frac{v}{a}\frac{\partial H}{\partial\theta} \qquad (A-10)$$

Integrating the third term eliminates w from the system of equations:

$$\int\limits_{z_B}^{z_T} \frac{\partial w}{\partial z}dz = w(z_T) - w(z_B)$$

$$= \frac{Dz_T}{Dt} - \frac{Dz_B}{Dt} = \frac{DH}{Dt} \qquad (A-11)$$

where the last equality is possible due to the lack of vertical shear in the horizontal velocities. Adding the right hand sides of equations $(A-9)$ to $(A-11)$ gives the continuity equation $(2-7)$, viz.

$$\frac{\partial H_j}{\partial t} + \frac{1}{a\cos\theta}\left[\frac{\partial U_j}{\partial\phi} + \frac{\partial}{\partial\theta}(V_j\cos\theta)\right] = 0 \qquad (A-12)$$

The acceleration term in the u equation is

$$\frac{Du}{Dt} = \frac{\partial u}{\partial t} + \frac{u}{a\cos\theta}\frac{\partial u}{\partial\phi} + \frac{v}{a}\frac{\partial v}{\partial\theta} \qquad (A-13)$$

The first term becomes

$$\int\limits_{z_B}^{z_T} \frac{\partial u}{\partial t}dz = \frac{\partial U}{\partial t} - u\frac{\partial H}{\partial t} \qquad (A-14)$$

the third can be written, using v constant over the layer:

$$\frac{v}{a}\int\limits_{z_B}^{z_T} \frac{\partial u}{\partial\theta}dz = \frac{1}{a}\left[\frac{\partial vU}{\partial\theta} - U\frac{\partial v}{\partial\theta} - uv\frac{\partial H}{\partial\theta}\right]$$

$$= \frac{1}{a}\left[\frac{\partial}{\partial\theta}(\frac{UV}{H}) - u\frac{\partial V}{\partial\theta}\right] \qquad (A-15)$$

From this, it is easily seen that the second term becomes

$$\int_{z_B}^{z_T} \frac{u}{a\cos\theta}\frac{\partial u}{\partial\phi}dz = \frac{1}{a\cos\theta}\left[\frac{\partial}{\partial\phi}(\frac{U^2}{H}) - u\frac{\partial U}{\partial\phi}\right] \qquad (A-16)$$

Using the continuity equation $(A-12)$, we find

$$\int_{z_B}^{z_T} \frac{Du}{Dt}dz = \frac{\partial U}{\partial t} + \frac{1}{a\cos\theta}\frac{\partial}{\partial\phi}(\frac{U^2}{H}) + \frac{1}{a}\frac{\partial}{\partial\theta}(\frac{UV}{H}) - \frac{UV\tan\theta}{aH} \qquad (A-17)$$

Defining the Coriolis parameter

$$f \equiv 2\Omega\sin\theta \qquad (A-18)$$

we find that the total planetary acceleration is

$$\int_{z_B}^{z_T}\left(fv + \frac{uv\sin\theta}{a\cos\theta}\right)dz = fV + \frac{UV\tan\theta}{aH} \qquad (A-18)$$

which completes the left hand side of equation $(2-2)$.

The horizontal friction term $(2-3)$ is easily obtained from $(A-3)$ by using the definitions $u = U/H$ and $v = V/H$, and multiplying by H, again using the assumption that we do not have any vertical variation of the horizontal fields over a layer. The vertical friction is integrated as

$$\int_{z_B}^{z_T}\frac{\partial}{\partial z}A_z\frac{\partial u}{\partial z}dz = A_z\left(\frac{\partial u}{\partial z}\Big|_{z_T} - \frac{\partial u}{\partial z}\Big|_{z_B}\right) \equiv (\tau_T - \tau_B)/\rho \qquad (A-19)$$

The terms in the prediction equation $(2-4)$ for V are obtained in the same fashion.

We have not yet considered the pressure gradients. From figure 1, which represents the case of $N = 4$, we see that the hydrostatic pressure in the upper layer must be given by

$$p_1(z) = p_a - g\rho_1 z \qquad (A-20)$$

recalling that p_a is the atmospheric pressure and the z coordinate is negative in the ocean and zero at the sea surface $\eta(\phi, \theta)$. For deeper layers the top is at

$$z_{Tj} = -\sum_{i=1}^{j-1} H_i \qquad (A-21)$$

so we find

$$p_j(z) = p_{j-1}(z_{Tj}) - g\rho_j(z - z_{Tj}) \qquad (A-22)$$

where the pressure at the top of layer j equals the pressure at the bottom of layer $j-1$, e.g.,

$$p_{j-1}(z_{Tj}) = p_a + \sum_{i=1}^{j-1} g\rho_i H_i \qquad (A-23)$$

We need to find the horizontal pressure gradient, vertical integrated over each layer. It is straight forward, but requires a little algebra, to integrate first and then use Leibnitz formula to obtain this quantity. However, if we keep in mind that the vertical coordinate varies in the horizontal direction so that

$$\nabla z = -\nabla \eta = -\nabla \sum_{i=1}^{N} (D + H_i) \qquad (A-24)$$

we find, taking the gradient of $(A-22)$ and inserting the definitions $(A-21)$ and $(A-23)$:

$$\nabla p_j(z) = \nabla (p_a - \sum_{i=1}^{j-1} g(\rho_j - \rho_i) H_i) + \nabla \eta \qquad (A-25)$$

which integrates vertically by multiplication with H_j and gives the pressure terms as written in $(2-2)$ and $(2-4)$.

Appendix B: Open boundary conditions

Most oceanographic models cover a limited area of the world ocean. It is therefore nessessary to implement boundary conditions across parts of the ocean. Early models used walls with a free-slip condition along a latitude where the wind-stress curl is assumed to be zero. For linear steady models this is a natural boundary, since no meridional transport occurs. In time-dependent simulations a sponge layer where incoming waves are dispersed due to large amount of friction, has often been used. Here we adopt the definition of an open boundary by Røed and Cooper, (1986), to be a boundary where a wave can leave the computational domain, without reflection, and no information from the outside is prescribed. In that sense the boundary condition described below is not strictly open, since a small mount of diffusion and relaxation towards a far field has been added.

First the calculation of the vertical modes is considered. The approach is that of Lighthill (1969) except we are interested in the modes for the case where the N-th layer is at rest. For simplicity we use the linearized equations on an f-plane to derive the normal modes.

The inviscid equations are in transport form

$$\frac{\partial U_j}{\partial t} - fV_j = -\frac{1}{\rho_j}\frac{\partial P_j}{\partial x} + F_j \qquad (B-1)$$

$$\frac{\partial V_j}{\partial t} + fU_j = -\frac{1}{\rho_j}\frac{\partial P_j}{\partial y} + G_j \qquad (B-2)$$

where the vertical integrated pressure is given by

$$P_j = gH_{0j}\left(\rho_j \sum_{i=1}^{N-1}\frac{\rho_N - \rho_i}{\rho_N}H_i - \sum_{i=1}^{j-1}(\rho_j - \rho_i)H_i\right) \qquad (B-3)$$

110

and F_j and G_j is the external forcing on layer j. The continuity equation is

$$\frac{\partial H_j}{\partial t} = -\frac{\partial U_j}{\partial x} - \frac{\partial V_j}{\partial y} \qquad (B-4)$$

We proceed by inserting the expression for the pressure P, $(B-3)$ into $(B-1)$ and $(B-2)$ and take $\partial / \partial t$. Using continuity $(B-4)$ to eliminate $\partial H_i / \partial t$ from these equations we obtain

$$\frac{\partial^2 U_j}{\partial t^2} - f\frac{\partial V_j}{\partial t} = \frac{\partial F_j}{\partial t} - g\sum_{i=1}^{N-1} a_{ji}\left(\frac{\partial^2 U_j}{\partial x^2} + \frac{\partial^2 V_j}{\partial x \partial y}\right) \qquad (B-5)$$

and

$$\frac{\partial^2 V_j}{\partial t^2} + f\frac{\partial U_j}{\partial t} = \frac{\partial G_j}{\partial t} - g\sum_{i=1}^{N-1} a_{ji}\left(\frac{\partial^2 U_j}{\partial x \partial y} + \frac{\partial^2 V_j}{\partial y^2}\right) \qquad (B-6)$$

where the matrix a_{ji} is given by

$$a_{ji} = H_{0j}\left(1 - \frac{\rho_i}{\rho_N} - \frac{\rho_{\min(i,j)}}{\rho_j}\right) \qquad (B-7)$$

which is of the same form as the equations given by Lighthill, except for the coefficients in the matrix $(B-7)$.

The solution to $(B-5)$ and $(B-6)$ can be expressed as a sum of normal modes, i.e.,

$$U_j = \sum_{k=1}^{N-1} \alpha_j^k \tilde{U}_k \qquad (B-8)$$

where α_j^k is the j-th component of the k-th eigenvector of the matrix $(B-7)$, and $\tilde{U}_k$ the amplitude of the k-th mode given by

$$\tilde{U}_k = b_{kj} U_j \qquad (B-9)$$

is the product of the vertical transport in each layer with the k-th row of the matrix b_{kj}, which is the inverse of the matrix α_{kj}, which consists of the $N-1$ eigenvectors of a_{kj} as columns.

The $N-1$ eigenvalues h_k are the equivalent depths, which give the internal gravity phase speeds of the vertical modes as

$$c_k^2 = gh_k \qquad (B-10)$$

As a orthogonality condition we will require that

$$\sum_{j=1}^{N-1} \rho_j \alpha_j^m \alpha_j^n / H_j = \delta_{nm} \qquad (B-11)$$

where δ_{nm} is the Kronecker delta. The only external forcing considered in this study is the wind stress acting as a body force across the upper layer, i.e.,

$$(F_1, G_1) = (\tau^x, \tau^y)/\rho_1 \qquad (B-12)$$

which implies that the wind stress is projected onto the n-th vertical mode as

$$(F^n, G^n) = \frac{\alpha_1^n (\tau^x, \tau^y)/H_1}{\sum_{j=1}^{N-1} \rho_j (\alpha_j^n)^2 / H_j} \qquad (B-13)$$

However for the open boundary conditions as implemented in this study, the scaling is unimportant, as will be seen in what follows.

The finite-difference form of the equations $(2-2)$ and $(2-4)$ cannot be computed along open boundaries, since the values nessessary for such a computation are not available. To some extent one-sided difference schemes can be used, which was tried in some tests, but it is not possible for all terms in the equations. A popular method is to use an extrapolation of interior values towards the boundary. Here a Sommerfeld radiation condition is applied. This method assumes that disturbances travel as free waves towards the boundary, and separates the forcing and other physics. For a discussion of this see Røed and Smedstad (1984) and the review papers by Røed and Cooper (1986, 1987). We illustrate an open boundary to the east with waves propagating towards the boundary in the x- direction, e.g.,

$$\frac{\partial \Phi}{\partial t} + c_\Phi \frac{\partial \Phi}{\partial x} = 0 \qquad (B-14)$$

where Φ can be any of the dependent variables, and c_Φ is a phase speed.

The equation above can be solved locally for c_ϕ near the boundary by using finite differences. If we have the solution at time level n, we compute the phase speed

$$c_\Phi = -\frac{\Delta x}{\Delta t^*} \frac{\Phi_{B-1}^n - \Phi_{B-1}^m}{\Phi_{B-1}^{n-1} - \Phi_{B-2}^{n-1}} \qquad (B-15)$$

where $m = n-2$ and $\Delta t^* = 2\Delta t$ when the leap-frog scheme is used while $m = n-1$ and $\Delta t^* = \Delta t$ for the Euler forward scheme. Here the subscript $B-1$ denoted the variable one grid point from the boundary.

The new value at the boundary, Φ_B^{n+1} can the found, for instance using the modified Orlanski condition suggested by Miller and Thorpe, (1981):

$$\Phi_B^{n+1} = \begin{cases} \Phi_B^n & c_\Phi \leq 0 \\ (1 - c_\Phi')\Phi_B^n + c_\Phi'\Phi_{B-1}^n & c_\Phi > 0 \end{cases} \qquad (B-16)$$

where c_Φ' is the non-dimensionalized phase speed,

$$c_\Phi' = \min(c_\Phi \frac{\Delta t^*}{\Delta x}, 1) \qquad (B-17)$$

The Camerlengo and O'Brien,(1980) scheme corresponds to always using the maximal phase speed, i.e., $c_\Phi' = 1$, when the wave motion is towards the boundary. It should be noted , that the original schemes by Orlanski and by Camerlengo and O'Brien prescribed $\Phi_B^{n+1} = \Phi_B^{n-1}$ when $c_\Phi \leq 0$. The tests described below showed no dependence in the solutions on which time level was used.

Associated with the computation of the boundary value Φ_B^{n+1} it is common to apply a smoothing operation as done below. This will help absorb reflecting disturbances and reduce small scale noise.

The set of equations $(B-15)$ to $(B-17)$ can be applied to any of the variables U, V and H, or their normal mode amplitudes $\tilde{U}$, $\tilde{V}$ and $\tilde{H}$.

The following test case was considered to evaluate the boundary conditions with the least amount of reflection: A rectangular equatorial 2.5 layer ocean with

open southern and eastern boundaries was forced with a zonal wind stress in the western part of the basin to create an equatorial Kelvin wave. The densities of the three layers are 1025 kg/m^3, 1028.2 kg/m^3 and 1029 kg/m^3 while the initial layer thicknesses of the two active layers are 200 m and 300 m, respectively. The model equations and other parameters are the same as used in the model simulations of the main paper, except that the basin only was extended to 80° E.

Figure 51 shows the solution in the two layers after 10, 20 and 40 days. The first baroclinic Kelvin mode is passing through the eastern boundary from day 14 to day 30. Since the second vertical mode moves much slower we have a separation of the two Kelvin modes. At day 40 the second baroclinic mode is moving out of the domain. We see reflections into weak westward propagating Rossby waves, but no coastal Kelvin are propagating poleward along the western boundary.

Several possible combinations of the equations above were considered. One group of experiments applied (B − 15) to (B − 17) to the dependent variables layer by layer. At the eastern boundary, U was always calculated using an open boundary condition. Cases where H and V was calculated using the actual equations, with onenotrh-south-sided finite differences when nessessary, were considered in addition to cases where the open boundary condition were used for these variables. Both the modified Orlanski condition (B − 16) and the Camerlengo-O'Brien condition were tested. A second group of experiments were made where the variables considered were transformed into normal vertical modes prior to the application of the open boundary condition.

The condition which show the minimum reflection of the equatorial Kelvin wave into equatorial Rossby waves was the Camerlengo-O'Brien condition when it was applied to $\tilde{U}$ and $\tilde{V}$ and H was computed from the continuity equation. However, the differences found between the different cases were not very large, and
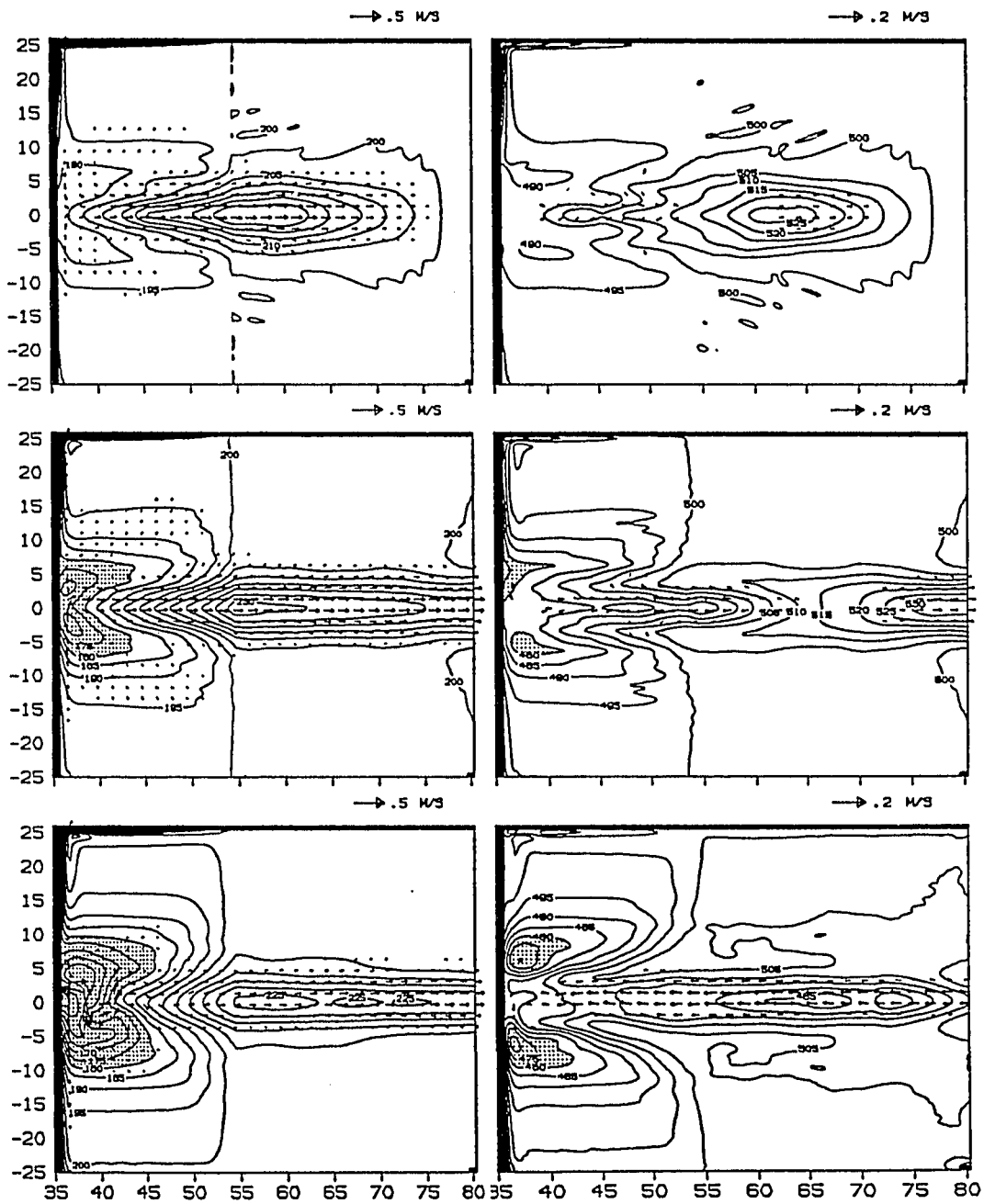
Figure 51. Equatorial Kelvin wave in 2.5 layer model. The initial depth to the bottom of layer 1 and 2 is 200 m and 500m. Top to bottom: Day 10, 20 and 40, in layer 1 (left) and layer 2 (right). Eastern and southern boundaries are open.

all cases produced reflections, which made it nessessary to apply some smoothing. A two-dimensional Hanning filter, *i.e.*,

$$\Phi'_{i,j} = \frac{1}{4}\Phi_{i,j} + \frac{1}{8}(\Phi_{i-1,j} + \Phi_{i+1,j} + \Phi_{i,j-1} + \Phi_{i,j+1})$$

$$+\frac{1}{16}(\Phi_{i-1,j-1} + \Phi_{i+1,j-1} + \Phi_{i-1,j+1} + \Phi_{i+1,j+1}) \qquad (B-18)$$

was applied to the two rows or columns nearest to the boundary for U, V and H. For the boundary points a one-sided smoothing was applied perpendicular to the boundary. If done every time step the absorbtion is very large, in fact the effective horizontal viscosity along the boundaries is two orders of magnitude higher that in the interior, and the choice of open boundary scheme is not important. With smoothing less frequent than every 10 time step reflections starts to become visible. As a compromise the Hanning filter was applied each 7th time step in this study.

In the Indian Ocean simulations it became clear that the open boundary conditions needed further modification where the future value of a variable depends on the conditions outside the domain. Along the east coast of Africa, coastal Kelvin waves travel towards the equator, and the same type of waves propagate counter clockwise around Madagascar. This implies that the layer thicknesses H_j is determined from the conditions outside the domain. With this modification the model failed to produce outflow along these coasts as seen in observations.

A relaxation towards observations was used by Cho and Clark (1981). When the flow was directed into the interior of their domain, they adjusted the solution obtained from the Orlanski scheme towards the far field conditions outside. For the two southermost H_j points along the coast of East Africa and Madagascar, we apply the relaxation, regardless of the direction of the flow,

$$H'_j = (1 - \varepsilon)H_j + \varepsilon H_{0j} \qquad (B-19)$$

where H'_j is the adjusted value and H_{0j} is the initial layer thickness. According to the atlas by Wyrtki (1971), H_{0j} is a reasonable choice for average thicknesses in the southern part of the Indian Ocean. It was attempted to adjust the layer thicknesses on the eastern side of Madagascar to those on the western side since pressure differences can propagate as coastal Kelvin waves. It worked well for the 1.5 layer model, but the 3.5 layer case developed a strong seasonal variation in the outflow along the east coast, and negatively correlated with that, in the flow north of Madagascar, which again influenced the conditions on the western side of the island. Since the amplitude of this seasonal variation in transport increased in time and may be due to some artificial resonance, this approach was not used.

The relaxation towards the far field, even if it is done in a few points as in this study does put restrictions on the flow condition. However some constraints may be nessessary. Hurlburt and Thompson (1980) found that recirculation through an open boundary, if unrestricted, can attain large unrealistic transports. To avoid this problem, Thompson and Schmitz (1989) who used a modified Orlanski open boundary condition, imposed a damping similar to (B − 19) at all inflow points, and scaled the total outflow uniformly to match the total inflow.

The formulation of the open boundaries does not constrain the inflow and outflow to conserve mass. The mass loss through the open boundaries correspond to a few meters of layer thickness per year of integration. While this is acceptable for shorter integrations, a compensation was needed in this study. In each time step the global average layer thickness anomaly is calculated for each layer, and subtracted from the thickness at each grid point, (Luther, personal communication). This can be thought of as a vertical diffussion of mass through the layers. Since the pressure gradients are unchanged by this adjustment, the geostrophic balance is not affected.

It should be clear from the discussion above, that the problem of implementing open boundary conditions for realistic ocean models has not been solved satisfactorily at this time, and there is a need for further work on this topic.